BAND STRUCTURE CALCULATION OF 3D ULTRAWIDE ELASTIC METAMATERIALS WITH EMBEDDED INERTIAL AMPLIFICATION MECHANISMS

by

Zafer Gökay Tetik

B.S., Mechanical Engineering, Yıldız Technical University, 2018

Submitted to the Institute for Graduate Studies in
Science and Engineering in partial fulfilment of
the requirements for the degree of
Master of Science

Graduate Program in Mechanical Engineering
Boğaziçi University

2022

ACKNOWLEDGEMENTS

This is the hardest part of the thesis. It is not easy to express my gratitude and sincere feelings to the people who helped me during this study. First of all, I would like to thank my supervisor Prof. Çetin Yılmaz for helping me not only technically but also emotionally and mentally. Thank you for believing in me, encouraging me whenever I fell into darkness and lost hope. Thank you for being a great guide and always available. Without his sacrifice, this thesis would not have been successfully completed. I would like to thank Prof. Serdar Soyöz and Assist. Prof. Polat Şendur for taking the time to read this thesis and providing insightful criticism about it.

Secondly, I would like to thank Berkay Acar and Sedef Nisan Otlu, with whom I worked on the same TUBITAK project, for their notable contributions and endless efforts. Working as a team was a lot of fun and it was one of the most important motivational sources of this work. I also owe a great thank to Ali Sarp Uyandıran for his encouragement and emotional support.

Last but not least, I would like to thank my family, especially my mother, for always believing in me. I would not be the person I am today without their great support.

This work was supported by TUBITAK Grant No. 218M475.

ABSTRACT

BAND STRUCTURE CALCULATION OF 3D ULTRAWIDE ELASTIC METAMATERIALS WITH EMBEDDED INERTIAL AMPLIFICATION MECHANISMS

In this study, phononic band structure of three dimensional (3D) ultrawide elastic metamaterials with embedded inertial amplification mechanisms are obtained. In order to achieve that, inertial amplification mechanisms with different sizes and geometries are considered by applying periodic boundary conditions, also known as Bloch's boundary conditions, to the unit cells. First, typical wave propagation problems in one dimensional, two dimensional, and three dimensional periodic structures studied in the literature are investigated and benchmark studies are performed by COMSOL Multiphysics and ABAQUS/MATLAB programs. In this way, these models are tested and verified so that the phonon band structure of the 3D elastic metamaterials with embedded inertial amplification mechanisms can be calculated accurately. Inertial amplification mechanisms have complex geometries and their computational costs can be very high. Thus, analyses are done by using both COMSOL Multiphysics and ABAQUS/MATLAB programs. Also, the comparison of the results obtained using these programs with the FRF results of the 3×2 octahedron array enables the determination of the most accurate model. It is very likely to encounter many problems when applying Bloch's theorem to a complex system such as a 3D elastic metamaterial with embedded inertial amplification mechanisms. Among many problems, four possible problems are explained and their solutions are presented. Thus, it is shown that the band structure of any geometry can be easily obtained, regardless of the complexity of the geometry. To sum up, in the literature, the widest band gap in 3D is achieved by this method, and the band gap is found to be in between 6.37 - 90.26 Hz, with a ratio of the upper limit to the lower limit of 14.17. Hence, it is demonstrated that the 3D elastic metamaterial with embedded inertial amplification mechanisms impedes waves coming from all directions in a very wide frequency range.

ÖZET

GÖMÜLÜ ATALET ARTIRIM MEKANİZMALARINA SAHİP ÜÇ BOYUTLU AŞIRI GENİŞ BANT ARALIKLI ELASTİK METAMALZEMELERİN BANT YAPISININ HESAPLANMASI

Bu çalışmada, gömülü atalet artırım mekanizmalarına sahip üç boyutlu ultra geniş bant aralıklı elastik metamalzemelerin fononik bant yapısı elde edilmiştir. Bunun için, Bloch sınır koşulları olarak da bilinen periyodik sınır koşulları birim hücrelere uygulanarak farklı boyut ve geometrilere sahip atalet artırım mekanizmaları ele alınmıştır. İlk olarak, literatürde incelenen bir boyutlu, iki boyutlu ve üç boyutlu periyodik yapılardaki tipik dalga yayılım problemleri incelenmiş ve COMSOL Multiphysics ve ABAQUS/MATLAB programları ile kıyaslama çalışmaları yapılmıştır. Bu sayede, gömülü atalet artırım mekanizmalarına sahip üç boyutlu elastik metamalzemelerin fonon bant yapısının doğru bir şekilde hesaplanabilmesi için bu modeller test edilmiş ve doğrulanmıştır. Atalet artırım mekanizmaları karmaşık geometrilere sahiptir ve hesaplama maliyetleri çok yüksek olabilir. Bu yüzden, hem COMSOL Multiphysics hem de ABAQUS/MATLAB programları kullanılarak analizler yapılmıştır. Ayrıca bu programlar kullanılarak elde edilen sonuçların, 3×2 sekizyüzlü dizisinin frekans tepki fonksiyon sonuçları ile karşılaştırılması en doğru modelin belirlenmesini sağlamıştır. Bloch teoremini, gömülü atalet artırım mekanizmalarına sahip üç boyutlu elastik metamalzeme gibi karmaşık bir sisteme uygularken birçok sorunla karşılaşma olasılığı çok yüksektir. Birçok problem arasından dört olası problem açıklanmış ve çözümleri sunulmuştur. Böylece, geometrinin karmaşıklığından bağımsız olarak herhangi bir geometrinin bant yapısının kolayca elde edilebileceği gösterilmiştir. Özetlemek gerekirse, literatürdeki üç boyutta en geniş bant aralığı bu yöntemle elde edilmiş ve bant aralığı, üst sınırın alt sınıra oranı 14.17 olup 6.37 - 90.26 Hz arasında bulunmuştur. Bu sayede, gömülü atalet artırım mekanizmalarına sahip üç boyutlu elastik metamalzemenin çok geniş bir frekans aralığında her yönden gelen dalgaları engellediği gösterilmiştir.

TABLE OF CONTENTS

ACKNOWLEDGEMENTS iii
ABSTRACT iv
ÖZET v
LIST OF FIGURES viii
LIST OF TABLES xv
LIST OF SYMBOLS xvi
LIST OF ACRONYMS /ABBREVIATIONS xviii
1. INTRODUCTION 1
1.1. Literature Review 2
2. BACKGROUND 5
2.1. Principle of Wave Propagation in Periodic Structures 5
2.1.1. Floquet-Bloch Theory 5
2.1.2. Lattice Symmetry, Reciprocal Lattice and Brillouin Zones 6
2.1.3. 1D Uniform Periodic Structure 10
2.2. Band Gap Generation Methods 11
2.2.1. Bragg Scattering Method 12
2.2.2. Local Resonance Method 13
2.2.3. Inertial Amplification Mechanism 15
2.2.4. Comparison of Band Gap Generation Methods 18
2.3. Bloch Boundary Condition in the Finite Element Method 19
2.3.1. Implementation of Bloch Boundary Condition in the FEM 25
2.4. Benchmark Solutions of the Wave Problems in Periodic Structures 28
2.4.1. Benchmark Solution of the Wave Problem in 1D Periodic Structure 28
2.4.2. Benchmark Solution of the Wave Problem in 2D Periodic Structure 30
2.4.3. Benchmark Solution of the Wave Problem in 3D Periodic Structure 34
3. ANALYSIS OF THE 3D INERTIAL AMPLIFICATION MECHANISMS 38
3.1. FEM Model of the 3D Inertial Amplification Mechanism 38
3.2. FEM Model of the First Optimized 3D Inertial Amplification Mechanism 50
3.3. FEM Model of the Second Optimized 3D Inertial Amplification Mechanism 53

3.4. FEM Model of the Optimized Large Scale 3D Inertial Amplification Mechanism……...58
4. CONCLUSION 63
REFERENCES 65
APPENDIX A: PSEUDO CODE THAT COMPUTES THE BAND STRUCTURE OF THE 2D STRUCTURES……76
APPENDIX B: ELSEVIER LICENSE NUMBER 5458851205096……77
APPENDIX C: JOHN WILEY AND SONS LICENSE NUMBER 5458850506031……78
APPENDIX D: ELSEVIER LICENSE NUMBER 5458850899369……79

LIST OF FIGURES

Figure 2.1.	Schematic representations of (a) 1D, (b) 2D, and (c) 3D periodic structures, respectively.....	5
Figure 2.2.	An infinite periodic series of masses m in 1D……..	6
Figure 2.3.	Five possible 2D Bravais lattices (a) oblique, (b) square, (c) rectangular, (d) centered rectangular, (e) hexagonal. The only non-primitive (conventional) structure is the centered rectangular lattice structure and the rest are primitive lattices……	7
Figure 2.4.	14 possible 3D Bravais lattices a) simple (primitive) cubic, b) body centered cubic, c) face centered cubic, d) simple tetragonal, e) body centered tetragonal, f) simple orthorhombic, g) base centered orthorhombic, h) body centered orthorhombic, i) face centered orthorhombic, j) trigonal, k) hexagonal, l) simple monoclinic, m) base centered monoclinic, n) triclinic…….	7
Figure 2.5.	The first six BZs of a 2D square lattice. The green color denotes the first BZ, and each color indicates the next BZ……	9
Figure 2.6.	(a) A square unit cell with a circular inclusion, (b) the corresponding BZ and IBZ of the unit cell, and (c) the phonon band structure of the unit cell calculated by following a route around the edge of the IBZ……..	10
Figure 2.7.	1D uniform periodic structure…….	10
Figure 2.8.	Phonon band structure of a 1D uniform periodic mass spring system for the parameters $m = 1, k = 2, a = 1$……..…	11

Figure 2.9. 1D periodic structure with two different masses and uniform springs……. 12

Figure 2.10. Phonon band structure of a 1D periodic structure with different masses and uniform springs system for the parameters $m_1 = 1, m_2 = 2, k = 2,\ a = 1$……..…… 13

Figure 2.11. 1D periodic structure of the local resonance model……..... 14

Figure 2.12. Band structure of the 1D periodic structure of the local resonance model for the parameters $m_m = 1,\ m_a = 2,\ k_m = 2,\ k_a = 3,$ $a = 1$……..... 15

Figure 2.13. Lumped parameter of the inertial amplification mechanism…..... 15

Figure 2.14. 1D periodic structure of the lumped parameter inertial amplification mechanism……...…… 17

Figure 2.15. Band structure of the 1D periodic structure of the lumped parameter inertial amplification mechanisms for $m_x/m_t = 1/3,$ $\theta = \pi/12,\ \ m_x/m_t = 2/3,\ \ \theta = \pi/12,$ and $m_x/m_t = 1/3,$ $\theta = \pi/18$. For all cases, $k = 2, a = 1$…..……...…… 18

Figure 2.16. Comparison of the band structures of the inertial amplification, Bragg scattering and local resonance methods for $m_x = m_1 =$ $m_m = 1, m_2 = m_a = 2, \theta = \pi/12, k = 2, k_a = 3, a = 1$…… 19

Figure 2.17. A 2D unit cell FE mesh showing the DOFs of the nodes required to apply the 1D Bloch BC. In the unit cell, the subscript L denotes left, I=internal, R= right. All nodes that are not on the left and right boundaries are considered internal nodes…… 20

Figure 2.18. A 2D unit cell FE mesh showing the DOFs of the nodes required to apply the 2D Bloch BC. In the unit cell, the subscript L denotes left, I=internal, R= right, T=top, B=bottom. All nodes that are not in the perimeter are considered internal nodes…..……... 21

Figure 2.19. A 3D unit cell FE mesh showing the DOFs of the nodes required to apply the 3D Bloch BC. The subscript l represents left, R=right, f=front, r=rear, b=bottom, t=top, I=internal. All nodes not explicitly specified are considered internal nodes……... 22

Figure 2.20. (a) Periodic structure, and (b) unit cell model of the sample model investigated in Ref. [31]……..... 28

Figure 2.21. Phonon band structure showing 1D wave propagation of the model investigated in Ref. [31]……..... 29

Figure 2.22. The corresponding faces in the *x* direction of the sample model created in COMSOL Multiphysics…….. 29

Figure 2.23. Phonon band structure showing the 1D wave propagation of the sample model investigated in Ref [31], obtained by using COMSOL Multiphysics……. 30

Figure 2.24. (a) Periodic structure, (b) and (c) unit cell of the sample model investigated in Ref. [7]……..... 31

Figure 2.25. Phonon band structure showing the 2D wave propagation of the model investigated in Ref. [7]……..... 31

Figure 2.26. (a) The corresponding nodes in the *x* direction, (b) *y* direction of the sample model created in ABAQUS. (c) IBZ of the unit cell investigated in Ref. [7]……..... 32

Figure 2.27. Phonon band structure showing the 2D wave propagation of the sample model investigated in Ref. [7], obtained by using ABAQUS/MATLAB…..……..... 33

Figure 2.28. Phonon band structure showing the 2D wave propagation of the sample model investigated in Ref. [7], obtained by using COMSOL Multiphysics……. 33

Figure 2.29. (a) Periodic structure, and (b) unit cell of the sample model in Ref. [13]…….. 34

Figure 2.30. IBZ of the unit cell studied in Ref. [13]…… 34

Figure 2.31. Phonon band structure showing the 3D wave propagation of the model studied in Ref. [13]……... 35

Figure 2.32. Phonon band structure showing the 3D wave propagation of the sample model investigated in Ref. [13], obtained by using ABAQUS/MATLAB…..……..... 36

Figure 2.33. Phonon band structure showing the 3D wave propagation of the sample model investigated in Ref. [13], obtained by using COMSOL Multiphysics……. 37

Figure 3.1. (a) Front view and (b) top view of the designed inertial amplification mechanism unit cell model……..…… 38

Figure 3.2. Seven thin flexures of the inertial amplification mechanisms. (a) First (x_1) and second (x_2) remote center flexures, horizontal flexure (x_3), and cross flexures (x_4, x_5). (b) Middle long (x_6) and short flexures (x_7) of the mechanism……... 39

Figure 3.3. (a) Front view and (b) top view of the periodic structure of the designed inertial amplification mechanism……. 40

Figure 3.4. High symmetry points of the triclinic crystal structure and the IBZ of the inertial amplification mechanism…….. 41

Figure 3.5. The mesh structure of the inertial amplification mechanism……... 42

Figure 3.6. Detailed view of the surface marked with yellow circle in Figure 3.5. (a) Unsymmetrical matching surfaces of the 3D inertial amplification mechanism obtained using the structured mesh technique, and (b) symmetrical matching surfaces obtained using the sweep mesh technique……... 43

Figure 3.7. (a) Detailed view of the surface shown in Figure 3.6. (a) Red circles show hexahedral mesh structures obtained using the structured mesh technique, and (b) yellow circles show distorted mesh structures obtained using the sweep mesh technique…….. 43

Figure 3.8. Phonon band structure showing the 3D wave propagation of the inertial amplification mechanism obtained using ABAQUS/MAT-LAB……. 46

Figure 3.9. Phonon band structure showing the 3D wave propagation of the inertial amplification mechanism obtained using COMSOL Multiphysics……..... 48

Figure 3.10. 3×2 octahedron array model of the inertial amplification mechanism [87]....…….……. 49

Figure 3.11. Frequency responses of the 3×2 octahedron array model of the inertial amplification mechanism [87]……. 49

Figure 3.12. (a) Front view and (b) top view of the first optimized unit cell model……... 51

Figure 3.13. (a) First (x_1) and second (x_2) remote center flexures, horizontal (x_3), and cross flexures (x_4, x_5). (b) Middle long (x_6) and short flexures (x_7), and three truss elements (x_8, x_9, x_{10}) of the first optimized mechanism……..…… 51

Figure 3.14. (a) The geometry of the top matching surfaces of the first optimized inertial amplification mechanism, and (b) its mesh structure obtained using the C3D4 tetrahedral element type…… 52

Figure 3.15. Phonon band structure showing the 3D wave propagation of the first optimized inertial amplification mechanism obtained using ABAQUS/MATLAB……... 53

Figure 3.16. (a) Front view and (b) top view of the second optimized inertial amplification mechanism unit cell model…… 54

Figure 3.17. Node numbering of 2D and 3D elements in FEM…… 55

Figure 3.18. Phonon band structure showing the 3D wave propagation of the second optimized inertial amplification mechanism obtained using ABAQUS/MATLAB……. 57

Figure 3.19. Frequency responses of the 3×2 octahedron array model of the second optimized inertial amplification mechanism……... 58

Figure 3.20. (a) Front view and (b) top view of the optimized large scale inertial amplification mechanism unit cell model…… 59

Figure 3.21. (a) First (x_1) and second (x_2) remote center flexures, horizontal flexure (x_3), and cross flexures (x_4, x_5). (b) Middle long (x_6) and short flexures (x_7), and three truss elements (x_8, x_9, x_{10}) of the large scale mechanism……. 60

Figure 3.22. (a) Left corner geometry of the newly designed optimized large scale model, and (b) left corner geometry of the previously designed (see Figure 3.12) model of the inertial amplification mechanism……... 61

Figure B.1. Elsevier license of [31] for Figures 2.20 and 2.21……..….. 77

Figure C.1. John Wiley and Sons license of [7] for Figures 2.24, 2.25 and 2.26..... 78

Figure D.1. Elsevier license of [13] for Figures 2.29, 2.30 and 2.31……... 79

LIST OF TABLES

Table 1.1. Bandwidth comparison of 3D phononic crystals and elastic metamaterials with a ratio of upper limit to lower limit greater than three in the literature…… 3

Table 3.1. Natural frequencies of the model with the reduced number of nodes and the percentage deviations from the original model…….. 45

Table 3.2. Natural frequencies of the models created using ABAQUS and COMSOL Multiphysics, and the percentage deviations from the ABAQUS (original) model…..……. 47

LIST OF SYMBOLS

a	Distance between two adjacent particles or nodes
$\mathbf{a_1}, \mathbf{a_2}, \mathbf{a_3}$	Real lattice primitive vectors
$\mathbf{b_1}, \mathbf{b_2}, \mathbf{b_3}$	Reciprocal lattice primitive vectors
BW_a	Arithmetic mean normalized bandwidth
BW_g	Geometric mean normalized bandwidth
E	Young modulus
e	Euler's number
$\mathbf{G}$	Reciprocal lattice vector
$\mathbf{I}$	Identity matrix
i	Imaginary unit
k	Stiffness
k_a, k_m	Stiffness coefficients in local resonance example
$\mathbf{K}$	Stiffness matrix
$\mathbf{K_R}$	Reduced stiffness matrix
l	Length of the ring
m	Mass
m_1, m_2	Masses in Bragg scattering example
m_a, m_m	Masses in local resonance example
m_t	Total mass
m_x	Mass in the inertial amplification mechanism
$\mathbf{M}$	Mass matrix
$\mathbf{M_R}$	Reduced mass matrix
$\mathbf{P}$	Bloch periodicity matrix
$\mathbf{P^T}$	Hermitian transpose of Bloch periodicity matrix
$\mathbf{q}$	Free DOF vector
$\mathbf{q_R}$	DOFs of the nodes
$\breve{\mathbf{q}}$	Reduced DOF vector
$\mathbf{R}$	Real space lattice vector
r	Radius of the ring

$T(\omega)$	Displacement transmissibility of the mechanism
$u^{(n)}, u^{(n+j)}$	Displacements of the n^{th} and $(n+j)^{th}$ masses
x_1	First remote center flexures of the inertial amplification mechanism
x_2	Second remote center flexures of the inertial amplification mechanism
x_3	Horizontal flexure of the inertial amplification mechanism
x_4, x_5	Cross flexures of the inertial amplification mechanism
x_6	Middle long flexures of the inertial amplification mechanism
x_7	Short flexures of the inertial amplification mechanism
x_8, x_9, x_{10}	Truss elements of the inertial amplification mechanism
x_a	Horizontal displacement of the small mass in the inertial amplification mechanism
y_a	Vertical displacement of the small mass in the inertial amplification mechanism
γ	Wave vector
δ_{ij}	Kronecker delta
θ	Angle between the spring and the stiff links in the inertial amplification mechanism
λ	Lame constant
μ	Lame constant
υ	Poisson's ratio
ρ	Mass density
ω	Excitation frequency
ω_l	Lower limit of the band gap
ω_p	Resonance frequency
ω_{p1}, ω_{p2}	First two resonance frequencies of the mechanism
ω_u	Upper limit of the band gap
ω_z	Antiresonance frequency

LIST OF ACRONYMS /ABBREVIATIONS

1D	One Dimensional
2D	Two Dimensional
3D	Three Dimensional
C3D4	Four Node Tetrahedral Element
C3D8R	Eight Node Hexahedral Element with Reduced Integration
BC	Boundary Condition
BZ	Brillouin Zone
CPU	Central Process Unit
DOF	Degree of Freedom
FD	Finite Difference
FE	Finite Element
FE-LSPI	Finite Element Least Square Point Interpolation
FEM	Finite Element Method
FDTD	Finite Difference Time Domain
FRF	Frequency Response Function
GB	Gigabyte
GHz	Gigahertz
Hz	Hertz
IBZ	Irreducible Brillouin Zone
LM	Lumped Mass
MST	Multiple Scattering Theory
MPC	Multipoint Constraints
PBC	Periodic Boundary Condition
PWE	Plane Wave Expansion
RAM	Random Access Memory
TM	Transfer Matrix
TUBITAK	The Scientific and Technological Research Council of Turkey
TWA	Traveling Wave Analysis

1. INTRODUCTION

Periodic structures are described as the infinite repetition of a particular part, known as unit cell, in one (1D), two (2D), or three dimensions (3D). There are, naturally, no infinite structures in the real world; yet, taking into consideration their infinite counterparts can provide valuable information regarding the behavior of the finite systems. There are some periodic structures called phononic crystals that impede wave transmission in specific frequency ranges known as phononic band gaps or stop bands. Band gaps can be obtained in both infinite and finite periodic systems. The number of unit cells in a periodic structure affects the amount of vibration attenuation in the band gap. That is, higher the number of unit cells, the greater the attenuation. Thus, there is no vibration transmission for the infinite periodic case [1,2]. In contrast to the infinite case, there is some vibration transmission in the finite periodic case. The level of vibration isolation provided by the system is determined by the depth of the gap (stop band) in a frequency response function plot of the finite periodic case [3-5]. Thanks to Bloch's theorem, infinite periodic structures can be analyzed by taking into consideration only a single unit cell. Phonon band structure, also called dispersion diagram, explains the behavior of infinite periodic structures by describing the relationship between wave vector and frequency [6].

There are various methods to calculate the phonon band structure of a periodic media, including the finite element (FE) method [7-12], finite element least square point interpolation (FE-LSPI) method [13], finite difference (FD) method [14,15], plane wave expansion (PWE) method [1,16-18], multiple scattering theory (MST) [19-21], finite-difference time domain (FDTD) method [22-27], transfer matrix (TM) method [28-31], lumped mass (LM) method [32,33], and traveling wave analysis (TWA) method [34]. Each approach has its own drawbacks such as convergence, stability, computational complexity and so on. Therefore, when calculating the band structures of periodic systems, the geometry, complexity and dimensions of the structures should be considered.

All in all, finite element method (FEM) is used to generate models in this thesis. In these models, by applying Bloch's theorem, the wave propagation analysis turns into a generalized eigenvalue problem in which the natural frequencies are square roots of the

eigenvalues and the mode shapes are the eigenvectors. Thus, the phonon band structures are obtained by solving the eigenvalue problems.

1.1. Literature Review

In the literature, band gaps in periodic structures are often created by Bragg scattering, level repulsion, local resonance, and inertial amplification methods [35]. Band gaps can occur due to material, geometric, boundary or a combination of these periodicities [36]. Band gaps are formed by periodically changing mass and stiffness values in Bragg scattering method. The lowest band gap frequency obtained by this method is found by the ratio of the wave speed to the lattice constant [37,38]. Hence, high density/low elastic modulus materials or large scale structures are required to form band gaps at low frequencies. Periodic structures employing the Bragg scattering technique are frequently referred to as phononic crystals. In local resonance method, band gaps are generated by adding local resonators to a main structure and band gaps can be obtained below the Bragg limit [39,40]. Yet, this method cannot create band gaps at low frequencies without using heavy resonators [37,38]. Periodic structures that employ the local resonance technique are typically referred to as elastic metamaterials since band gaps can be obtained below the Bragg limit. In level repulsion method, band gaps are created by the coupling of various polarization modes. However, this method usually does not generate wide band gaps [41].

In inertial amplification method, band gaps are obtained by utilizing embedded amplification mechanisms to increase the effective inertia [42,43]. Thanks to the amplified inertia, the wave propagation in the structure becomes difficult and thus, wide band gaps at low frequencies are produced without changing the mechanism's overall mass or stiffness. Periodic structures that contain inertial amplification mechanisms are also regarded as elastic metamaterials because this method enables to create band gaps below the Bragg limit. These characteristics have led to an increase in interest in creating band gaps by using inertial amplification method [44-67]. In the literature, the widest band gaps in 1D [51] and 2D [54] have been generated by this method. In this thesis, the aim is to obtain the widest band gap in 3D. The comparison of 3D phononic crystals and elastic metamaterials with a ratio of upper limit to lower limit (ω_u/ω_l) greater than three in the literature is given in Table 1.1. As shown in Table 1.1, $BW_a = 2(\omega_u - \omega_l)/(\omega_u + \omega_l)$ and $BW_g = (\omega_u - \omega_l)/(\sqrt{\omega_u \omega_l})$

are arithmetic and geometric mean normalized bandwidths, respectively and the widest bandwidth ever generated is between 1292.5 Hz and 16875 Hz, with an upper and lower limit ratio of 13.06 [68]. The main purpose of this study is to analyze 3D ultrawide elastic metamaterials with embedded inertial amplification mechanisms by applying Bloch's theorem and to obtain their phonon band structures of the infinitely periodic case.

Table 1.1. Bandwidth comparison of 3D phononic crystals and elastic metamaterials with a ratio of upper limit to lower limit greater than three in the literature.

References	ω_u (Hz)	ω_l (Hz)	ω_u/ω_l	BW_a	BW_g
Current Study 1	90.26	6.37	14.17	173.6%	349.9%
Current Study 2	457.5	33.7	13.58	172.6%	341.3%
Muhammed and Lim (2021) [68]	16875	1292.5	13.06	171.5%	333.7%
Martinez et al. (2021) [69]	7500000	600000	12.50	170.4%	325.3%
Muhammad and Lim (2021) [70]	11319	1247.2	9.08	160.3%	268.1%
Muhammad (2021) [71]	17890	2207.7	8.10	156.1%	249.5%
D'Alessandro et al. (2019) [72]	2337	455	5.14	134.8%	182.5%
D'Alessandro et al. (2016) [73]	18870	3850	4.90	132.2%	176.2%
Taniker and Yilmaz (2015) [47]	242	50	4.84	131.5%	174.5%
Lu et al. (2017) [74]	230000	75000	3.07	101.6%	118%

Last but not least, the original contributions made by this study to the literature can be summed up as follows

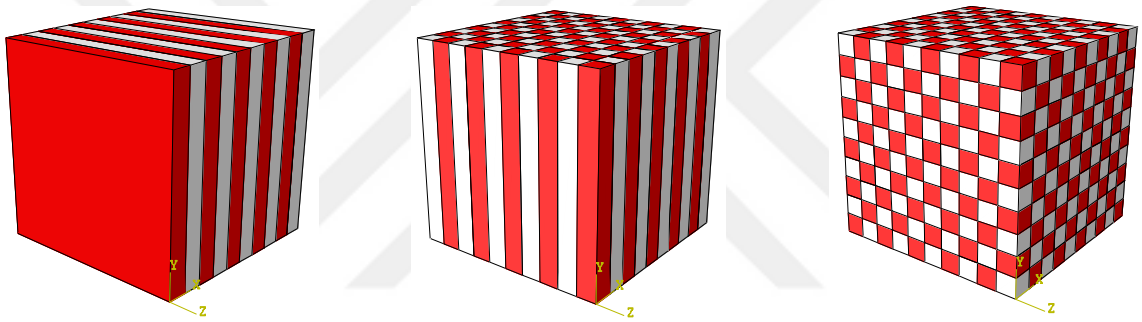
- The unit cell model of the 3D elastic metamaterial with embedded inertial amplification mechanism is obtained by combining six identical 1D inertial amplification mechanisms.
- Triclinic Irreducible Brillouin Zone (IBZ) is used for the first time for the 3D elastic metamaterial with embedded inertial amplification mechanisms.

- Phononic band structures of 3D elastic metamaterials with embedded inertial amplification mechanisms are obtained for the first time.
- When compared to 3D phononic crystals and elastic metamaterials, the widest band gap is obtained.

2. BACKGROUND

2.1. Principle of Wave Propagation in Periodic Structures

Unit cells are described as the smallest repeated unit in a periodic structure which can repeat itself in 1D, 2D or 3D. As seen in Figure 2.1, each material is indicated with different colors and the red-white marked cell is called unit cell or primitive cell. The periodic structures of the unit cell generated by expanding the unit cell in 1D, 2D and 3D are shown in Figure 2.1a, b and c, respectively.



(a) (b) (c)

Figure 2.1**.** Schematic representations of (a) 1D, (b) 2D, and (c) 3D periodic structures, respectively.

The behavior of the infinite periodic structure can be predicted by applying Floquet Bloch Theory to a single unit cell. In this way, phonon band structure that explains the relationship between the wave vector and its frequency can be found. This diagram gives information about transmission of waves such as pass bands and band gaps. In the former case waves propagate, whereas in the latter case waves do not propagate [6].

2.1.1. Floquet-Bloch Theory

Bloch’s theorem describes waves in periodic materials [75]. Bloch's theorem, which states the wave function of a periodically repeating particle, can be expressed in terms of displacements of neighboring unit cells as follows

$$u^{(n+j)} = e^{i\gamma a j} u^{(n)} \tag{2.1}$$

where $u^{(n)}$ and $u^{(n+j)}$ are the displacements of the n^{th} and $(n+j)^{th}$ masses, respectively, a is the distance between two adjacent particles, $i = \sqrt{-1}$ and γ is the wave number. An infinite periodic series of masses m with distance a is shown in Figure 2.2.

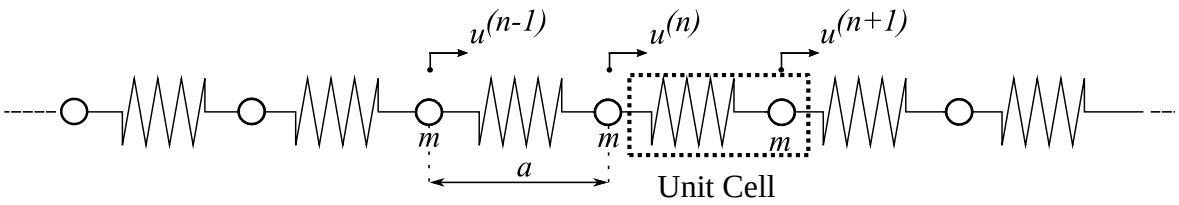


Figure 2.2. An infinite periodic series of masses m in 1D.

The displacement of the particle $(n+1)$ can be written in terms of $u^{(n)}$ by applying Bloch's theorem as

$$u^{(n+1)} = e^{i\gamma a} u^{(n)}. \tag{2.2}$$

2.1.2. Lattice Symmetry, Reciprocal Lattice and Brillouin Zones

A lattice can be described as an infinite set of mathematical points that are arranged in periodic order in space. Naturally, there are an infinite number of lattices that can exist depending on various periodicities. Point group symmetry and space group symmetry are the two types of lattice symmetry that are used to categorize these lattices. In point group symmetry, at least one point needs to be fixed. In other words, this group has all the symmetry operations except translations, since there is no fixed point in translation operations. Space group symmetry, on the other hand, has all symmetry operations, including translations. If lattices are grouped depending on point group symmetry, there are four types of lattice systems in 2D, and seven types in 3D, also called primitive unit cells. Primitive and conventional unit cells are subgroups of unit cells. Primitive unit cells have exactly one lattice point, composed of the lattice points at each corner. Conventional unit cells, however, may include more than one lattice point, either on a surface or within the unit cell.

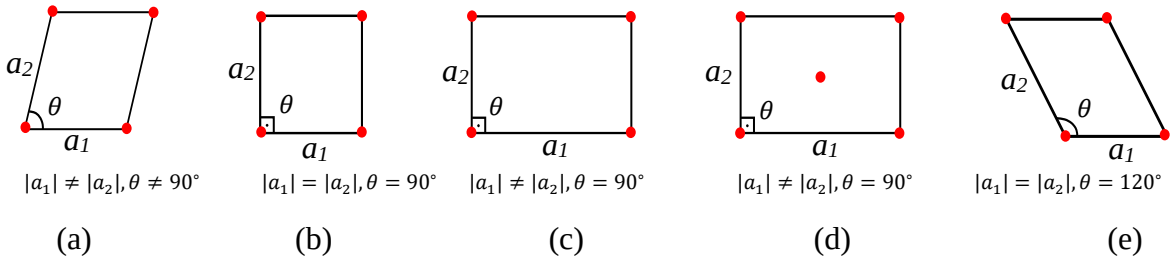


Figure 2.3. Five possible 2D Bravais lattices (a) oblique, (b) square, (c) rectangular, (d) centered rectangular, (e) hexagonal. The only non-primitive (conventional) structure is the centered rectangular lattice structure and the rest are primitive lattices.

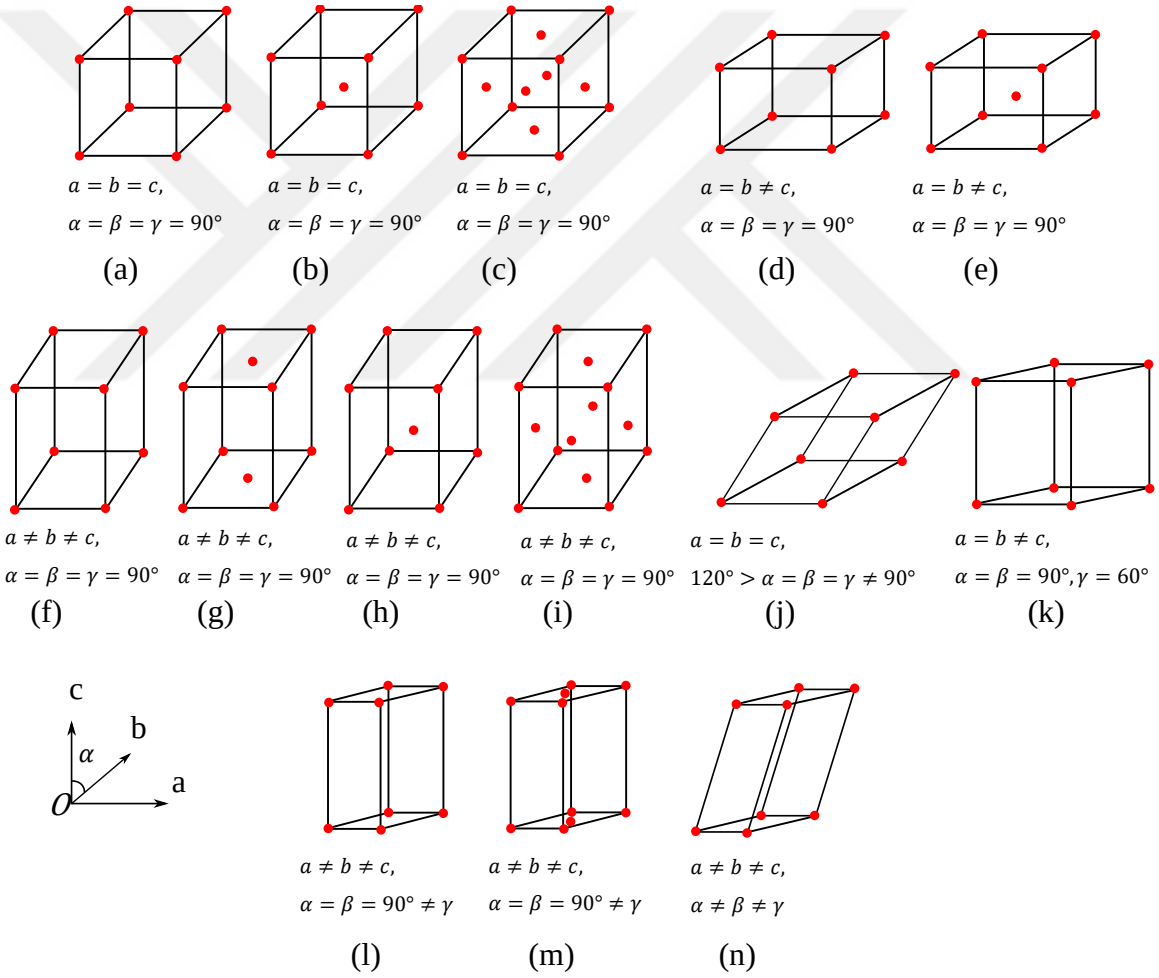


Figure 2.4. 14 possible 3D Bravais lattices a) simple (primitive) cubic, b) body centered cubic, c) face centered cubic, d) simple tetragonal, e) body centered tetragonal, f) simple orthorhombic, g) base centered orthorhombic, h) body centered orthorhombic, i) face centered orthorhombic, j) trigonal, k) hexagonal, l) simple monoclinic, m) base centered monoclinic, n) triclinic.

If lattices are categorized according to space group symmetry, there are five types of Bravais lattices in 2D, and 14 types in 3D [6]. The term Bravais lattice means that all lattice points are equal and seem the same regardless of the lattice from which they are viewed. The Bravais lattices in 2D are shown in Figure 2.3. As it can be seen in Figure 2.3, there are five Bravais lattices in 2D, four of which are primitive unit cells and one of which is conventional unit cell. The 14 possible 3D Bravais lattices, seven of which are primitive lattices, are shown in Figure 2.4. The angles α, β, γ are described based on usual geometrical convention and α is the angle between b and c. The periodic structure of the inertial amplification mechanism in 3D will be a Triclinic lattice. All analyses in this thesis are performed in the light of this information. Details will be given in the next chapter.

The real space lattice and the reciprocal lattice are two types of lattices that exist in every periodic structure. The former defines the periodic structure, while the latter describes the relationship between periodic structures and waves. Reciprocal space, also known as k space or momentum space, is the Fourier transform of real space [76]. Any real lattice can be defined by three primitive translational vectors $\mathbf{a_1}, \mathbf{a_2}, \mathbf{a_3}$. The real space lattice vector can be written as

$$\mathbf{R} = n_1\mathbf{a_1} + n_2\mathbf{a_2} + n_3\mathbf{a_3}. \tag{2.3}$$

where n_i are any integers. By using primitive vectors of the material lattice in real space, primitive vectors of the reciprocal lattice in reciprocal space can be found as

$$\mathbf{b_1} = 2\pi\frac{\mathbf{a_2}\ x\ \mathbf{a_3}}{\mathbf{a_1}.\ \mathbf{a_2}\ x\ \mathbf{a_3}}\ ,\ \mathbf{b_2} = 2\pi\frac{\mathbf{a_3}\ x\ \mathbf{a_1}}{\mathbf{a_1}.\ \mathbf{a_2}\ x\ \mathbf{a_3}}\ ,\mathbf{b_3} = 2\pi\frac{\mathbf{a_1}\ x\ \mathbf{a_2}}{\mathbf{a_1}.\ \mathbf{a_2}\ x\ \mathbf{a_3}}. \tag{2.4}$$

The real lattice primitive vectors and the reciprocal lattice primitive vectors have the following relationship

$$\mathbf{b_i}.\mathbf{a_j} = 2\pi\delta_{ij} \tag{2.5}$$

where δ_{ij} is the Kronecker delta, which means that if $i = j$, it takes the value 1, and 0 otherwise. Reciprocal lattice vector can be defined with primitive vectors as follows

$$\mathbf{G} = m_1\mathbf{b_1} + m_2\mathbf{b_2} + m_3\mathbf{b_3} \tag{2.6}$$

where m_i are any integers. To summarize, real space lattice vectors are used to calculate the reciprocal lattice vectors and obtain the reciprocal lattice. Afterwards, any lattice point in the

reciprocal lattice can be used as the origin when constructing the Brillouin zone (BZ). This point should be the center of the BZ. The smallest volume completely surrounded by planes that are the reciprocal lattice vectors' perpendicular bisectors is known as the first BZ. The first BZ is a primitive cell in the reciprocal lattice and it is the geometric equivalent of the Wigner-Seitz cell in real space [6,76,77]. BZs diagram for the 2D square reciprocal lattice is shown in Figure 2.5. As it can be seen in Figure 2.5, the first BZ contains frequencies with wave vector values from 0 to π/a, for frequencies that move in the $\pm x$ and $\pm y$ directions.

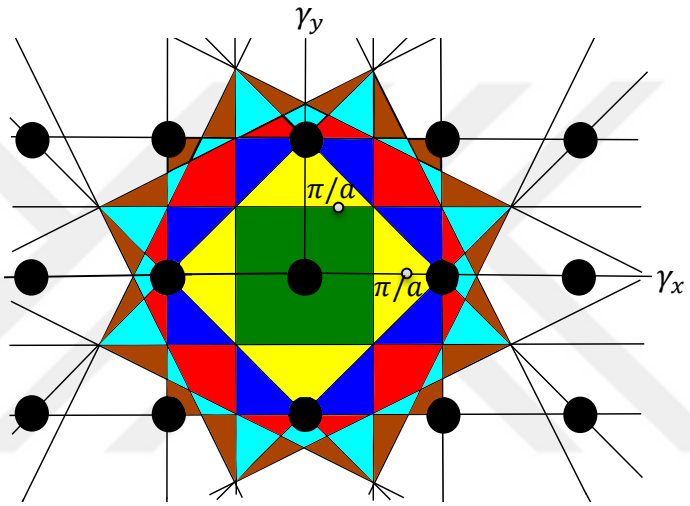


Figure 2.5. The first six BZs of a 2D square lattice. The green color denotes the first BZ, and each color indicates the next BZ.

The first BZ has all the information of the whole structure and the other BZs are not used for band structure calculations. The first BZ is therefore frequently referred to as simply the BZ. The first BZ that cannot be minimized by any of the symmetries in the point group of the lattice is known as the Irreducible Brillouin Zone (IBZ). Instead of calculating the phonon band structure of the whole region in 2D or the volume in 3D, the band structure is analyzed by following a route around the edge of the IBZ. This method also reduces the computational cost. The BZ, IBZ, and the phonon band structure of a square unit cell with a circular inclusion is shown in Figure 2.6. Here, a graph showing the phonon band structure of the unit cell is obtained, considering waves with wave vectors in the triangular path Γ, X, M, Γ. The triangle with corners Γ, X, M represents the first BZ thanks to the symmetry operations.

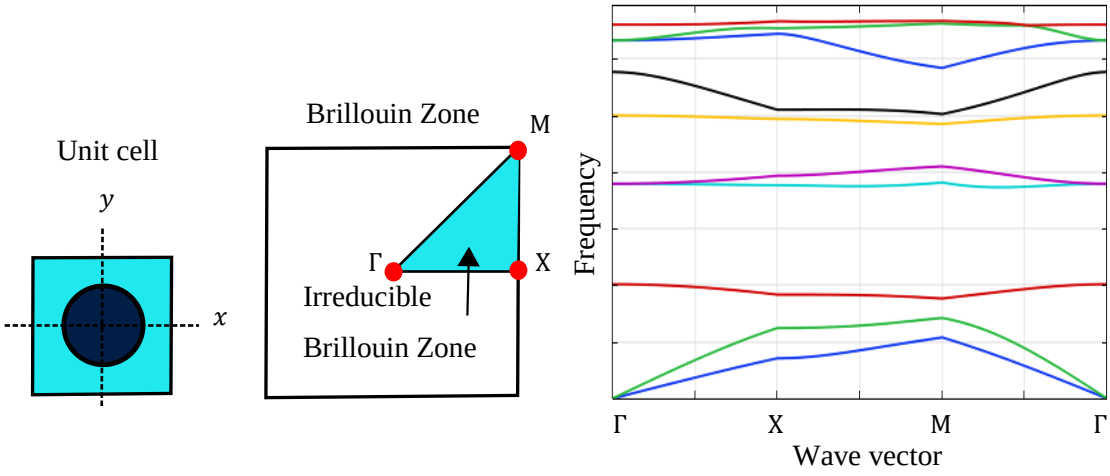


Figure 2.6. (a) A square unit cell with a circular inclusion, (b) the corresponding BZ and IBZ of the unit cell, and (c) the phonon band structure of the unit cell calculated by following a route around the edge of the IBZ.

2.1.3. 1D Uniform Periodic Structure

The periodic structure of the 1D mass-spring structure is shown in Figure 2.7.

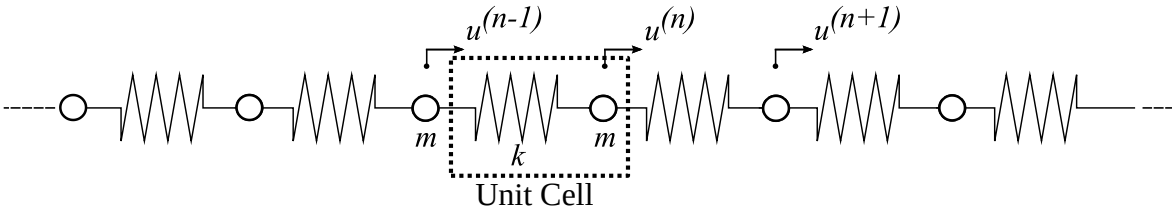


Figure 2.7. 1D uniform periodic structure.

The equation of motion for the n^{th} particle is written by using Netwon's law as

$$m\ddot{u}^{(n)} = k\left(u^{(n+1)} - u^{(n)}\right) - k\left(u^{(n)} - u^{(n-1)}\right) \tag{2.7}$$

where m is the mass, k is the spring constant, and $u^{(n)}$ is the displacement of the n^{th} particle. The equation of motion can be written assuming $u(t) = e^{i\omega t}$ and $\ddot{u}(t) = -\omega^2 e^{i\omega t}$ as

$$\omega^2 m u^{(n)} + k\left(u^{(n+1)} - u^{(n)}\right) - k\left(u^{(n)} - u^{(n-1)}\right) = 0. \tag{2.8}$$

Using Bloch's theorem in Equation (2.2), the expressions $u^{(n+1)}, u^{(n-1)}$ can be written in terms of u^n. After the substitutions, the equation of motion is found as follows

$$k\left(2 - e^{i\gamma a} - e^{-i\gamma a}\right)u - \omega^2 m u = 0. \tag{2.9}$$

When this eigenvalue problem is solved with the following parameters using γ values for ω in the range of $-2\pi/a, 2\pi/a$, the band structure of the system is found as in Figure 2.8. As seen here, the band gap is not found for this system and first BZ is marked.

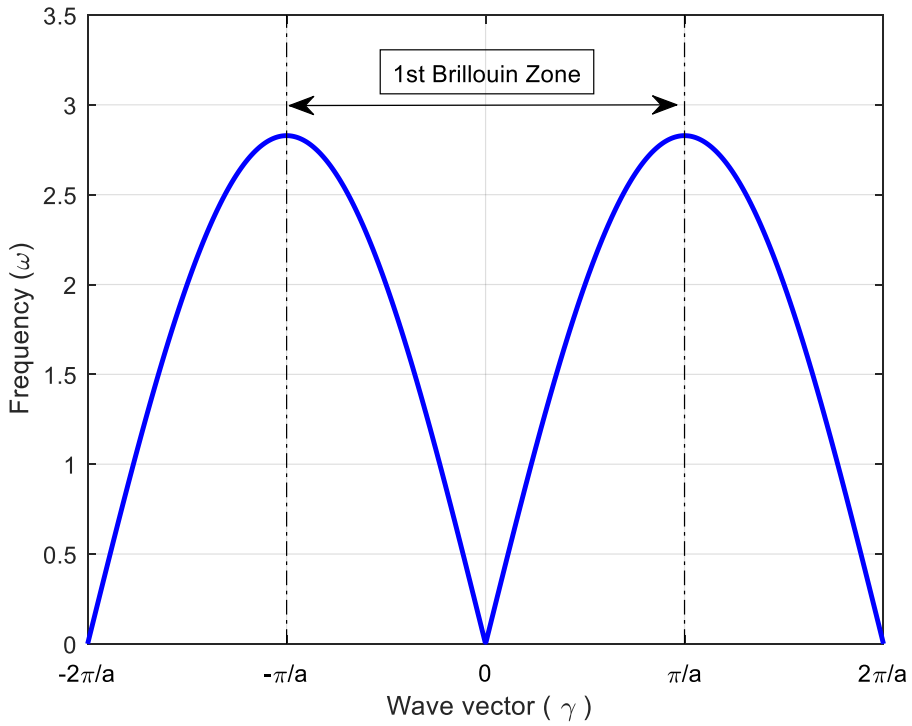


Figure 2.8. Phonon band structure of a 1D uniform periodic mass spring system for the parameters $m = 1, k = 2, a = 1$.

2.2. Band Gap Generation Methods

In the literature, band gaps in periodic structures are often created by Bragg scattering, local resonance, and inertial amplification methods. In this section, these three band gap generation methods are explained and the comparison of the band structures of these methods obtained using the same parameters is given.

2.2.1. Bragg Scattering Method

The 1D periodic structure formed by two different masses that repeat themselves periodically is shown in Figure 2.9. This is a typical Bragg scattering model. Also note that band gaps in this method can be created by changing the stiffness elements instead of the mass elements.

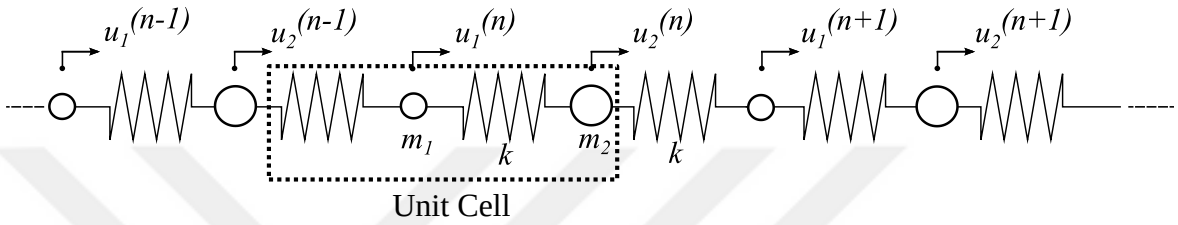


Figure 2.9. 1D periodic structure with two different masses and uniform springs.

The equations of motion for two masses can be expressed as follows, assuming $u(t) = e^{i\omega t}$

$$k\left(u_1^{(n)} - u_2^{(n+1)}\right) + k\left(u_1^{(n)} - u_2^{(n)}\right) - \omega^2 m_1 u_1^{(n)} = 0 \qquad (2.10)$$

$$k\left(u_2^{(n)} - u_1^{(n)}\right) + k\left(u_2^{(n)} - u_1^{(n-1)}\right) - \omega^2 m_2 u_2^{(n)} = 0. \qquad (2.11)$$

When these expressions are substituted in Bloch's theorem in Equation (2.2), the matrix form is obtained as follows

$$\begin{bmatrix} 2k & -k(1+e^{i\gamma a}) \\ -k(1+e^{-i\gamma a}) & 2k \end{bmatrix} \begin{bmatrix} u_1 \\ u_2 \end{bmatrix} - \omega^2 \begin{bmatrix} m_1 & 0 \\ 0 & m_2 \end{bmatrix} \begin{bmatrix} u_1 \\ u_2 \end{bmatrix} = 0 \qquad (2.12)$$

where

$$\mathbf{M} = \begin{bmatrix} m_1 & 0 \\ 0 & m_2 \end{bmatrix} \quad , \quad \mathbf{K} = \begin{bmatrix} 2k & -k(1+e^{i\gamma a}) \\ -k(1+e^{-i\gamma a}) & 2k \end{bmatrix}. \qquad (2.13)$$

The solution to the problem can be written in compact form $(\mathbf{K} - \omega^2\mathbf{M})\mathbf{u} = 0$ as

$$\begin{bmatrix} +2k - \omega^2 m_1 & -k(1+e^{i\gamma a}) \\ -k(1+e^{-i\gamma a}) & +2k - \omega^2 m_2 \end{bmatrix} \begin{bmatrix} u_1 \\ u_2 \end{bmatrix} = \begin{bmatrix} 0 \\ 0 \end{bmatrix}. \qquad (2.14)$$

The result of this eigenvalue problem is found with $\det(\mathbf{K} - \omega^2\mathbf{M}) = 0$.

When this eigenvalue problem is solved with the following parameters using γ values for ω in the range of $-2\pi/a, 2\pi/a$ the band structure of the system is found as shown in Figure 2.10. As seen in Figure 2.10, the band gap for this structure is between 1.41 and 2.00 and the band gap and first BZ are marked.

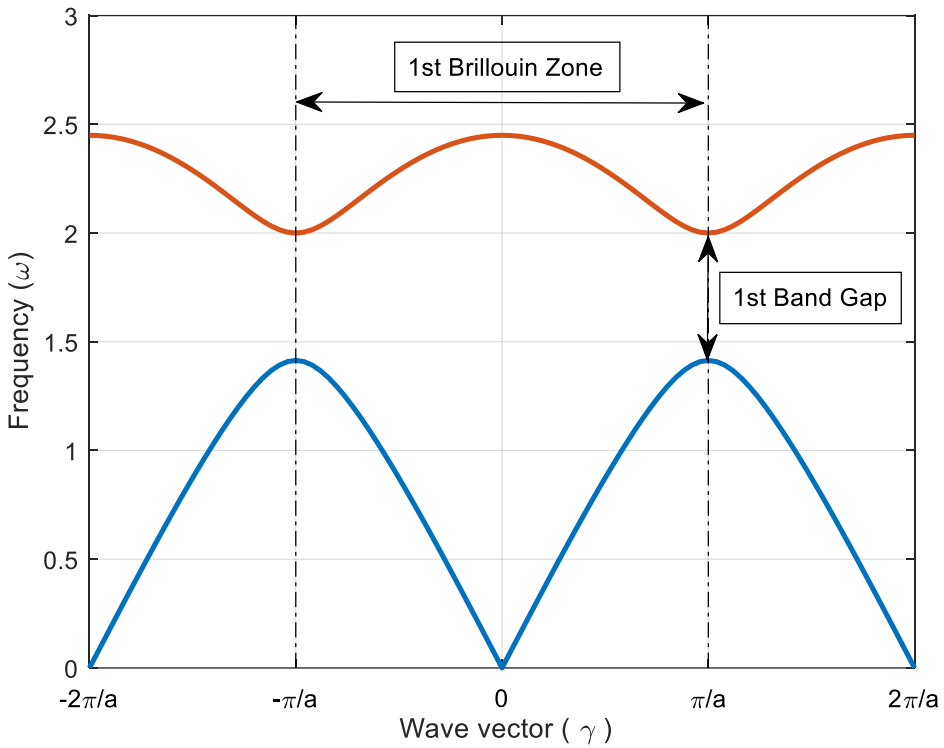


Figure 2.10. Phonon band structure of a 1D periodic structure with different masses and uniform springs system for the parameters $m_1 = 1, m_2 = 2, k = 2, a = 1$.

2.2.2. Local Resonance Method

This method uses the effect of coupling oscillators to generate band gaps and therefore local resonators are added to a main structure. Band gaps occur around the natural frequencies of the resonators in this method. 1D periodic structure of the local resonance model is shown in Figure 2.11. A small mass that is connected to the host structure by a spring is an illustration of a local resonator.

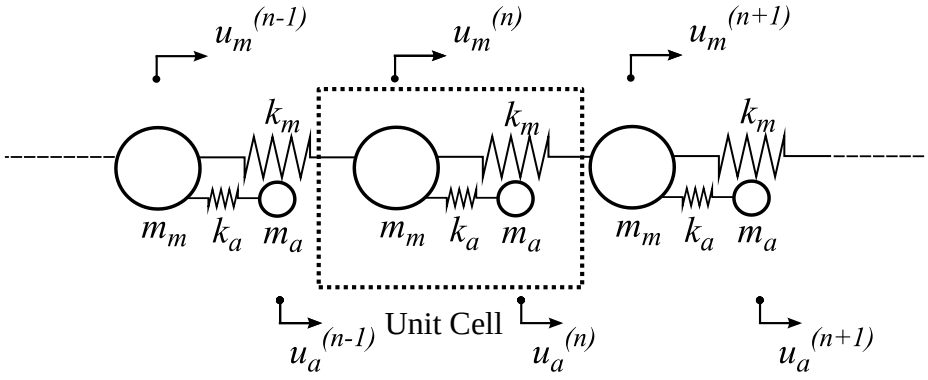


Figure 2.11. 1D periodic structure of the local resonance model.

The equation of motion of the unit cell of the local resonance model can be written as follows

$$m_m \ddot{u}_m{}^{(n)} + k_m\left(2u_m^n - u_m^{(n-1)} - u_m^{(n+1)}\right) + k_a(u_m^n - u_a^n) = 0 \quad (2.15)$$

$$m_a \ddot{u}_a{}^{(n)} + k_a(u_a^n - u_m^n) = 0. \quad (2.16)$$

By applying Bloch's theorem to Equations (2.15) and (2.16), the equation of motion is written as follows

$$m_m \ddot{u}_m{}^{(n)} + k_m u_m^n\left(2 - e^{-i\gamma a} - e^{i\gamma a}\right) + k_a(u_m^n - u_a^n) = 0 \quad (2.17)$$

$$m_a \ddot{u}_a{}^{(n)} + k_a(u_a^n - u_m^n) = 0. \quad (2.18)$$

The equation of motion of the system can be solved by assuming $x(t) = e^{i\omega t}$. The band structure can be obtained by solving the eigenvalue problem with $\det(\mathbf{K} - \omega^2\mathbf{M}) = 0$. When this eigenvalue problem is solved with the following parameters using γ values for ω in the range of $-2\pi/a, 2\pi/a$ the band structure of the system is found as shown in Figure 2.12. The band gap for this structure is between 1.02 and 2.12 and first band gap and first BZ are marked in the figure.

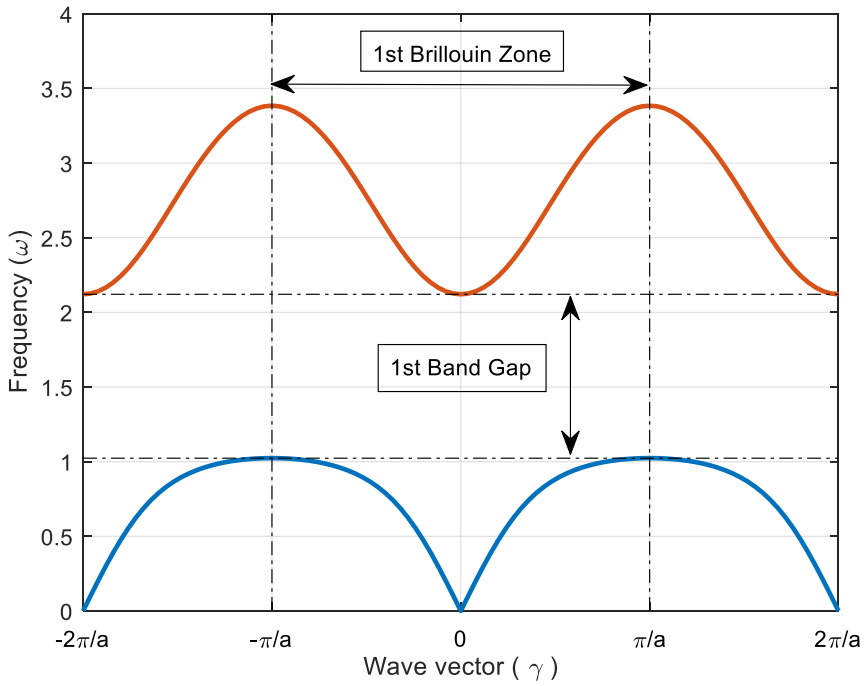


Figure 2.12. Band structure of the 1D periodic structure of the local resonance model for the parameters $m_m = 1$, $m_a = 2$, $k_m = 2$, $k_a = 3$, $a = 1$.

2.2.3. Inertial Amplification Mechanism

The lumped parameter model that explains the fundamental idea of the mechanism is shown in Figure 2.13. As seen in Figure 2.13, there are two masses, m_x, that are attached to one another by a spring of stiffness k. Rigid linkages connect the masses, m_x, and the mass, m_a. The angle between the spring and the stiff links is represented as θ.

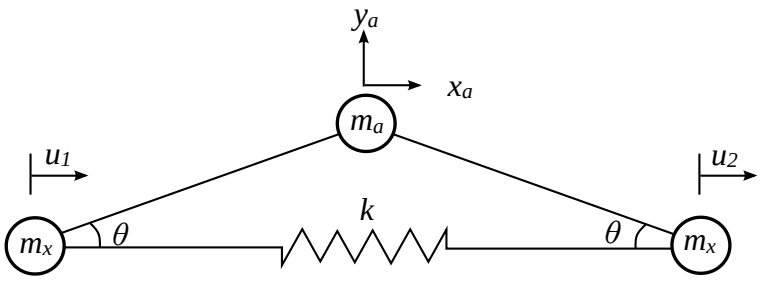


Figure 2.13. Lumped parameter of the inertial amplification mechanism.

The displacement of m_a can be calculated in terms of u_1 and u_2 by using u_1 as the input displacement and u_2 as the output displacement of the mechanism as

$$x_a = \frac{u_1 + u_2}{2} \tag{2.19}$$

$$y_a = \frac{(u_1 - u_2)}{2}\cot(\theta). \tag{2.20}$$

It can be seen that the DOF of the system is one. The equation of motion of the system is determined as follows by considering u_1 and u_2 displacements, which are very small in comparison to the size of the mechanism as [43, 54]

$$\left(\frac{m_a\,(\cot^2(\theta)+1)}{4} + m_x\right)\ddot{u}_2 + ku_2 = \left(\frac{m_a\,(\cot^2(\theta)-1)}{4}\right)\ddot{u}_1 + ku_1. \tag{2.21}$$

The resonance frequency can be written as

$$\omega_p = \sqrt{\frac{k}{m_x + m_a\,(\cot^2(\theta)+1)/4}}. \tag{2.22}$$

Similarly, the antiresonance frequency can be calculated as

$$\omega_z = \sqrt{\frac{k}{m_a\,(\cot^2(\theta)-1)/4}}. \tag{2.23}$$

The displacement transmissibility of the mechanism can be written as

$$T(\omega) = \frac{output}{input} = \frac{k - \left(\frac{m_a\,(\cot^2(\theta)-1)}{4}\right)\omega^2}{k - \left(\left(\frac{m_a\,(\cot^2(\theta)+1)}{4}\right) + m_x\right)\omega^2}. \tag{2.24}$$

By dividing both the nominator and denominator by *k*, the displacement transmissibility can be calculated as

$$T(\omega) = \frac{1 - \frac{\omega^2}{\omega_z^2}}{1 - \frac{\omega^2}{\omega_p^2}} \tag{2.25}$$

where ω_p, ω_z, and ω are the resonance, antiresonance, and excitation frequencies, respectively. When $T(\omega)$ is smaller than 1, it is called stop band or band gap. Band gap begins right above the resonance frequency and goes to infinity for the 1D lumped parameter of the inertial amplification mechanism, which will be detailed in the following pages.

The 1D periodic structure of the lumped parameter inertial amplification mechanism is shown in Figure 2.14.

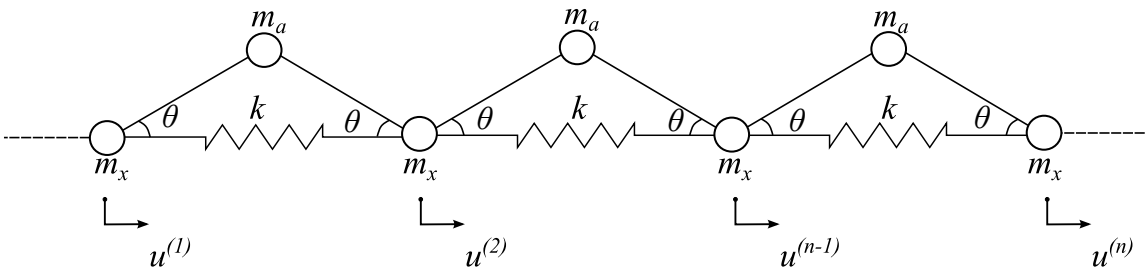


Figure 2.14. 1D periodic structure of the lumped parameter inertial amplification mechanism.

The equation of motion of the unit cell of the inertial amplification mechanism can be written as

$$\left(\frac{m_a\,(\cot^2(\theta)+1)}{4}+m_x\right)\ddot{u}^{(n)}+ku^{(n)}=\left(\frac{m_a\,(\cot^2(\theta)-1)}{4}\right)\ddot{u}^{(n-1)} +ku^{(n-1)}. \qquad (2.26)$$

After applying Bloch's theorem, the equation of motion can be written as

$$\left[\left(\frac{m_a\,(\cot^2(\theta)+1)}{4}+m_x\right)-\left(\frac{m_a\,(\cot^2(\theta)-1)}{4}\right)e^{-i\gamma\alpha}\right]\ddot{u}^{(n)} +k\left(1-e^{-i\gamma\alpha}\right)u^{(n)}=0. \qquad (2.27)$$

The equation of motion of the system can be solved by assuming $u(t)=e^{i\omega t}$. The band structure of the mechanism can be obtained by solving the eigenvalue problem with $\det(\mathbf{K}-\omega^2\mathbf{M})=0$. When this eigenvalue problem is solved with the following parameters using γ values for ω in the range of $0,\pi/a$ the band structure of the system is found as shown in Figure 2.15. Note that total mass is $m_t=m_x+m_a$. For easy interpretation of the figure, the total mass is set the same for all cases.

As noted in Figure 2.15, it is clear that the band gap begins at lower frequencies when θ and m_x are smaller. Moreover, the denominator of the resonance frequency of the mechanism has m_a multiplied by $(cot^2(\theta)+1)/4$. When θ decreases, $(cot^2(\theta)+1)/4$ increases. Therefore, a small mass, m_a, has a greater impact on the system than its static

value. Thanks to this technique, band gaps are created at lower frequencies that Bragg scattering or local resonance methods cannot achieve without increasing the overall mass of the system [42,43,45,47,54].

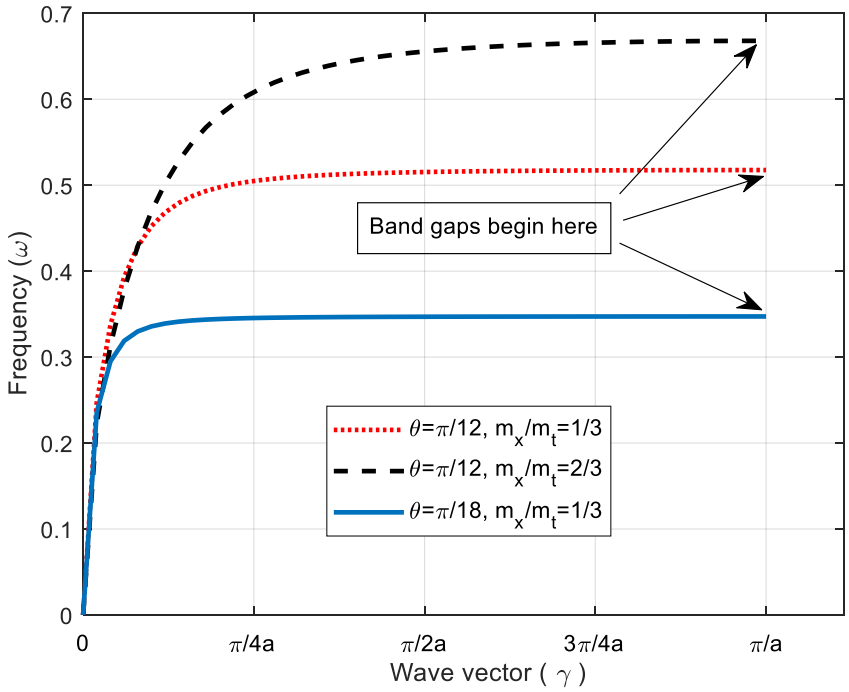


Figure 2.15. Band structure of the 1D periodic structure of the lumped parameter inertial amplification mechanisms for $m_x/m_t = 1/3$, $\theta = \pi/12$, $m_x/m_t = 2/3$, $\theta = \pi/12$, and $m_x/m_t = 1/3$, $\theta = \pi/18$. For all cases, $k = 2$, $a = 1$.

2.2.4. Comparison of Band Gap Generation Methods

Figure 2.16 illustrates the comparison of the band structures of the three methods for $m_x = m_1 = m_m = 1$, $m_2 = m_a = 2$, $\theta = \pi/12$, $k = 2$, $k_a = 3$, $a = 1$. As can be seen clearly, all parameters are chosen the same for easy comparison of the methods.

Eigenvalue problem is solved with the parameters using γ values for ω in the range of $0, \pi/a$. As seen in Figure 2.16, band gaps created by inertial amplification mechanisms start at lower frequencies than that of Bragg scattering and local resonance methods. Also, both Bragg scattering and local resonance methods have two branches, whereas inertial amplification mechanism has only one branch because the mechanism has one DOF for the lumped model. The inertial amplification mechanism is therefore considered as a semi-

infinite band gap [78]. Although there is only one resonance frequency in the lumped parameter model, finite element model of the mechanism will include many resonance frequencies. The ratio of the first two resonance frequencies (ω_{p2}/ω_{p1}) will thereby be maximized to obtain the widest band gap.

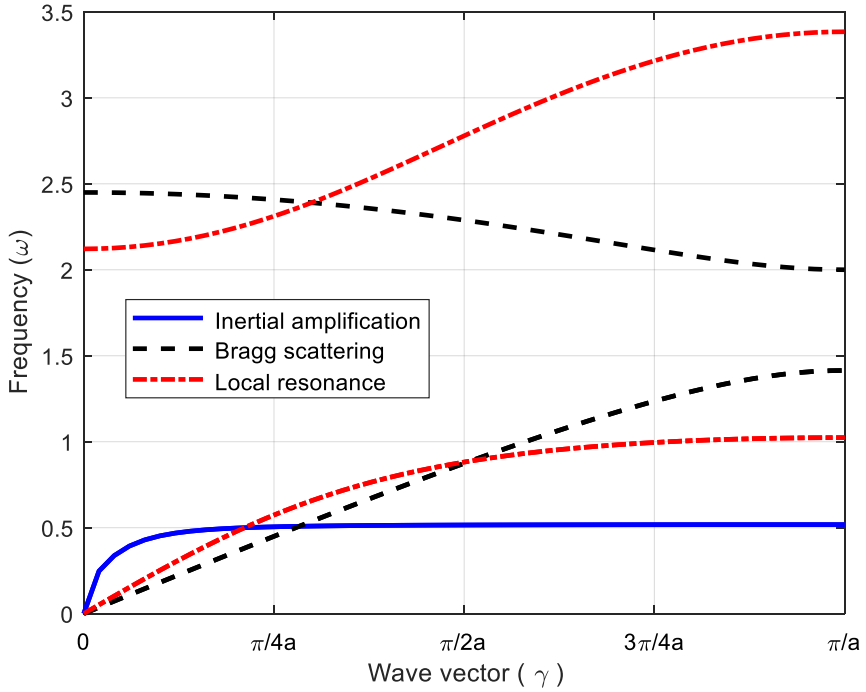


Figure 2.16. Comparison of the band structures of the inertial amplification, Bragg scattering and local resonance methods for $m_x = m_1 = m_m = 1$, $m_2 = m_a = 2$, $\theta = \pi/12$, $k = 2$, $k_a = 3$, $a = 1$.

2.3. Bloch Boundary Condition in the Finite Element Method

In this section, 1D, 2D, and 3D Bloch boundary conditions (BCs) are explained in the FEM. To apply Bloch's theorem, DOFs on the unit cell's boundaries must be connected to each other with phase terms relying on the wave vector. A 2D unit cell FE mesh showing the DOFs of the nodes required for applying the 1D Bloch BC is shown in Figure 2.17. The details of these derivations can be found in Refs. [13,79].

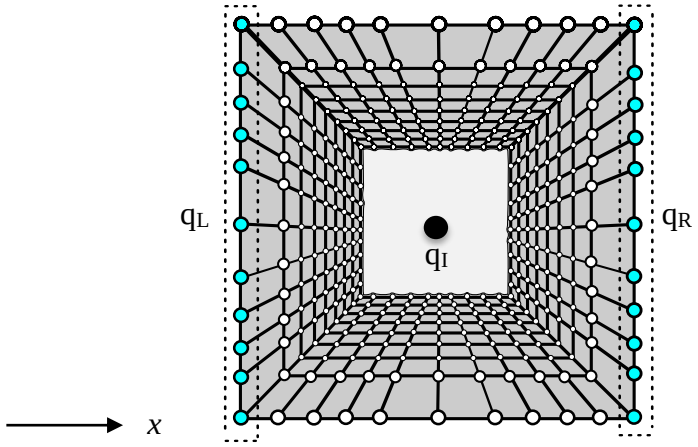


Figure 2.17. A 2D unit cell FE mesh showing the DOFs of the nodes required to apply the 1D Bloch BC. In the unit cell, the subscript L denotes left, I=internal, R= right. All nodes that are not on the left and right boundaries are considered internal nodes.

The DOFs on the right boundary are linked to the DOFs on the left boundary for the 1D case. The corresponding DOFs are shown in Figure 2.17 with the same light blue color and Bloch BC can be written between these nodes as follows

$$q_R = \lambda_x q_L \tag{2.28}$$

where $\lambda_x = e^{i\gamma_x a_x}$. a_x and γ_x denote the translation vector component, and the wave vector component, respectively. The relations can be written in matrix form as follows

$$\underbrace{\begin{bmatrix} q_L \\ q_R \\ q_I \end{bmatrix}}_{\mathbf{q}} = \underbrace{\begin{bmatrix} \mathbf{I_L} & 0 \\ \lambda_x \mathbf{I_L} & 0 \\ 0 & \mathbf{I_I} \end{bmatrix}}_{\mathbf{P}} \underbrace{\begin{bmatrix} q_L \\ q_I \end{bmatrix}}_{\breve{\mathbf{q}}} \tag{2.29}$$

where $\mathbf{q}$, $\mathbf{P}$, and $\breve{\mathbf{q}}$ indicate the free DOF vector, the Bloch periodicity matrix, and the reduced DOF vector, respectively. Note that $\mathbf{I_L}$ and $\mathbf{I_I}$ are identity matrices with subscript *I* and *L* indicating the boundary.

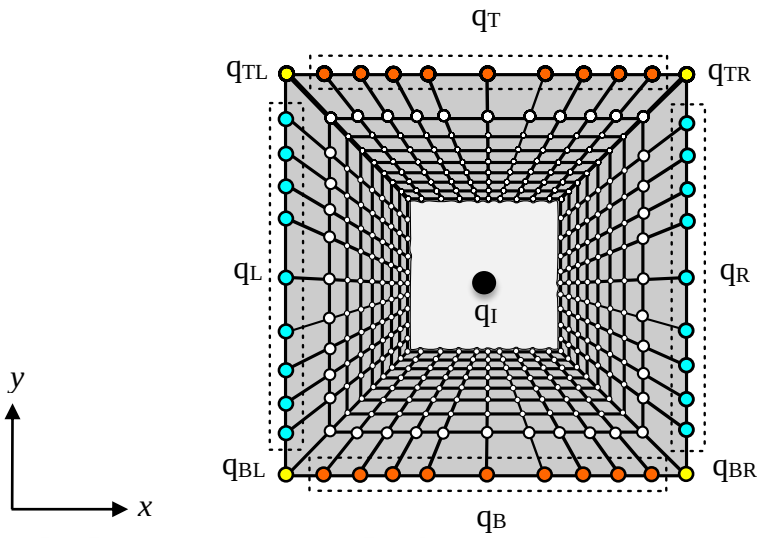


Figure 2.18. A 2D unit cell FE mesh showing the DOFs of the nodes required to apply the 2D Bloch BC. In the unit cell, the subscript L denotes left, I=internal, R= right, T=top, B=bottom. All nodes that are not in the perimeter are conside”red internal nodes.

In 2D, the DOFs on the boundaries and corners must be taken into account when applying Bloch's theorem. The corresponding DOFs marked with the same colors are shown in Figure 2.18. The DOFs with the same colors are connected to each other with Bloch BC, and Bloch BC can be written between these DOFs.

The relations between the corresponding DOFs on the boundaries can be written as

$$q_R = \lambda_x q_L,\ q_T = \lambda_y q_B. \tag{2.30}$$

Similarly, the relationships between the corresponding corner DOFs can be written as follows

$$q_{BR} = \lambda_x q_{BL},\ q_{TL} = \lambda_y q_{BL},\ q_{TR} = \lambda_x \lambda_y q_{BL} \tag{2.31}$$

where $\lambda_x = e^{i\gamma_x a_x}$, and $\lambda_y = e^{i\gamma_y a_y}$. a_x, a_y are the translation vector components, and γ_x, γ_y denote the wave vector components.

The relations can be written in matrix form as follows

$$\underbrace{\begin{bmatrix} q_L \\ q_R \\ q_B \\ q_T \\ q_{BL} \\ q_{BR} \\ q_{TL} \\ q_{TR} \\ q_I \end{bmatrix}}_{\mathbf{q}} = \underbrace{\begin{bmatrix} \mathbf{I_L} & 0 & 0 & 0 \\ \lambda_x \mathbf{I_L} & 0 & 0 & 0 \\ 0 & \mathbf{I_B} & 0 & 0 \\ 0 & \lambda_y \mathbf{I_B} & 0 & 0 \\ 0 & 0 & \mathbf{I_{BL}} & 0 \\ 0 & 0 & \lambda_x \mathbf{I_{BL}} & 0 \\ 0 & 0 & \lambda_y \mathbf{I_{BL}} & 0 \\ 0 & 0 & \lambda_x \lambda_y \mathbf{I_{BL}} & 0 \\ 0 & 0 & 0 & \mathbf{I_I} \end{bmatrix}}_{\mathbf{P}} \underbrace{\begin{bmatrix} q_L \\ q_B \\ q_{BL} \\ q_I \end{bmatrix}}_{\breve{\mathbf{q}}} \tag{2.32}$$

where $\mathbf{I_L}$, $\mathbf{I_B}$, $\mathbf{I_{BL}}$, and $\mathbf{I_I}$ are identity matrices with subscripts representing the left, bottom, bottom left corner, and internal.

In 3D, Bloch's theorem can be tricky to implement because DOFs exist not only on the boundaries and corners but also on surfaces, and they all need to be considered. The corresponding DOFs marked with the same colors are shown in Figure 2.19. The DOFs with the same colors are connected to each other with Bloch BC.

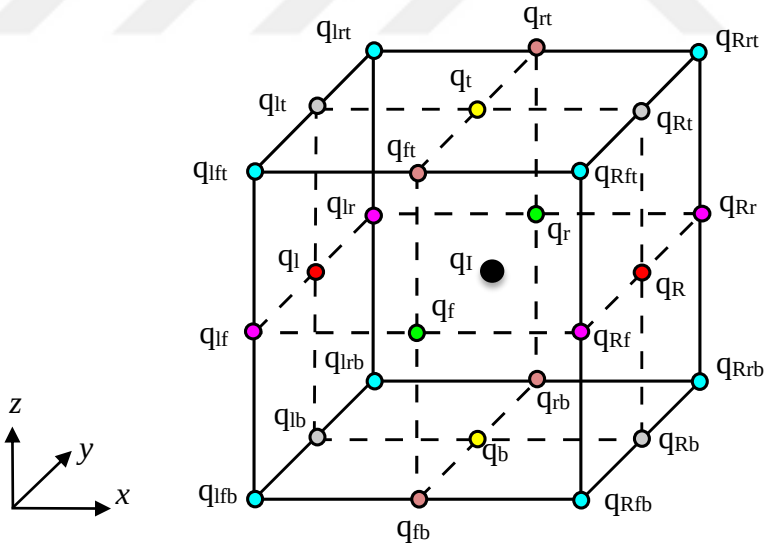


Figure 2.19. A 3D unit cell FE mesh showing the DOFs of the nodes required to apply the 3D Bloch BC. The subscript l represents left, R=right, f=front, r=rear, b=bottom, t=top, I=internal. All nodes not explicitly specified are considered internal nodes.

Surface nodal DOFs are indicated by single subscripts, boundary nodal DOFs by double subscripts, and corner nodal DOFs by triple subscripts. Note that surface nodes are a

group of nodes that do not include nodes on the boundaries and corners. Similarly, boundary nodes are a group of nodes with no nodes on the corners. Bloch BCs can be written between the corresponding DOFs on the surfaces, boundaries, and corners.

The relations between the corresponding DOFs on the surfaces can be written as

$$q_R = \lambda_x q_l, \qquad q_r = \lambda_y q_f, \qquad q_t = \lambda_z q_b. \tag{2.33}$$

Likewise, the relations between the corresponding DOFs on the boundaries can be written as follows

$$q_{Rf} = \lambda_x q_{lf}, \qquad q_{lr} = \lambda_y q_{lf}, \qquad q_{Rr} = \lambda_x \lambda_y q_{lf} \tag{2.34}$$
$$q_{rb} = \lambda_y q_{fb}, \qquad q_{ft} = \lambda_z q_{fb}, \qquad q_{rt} = \lambda_y \lambda_z q_{fb} \tag{2.35}$$
$$q_{Rb} = \lambda_x q_{lb}, \qquad q_{lt} = \lambda_z q_{lb}, \qquad q_{Rt} = \lambda_x \lambda_z q_{lb}. \tag{2.36}$$

Similarly, the relationships between the corresponding corner DOFs can be written as follows

$$q_{Rrb} = \lambda_x \lambda_y q_{lfb}, \quad q_{Rft} = \lambda_x \lambda_z q_{lfb}, \quad q_{lrt} = \lambda_y \lambda_z q_{lfb} \tag{2.37}$$
$$q_{Rfb} = \lambda_x q_{lfb}, \quad q_{lrb} = \lambda_y q_{lfb}, \quad q_{lft} = \lambda_z q_{lfb}, \quad q_{Rrt} = \lambda_x \lambda_y \lambda_z q_{lfb} \tag{2.38}$$

where $\lambda_x = e^{i\gamma_x a_x}$,$\lambda_y = e^{i\gamma_y a_y}$,$\lambda_z = e^{i\gamma_z a_z}$, and a_x, a_y, a_z are translation vector components, and γ_x, γ_y, γ_z denote the wave vector components.

The relations can be written in matrix form as follows

$$\underbrace{\begin{bmatrix} q_l \\ q_R \\ q_f \\ q_r \\ q_b \\ q_t \\ q_{lf} \\ q_{Rf} \\ q_{lr} \\ q_{Rr} \\ q_{fb} \\ q_{rb} \\ q_{ft} \\ q_{rt} \\ q_{lb} \\ q_{Rb} \\ q_{lt} \\ q_{Rt} \\ q_{lfb} \\ q_{Rfb} \\ q_{lrb} \\ q_{lft} \\ q_{Rrb} \\ q_{Rft} \\ q_{lrt} \\ q_{Rrt} \\ q_I \end{bmatrix}}_{\mathbf{q}} = \underbrace{\begin{bmatrix} \mathbf{I_l} & 0 & 0 & 0 & 0 & 0 & 0 & 0 \\ \lambda_x\mathbf{I_l} & 0 & 0 & 0 & 0 & 0 & 0 & 0 \\ 0 & \mathbf{I_f} & 0 & 0 & 0 & 0 & 0 & 0 \\ 0 & \lambda_y\mathbf{I_f} & 0 & 0 & 0 & 0 & 0 & 0 \\ 0 & 0 & \mathbf{I_b} & 0 & 0 & 0 & 0 & 0 \\ 0 & 0 & \lambda_z\mathbf{I_b} & 0 & 0 & 0 & 0 & 0 \\ 0 & 0 & 0 & \mathbf{I_{lf}} & 0 & 0 & 0 & 0 \\ 0 & 0 & 0 & \lambda_x\mathbf{I_{lf}} & 0 & 0 & 0 & 0 \\ 0 & 0 & 0 & \lambda_y\mathbf{I_{lf}} & 0 & 0 & 0 & 0 \\ 0 & 0 & 0 & \lambda_x\lambda_y\mathbf{I_{lf}} & 0 & 0 & 0 & 0 \\ 0 & 0 & 0 & 0 & \mathbf{I_{fb}} & 0 & 0 & 0 \\ 0 & 0 & 0 & 0 & \lambda_y\mathbf{I_{fb}} & 0 & 0 & 0 \\ 0 & 0 & 0 & 0 & \lambda_z\mathbf{I_{fb}} & 0 & 0 & 0 \\ 0 & 0 & 0 & 0 & \lambda_y\lambda_z\mathbf{I_{fb}} & 0 & 0 & 0 \\ 0 & 0 & 0 & 0 & 0 & \mathbf{I_{lb}} & 0 & 0 \\ 0 & 0 & 0 & 0 & 0 & \lambda_x\mathbf{I_{lb}} & 0 & 0 \\ 0 & 0 & 0 & 0 & 0 & \lambda_z\mathbf{I_{lb}} & 0 & 0 \\ 0 & 0 & 0 & 0 & 0 & \lambda_x\lambda_z\mathbf{I_{lb}} & 0 & 0 \\ 0 & 0 & 0 & 0 & 0 & 0 & \mathbf{I_{lfb}} & 0 \\ 0 & 0 & 0 & 0 & 0 & 0 & \lambda_x\mathbf{I_{lfb}} & 0 \\ 0 & 0 & 0 & 0 & 0 & 0 & \lambda_y\mathbf{I_{lfb}} & 0 \\ 0 & 0 & 0 & 0 & 0 & 0 & \lambda_z\mathbf{I_{lfb}} & 0 \\ 0 & 0 & 0 & 0 & 0 & 0 & \lambda_x\lambda_y\mathbf{I_{lfb}} & 0 \\ 0 & 0 & 0 & 0 & 0 & 0 & \lambda_x\lambda_z\mathbf{I_{lfb}} & 0 \\ 0 & 0 & 0 & 0 & 0 & 0 & \lambda_y\lambda_z\mathbf{I_{lfb}} & 0 \\ 0 & 0 & 0 & 0 & 0 & 0 & \lambda_x\lambda_y\lambda_z\mathbf{I_{lfb}} & 0 \\ 0 & 0 & 0 & 0 & 0 & 0 & 0 & \mathbf{I_I} \end{bmatrix}}_{\mathbf{P}} \underbrace{\begin{bmatrix} q_l \\ q_f \\ q_b \\ q_{lf} \\ q_{fb} \\ q_{lb} \\ q_{lfb} \\ q_I \end{bmatrix}}_{\breve{\mathbf{q}}} \quad (2.39)$$

where $\mathbf{I_l}$, $\mathbf{I_f}$, $\mathbf{I_b}$, $\mathbf{I_{lf}}$, $\mathbf{I_{fb}}$, $\mathbf{I_{lb}}$, $\mathbf{I_{lfb}}$ and $\mathbf{I_I}$ are identity matrices. After writing the Bloch BC in one, two and three dimensions in matrix form, the Bloch periodicity matrix, **P**, can be divided into parts for easy computation.

The 1D Bloch periodicity matrix written in Equation (2.29) can be divided into parts as

$$\mathbf{P} = \mathbf{P_0} + \mathbf{P_x}\lambda_x. \quad (2.40)$$

Similarly, the 2D Bloch periodicity matrix found in Equation (2.32) can be written as

$$\mathbf{P} = \mathbf{P_0} + \mathbf{P_x}\lambda_x + \mathbf{P_y}\lambda_y + \mathbf{P_x}\lambda_x + \mathbf{P_{xy}}\lambda_x\lambda_y. \quad (2.41)$$

Likewise, the 3D Bloch periodicity matrix stated in Equation (2.39) can be written as

$$\mathbf{P} = \mathbf{P_0} + \mathbf{P_x}\lambda_x + \mathbf{P_y}\lambda_y + \mathbf{P_z}\lambda_z + \mathbf{P_{xy}}\lambda_x\lambda_y + \mathbf{P_{xz}}\lambda_x\lambda_z + \mathbf{P_{yz}}\lambda_y\lambda_z + \mathbf{P_{xyz}}\lambda_x\lambda_y\lambda_z. \quad (2.42)$$

Mass and stiffness matrices are then pre-multiplied by $\mathbf{P^T}$ and post-multiplied **P** to obtain reduced mass and stiffness matrices as

$$\mathbf{K_R} = \mathbf{P^T K P} \quad (2.43)$$

$$\mathbf{M_R} = \mathbf{P^T M P} \quad (2.44)$$

where $\mathbf{P^T}$ is the Hermitian transpose of **P**, the **K** and **M** are the stiffness and mass matrices generated by a commercial finite element software package.

The eigenvalue problem can then be solved by assuming the time harmonic solution $\breve{\mathbf{q}} = \bar{\bar{\mathbf{q}}}e^{iwt}$. Then, the phonon band structure frequencies can be calculated as follows

$$(\mathbf{K_R} - \omega^2\mathbf{M_R})\breve{\mathbf{q}} = 0 \quad (2.45)$$

where $\mathbf{M_R}$, $\mathbf{K_R}$, ω and $\breve{\mathbf{q}}$ indicate the reduced mass matrix, reduced stiffness matrix, frequency, and the reduced DOF vector, respectively.

2.3.1. Implementation of Bloch Boundary Condition in the FEM

In the literature, there are three different methods that are used to apply Bloch's theorem in the FEM. All three different methods are explained below.

- The first method is to take mass, **M**, and stiffness, **K**, matrices from a finite element software (e.g. ABAQUS) and use them in a computer program (e.g. MATLAB), then implement Bloch's theorem between the corresponding nodes and solve the eigenvalue problem [45,47,51,79]. This is the most common method used for band structure calculations.
- The second method is to apply Bloch's Theorem directly between the corresponding nodes in a finite element software (e.g. in the Solid Mechanics module in COMSOL Multiphysics program). This method does not need to import **K** and **M** matrices from other FE package programs. All analyses including obtaining the phonon band structure can be performed by using COMSOL Multiphysics [68,70-73].

- The third method is to implement Bloch BCs using a user-defined subroutine multipoint constraints (MPC) in ABAQUS. Note that this method requires to duplicate mesh to take into account the real and imaginary parts [78,80-84]. Details will be given on the following pages.

As a first method, **K** and **M** matrices are generated from ABAQUS. The following lines are written at the end of the Input file as

- *STEP
- *MATRIX GENERATE, STIFFNESS, MASS
- *MATRIX OUTPUT, STIFFNESS, MASS, FORMAT=MATRIX INPUT
- *END STEP.

After that, the following line is written in Windows PowerShell to execute the process

- abaqus j= Job-1 int

where Job-1 is the name of the input file. In this way, ABAQUS generates two text files named Job-1_MASS2.mtx and Job-1_STIF2.mtx. ABAQUS or any other FE software package program generates the mass and stiffness matrices by using the direct stiffness method, also called the matrix stiffness method. After exporting **K** and **M** matrices from ABAQUS, a MATLAB code is written to load the matrices into MATLAB and solve the eigenvalue problem by applying Bloch's theorem between the nodes. The pseudo code for applying Bloch's theorem to corresponding DOF sets for 2D case can be found in Appendix A. This code can also be developed for the 3D case.

As a second method, Bloch's theorem can be applied between the corresponding nodes under the Structural Mechanics module in COMSOL Multiphysics program. In the program, Bloch BC can be found under the Solid Mechanics → Physics → Boundaries → Periodicity Settings → Floquet periodicity. Note that the wave vectors must be specified in the parameters section, following a route around the edge of the corresponding IBZ. Then the study can be performed with parametric sweep and eigenfrequency analyses. After completing the analyses, phonon band structure can be obtained under the Results → 1D

Plot Group → Dataset: Parametric Solutions → Global → y-Axis Data: Expression: solid.freq → x-Axis Data: Outer solutions and Parameter value → Plot.

As a third method, Bloch BC can be applied using a user-defined subroutine MPC in ABAQUS. This method does not need to import **K** and **M** matrices from other FE package programs and all analyzes are conducted by using ABAQUS. The difficulty in applying this method is that the complex valued relations of the Bloch BC specified in Equation (2.2) can be handled. Complex valued eigenvalue problem can be solved by dividing all fields into real and imaginary parts [85]. Thus, this method requires to duplicate mesh to take into account the real and imaginary parts.

Bloch BC can be applied as follows

$$\begin{aligned} Real(u_i^B) &= Real(u_i^A)\cos[\gamma.a_{A_iB_i}] - Imag(u_i^A)\sin[\gamma.a_{A_iB_i}] \\ Imag(u_i^B) &= Real(u_i^A)\sin[\gamma.a_{A_iB_i}] + Imag(u_i^A)\cos[\gamma.a_{A_iB_i}] \end{aligned} \quad (2.46)$$

where u_i^A, u_i^B are the displacements, $a_{A_iB_i} = x_i^B - x_i^A$ represents the distance between the two nodes A_i and B_i and γ is the wave vector. Equation (2.46) can be implemented using a user defined subroutine MPC in ABAQUS.

In this thesis, the first two methods (i.e., COMSOL Multiphysics, and ABAQUS/MATLAB) are used. The purpose of using the second method is to apply Bloch's theorem in COMSOL Multiphysics much faster and to compare the accuracy of band structure graphs obtained using two different programs. Note that COMSOL Multiphysics is very useful for simple geometries, but can be tricky to mesh complex geometries. The inertial amplification mechanism developed in the TUBITAK project (218M475) has a complex geometry and analysis time can be very long. In order to determine the most accurate model by comparing it to the FRF results of the 3×2 octahedron array, band structures are computed using both the COMSOL Multiphysics and ABAQUS/MATLAB programs.

2.4. Benchmark Solutions of the Wave Problems in Periodic Structures

In this section, wave problems in 1D, 2D, and 3D periodic structures previously studied in the literature [7,13,31] are investigated and the same results are obtained with the help of COMSOL Multiphysics and ABAQUS/MATLAB programs. In this way, it is shown that COMSOL Multiphysics and ABAQUS/MATLAB models which will be used for inertial amplification mechanisms are tested and verified.

2.4.1. Benchmark Solution of the Wave Problem in 1D Periodic Structure

A sample model in Ref. [31] is investigated to obtain and verify the phonon band structure in 1D, and the unit cell model is shown in Figure 2.20. In this study, local resonators are added to a main structure and band gaps are created by local resonance method. The structure has a shaft with torsional resonator that is periodically connected. Resonator has a soft rubber ring surrounded by an outer ring. The material of the shaft is epoxy ($\rho = 1180$ kg/m^3, $E = 1.59 \times 10^9$ Pa, $\upsilon = 0.37$) and the materials of the resonator are rubber ($\rho = 1300$ kg/m^3, $E = 3.4 \times 10^5$ Pa, $\upsilon = 0.47$) and lead ($\rho = 11600$ kg/m^3, $E = 1.49 \times 10^{10}$ Pa, $\upsilon = 0.37$). The radii are r_0 = 5 mm, r_1 = 8 mm, r_2 = 10 mm. The length of the ring is l = 25 mm and the lattice constant is a = 75 mm.

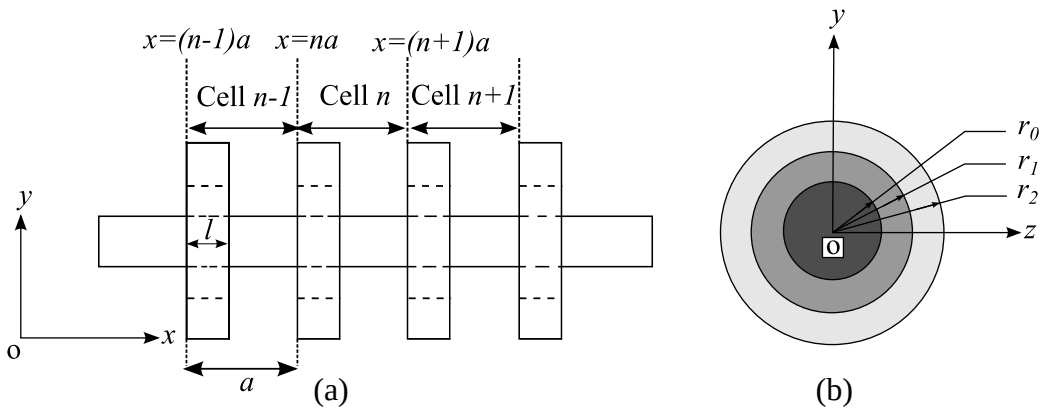


Figure 2.20. (a) Periodic structure, and (b) unit cell model of the sample model investigated in Ref. [31].

The band structure of the sample model is shown in Figure 2.21 [31]. In order to apply Bloch BCs between corresponding nodes or faces in 1D, the sample model shown in Figure 2.22 is created and analyzed in COMSOL Multiphysics.

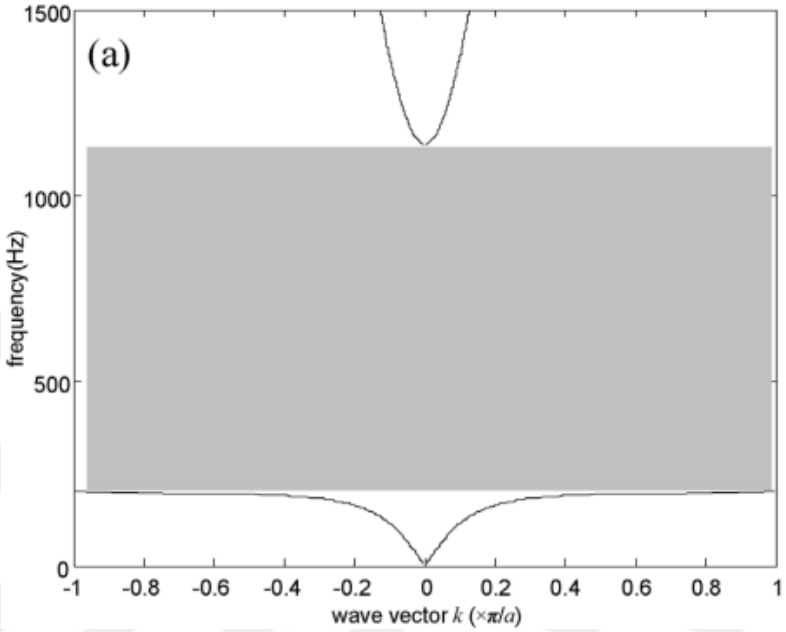


Figure 2.21. Phonon band structure showing 1D wave propagation of the model investigated in Ref. [31].

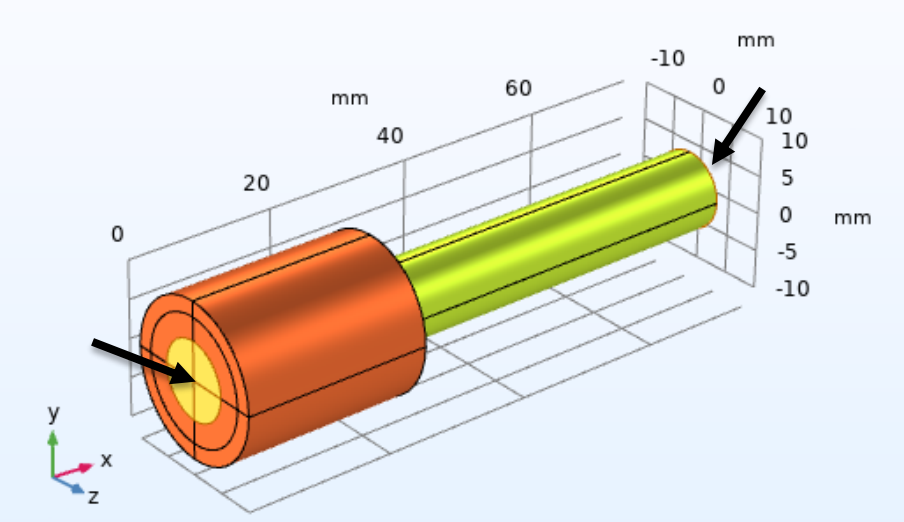


Figure 2.22. The corresponding faces in the *x* direction of the sample model created in COMSOL Multiphysics.

The band gap of the sample model is between 198 Hz and 1138 Hz in Ref. [31], while the band gap obtained by COMSOL Multiphysics is between 198 Hz and 1082 Hz. The band structure obtained by COMSOL Multiphysics is shown in Figure 2.23. There is 4.9% deviation at the upper limit of the band gap of the sample model investigated in Ref. [31]. This deviation is small and the COMSOL Multiphysics model is validated.

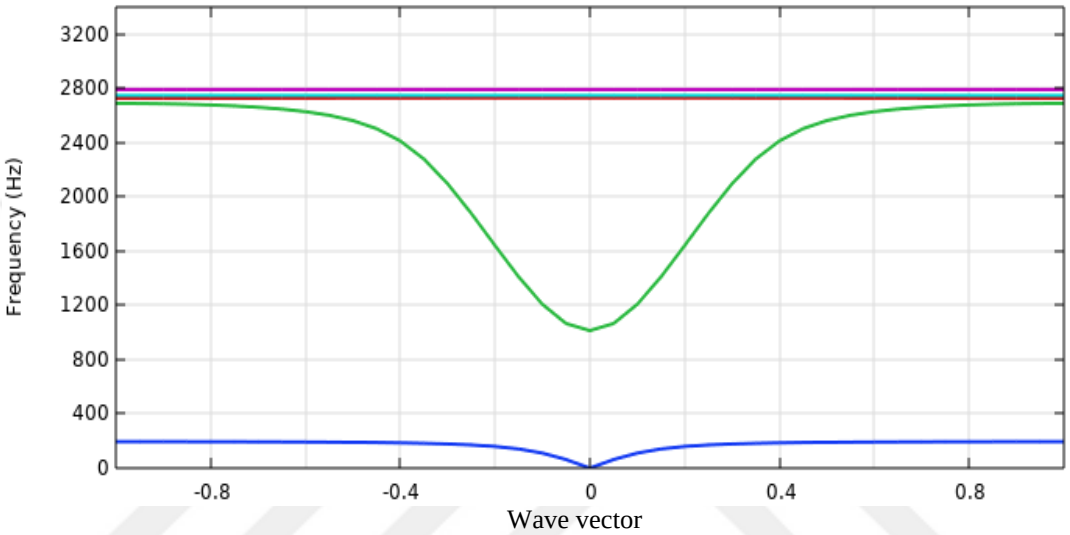


Figure 2.23. Phonon band structure showing the 1D wave propagation of the sample model investigated in Ref [31], obtained by using COMSOL Multiphysics.

2.4.2. Benchmark Solution of the Wave Problem in 2D Periodic Structure

A sample model in Ref. [7] is examined to obtain and verify the phonon band structure in 2D. The periodic structure of the unit cell is given in Figure 2.24a, and the geometries of the unit cell are given in Figure 2.24b and c. The region marked in blue in Figure 2.24a represents Figure 2.24b, and the region marked in red represents Figure 2.24c. The sample models shown in Figures 2.24b and c both represent the same periodic structure and give the same result when the two unit cells are used separately.

The material of the unit cell is copper ($\rho = 8900$ kg/m^3, $E = 120$ GPa, $\upsilon = 0.3$) and the dimensions are $b/a = 0.6$, $c/a = 0.3$, $d/a = 0.6$. The phonon band gap of the sample model is between 0.32 and 1.12 and the band structure is shown in Figure 2.25 [7].

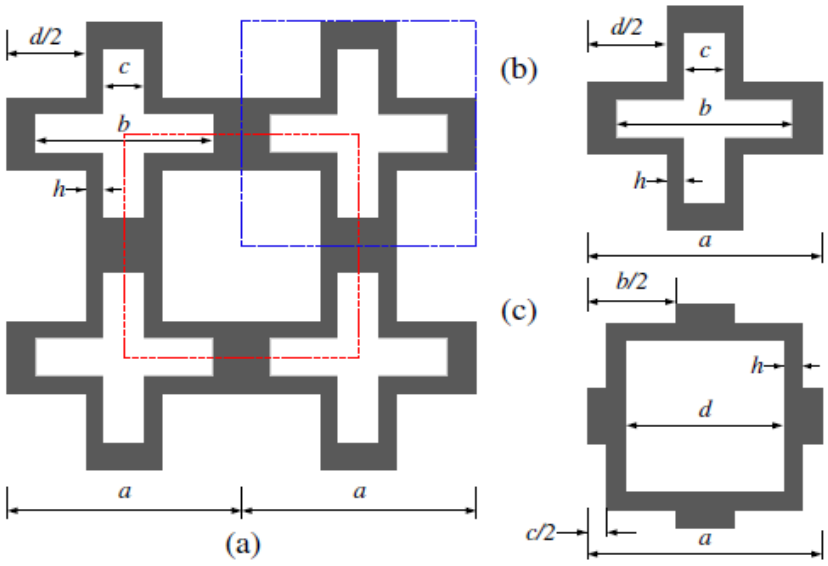


Figure 2.24. (a) Periodic structure, (b) and (c) unit cell of the sample model investigated in Ref. [7].

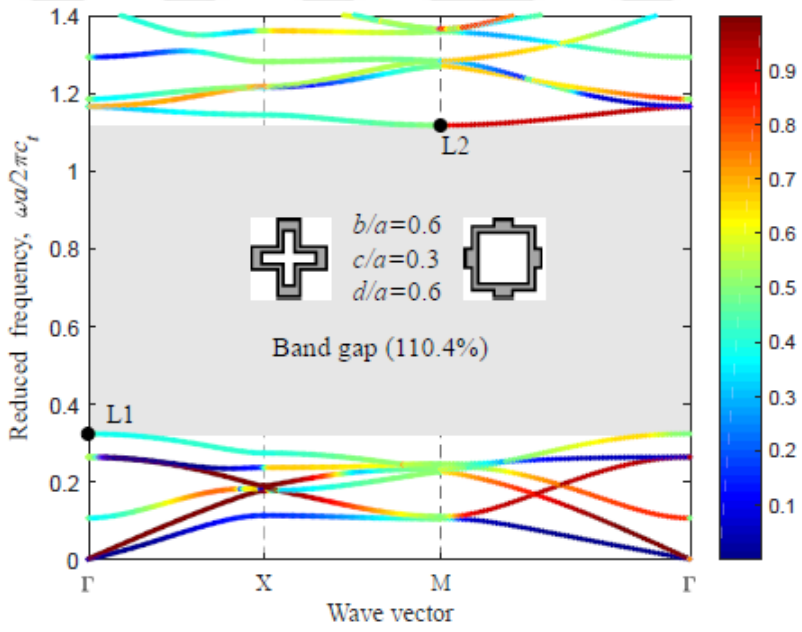
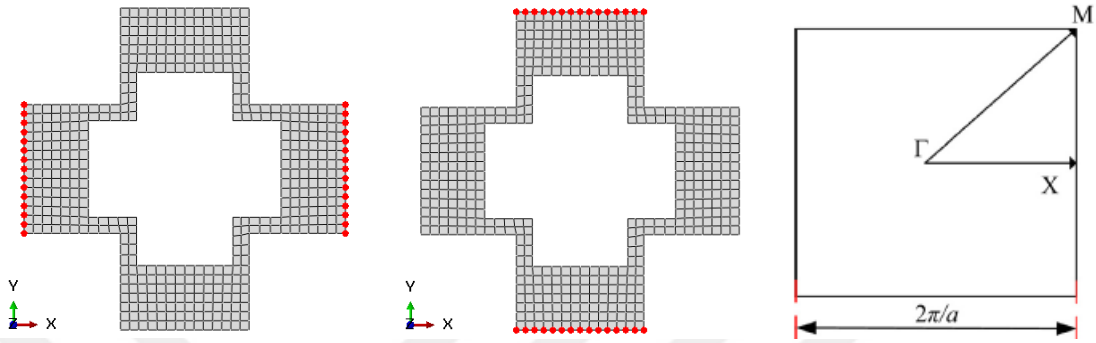


Figure 2.25. Phonon band structure showing the 2D wave propagation of the model investigated in Ref. [7].

The unit cell in Ref. [7] is designed, modeled and analyzed in ABAQUS, taking into account the same geometric and material properties. As a result of the modal analysis, **K** and **M** matrices are taken from ABAQUS and transferred to MATLAB. In order to obtain the phonon band structure for the 2D case, Bloch's theorem is applied between opposing nodes

as shown in Figure 2.26a and b, and the necessary MATLAB code is written for the 2D case. The pseudo code for applying Bloch's theorem to the corresponding DOF sets for 2D case can be found in Appendix A.



(a) (b) (c)

Figure 2.26. (a) The corresponding nodes in the *x* direction, (b) *y* direction of the sample model created in ABAQUS. (c) IBZ of the unit cell investigated in Ref. [7].

Figure 2.26a shows the relationship between opposing nodes in the *x* direction, and Figure 2.26b shows the relationship between opposing nodes in the *y* direction. In order to find the phonon band structure of the mechanism, the wave vector should follow a path around the IBZ. Since the periodic structure of the unit cell creates square symmetry and is periodic in the *x*-*y* directions, the IBZ of the system is as seen in Figure 2.26c [7].

The phonon band structure of the sample model obtained with the help of ABAQUS/MATLAB is shown in Figure 2.27. The phonon band structure of the sample model in Ref. [7] (see Figure 2.25) and the phonon band structure obtained in ABAQUS/MATLAB (see Figure 2.27) are similar. The band gap is between 0.32 and 1.12 in Ref. [7], whereas the band gap obtained by ABAQUS/MATLAB is between 0.32 and 1.09. It is not possible to obtain the exact mesh structure of the sample model in Ref. [7], and there is deviation of 2.7% at the upper limit of the band gap. This deviation is negligible and the developed MATLAB code is validated.

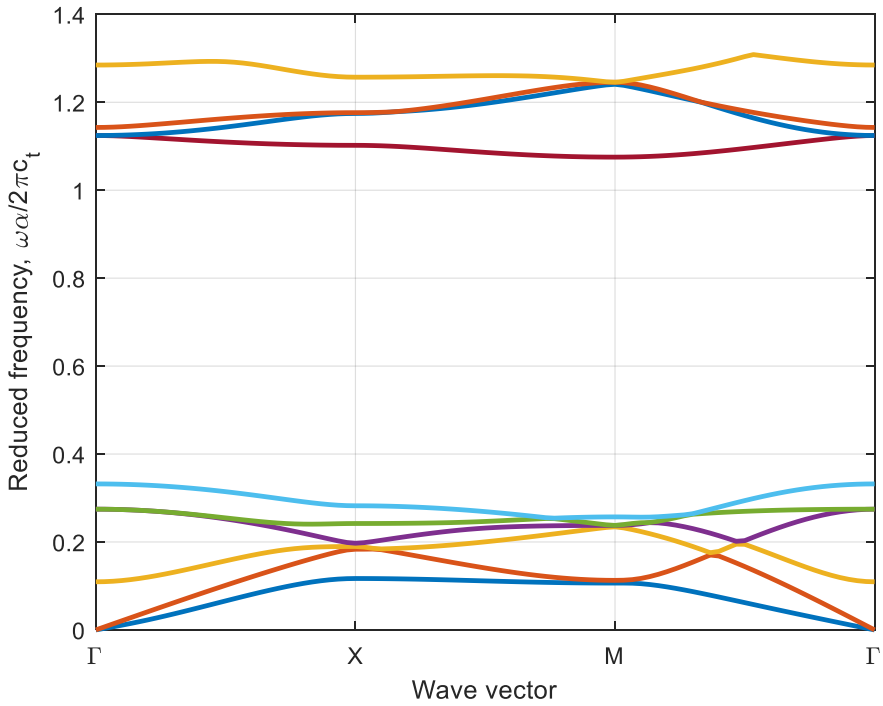


Figure 2.27. Phonon band structure showing the 2D wave propagation of the sample model investigated in Ref. [7], obtained by using ABAQUS/MATLAB.

As a second method, the same system in Ref. [7] is designed and modeled using COMSOL Multiphysics. The phonon band structure of the sample model obtained using COMSOL Multiphysics is shown in Figure 2.28.

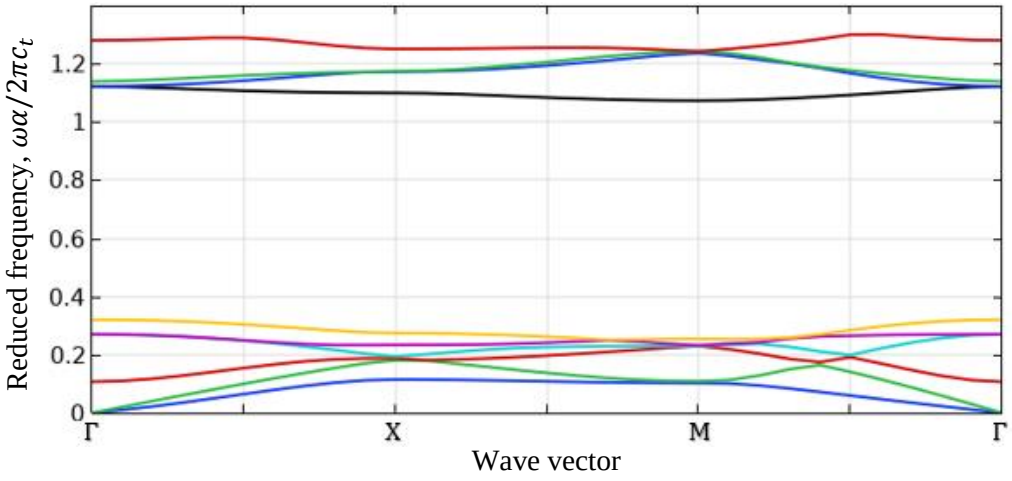


Figure 2.28. Phonon band structure showing the 2D wave propagation of the sample model investigated in Ref. [7], obtained by using COMSOL Multiphysics.

The band gap is between 0.32 and 1.12 in Ref. [7], while the band gap obtained by COMSOL Multiphysics is between 0.32 and 1.08. The upper limit of the band gap have 3.6% deviation. This deviation is small and the COMSOL Multiphysics model is validated.

2.4.3. Benchmark Solution of the Wave Problem in 3D Periodic Structure

A sample model in Ref. [13] is examined to obtain and verify the phonon band structure in 3D. The periodic structure of the unit cell is given in Figure 2.29a and the geometry of the unit cell is given in Figure 2.29b. As seen in Figure 2.29a, the periodic structure is obtained with the symmetry of the unit cell in the *x*, *y* and *z* directions.

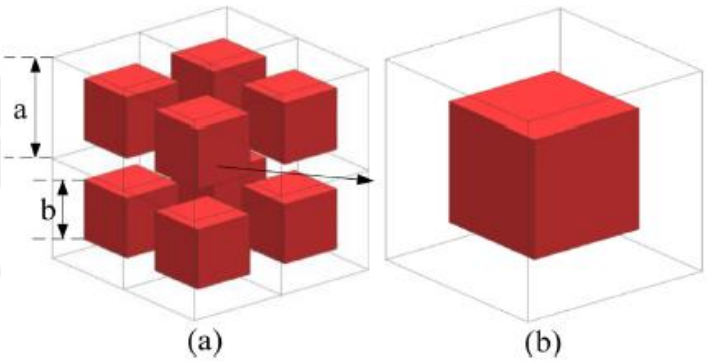


Figure 2.29. (a) Periodic structure, and (b) unit cell of the sample model in Ref. [13].

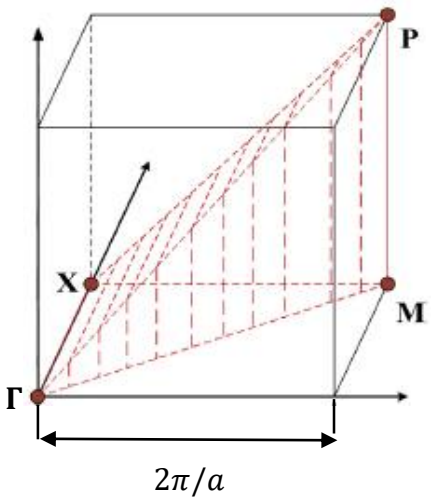


Figure 2.30. IBZ of the unit cell studied in Ref. [13].

There are two materials in the unit cell, the material of the small cube (red) is lead ($\rho = 11600$ kg/m^3, $\lambda = 4.23 \times 10^{10}$, $\mu = 1.49 \times 10^{10}$), and the material of the large cube (white) which surrounds the small cube is epoxy ($\rho = 1180$ kg/m^3, $\lambda = 4.43 \times 10^{9}$, $\mu = 1.59 \times 10^{9}$). Notice that $\lambda = Ev/(1+v)(1-2v)$ and $\mu = E/2(1+v)$ where E is Young's modulus and v is Poisson's ratio. In this model, the epoxy acts like a spring, while the lead acts like a mass because it is harder and heavier, and this model is a classic example of Bragg Scattering. The dimensions of the model are $b = 0.06$ m and a $= 0.10$ m. The IBZ geometry of the sample model is shown in Figure 2.30 and the phonon band structure is shown in Figure 2.31. The phonon band gap of the sample model is between 6900 Hz and 9100 Hz [13].

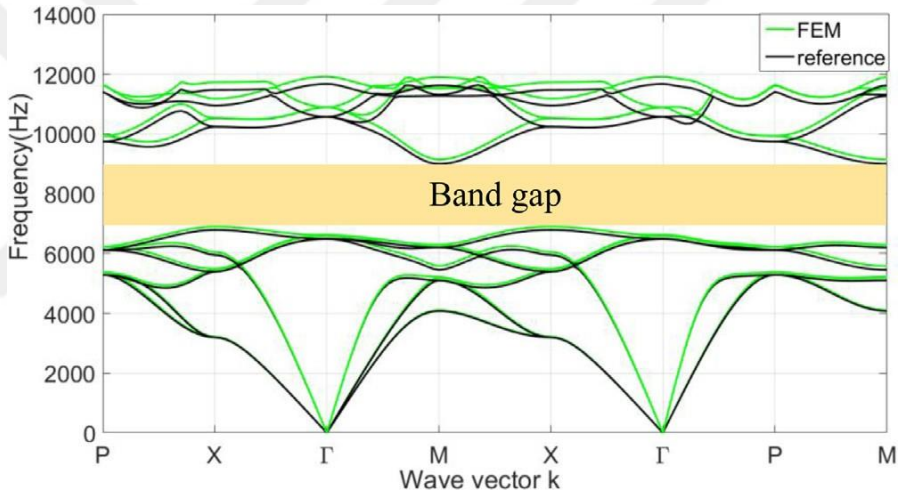


Figure 2.31. Phonon band structure showing the 3D wave propagation of the model studied in Ref. [13].

The unit cell in Ref. [13] is designed and modeled in ABAQUS using the same geometric and material properties, and the modal analysis results are obtained. As a result of the modal analysis, **K** and **M** matrices are taken from ABAQUS and transferred to MATLAB. The necessary MATLAB code is written for the 3D wave propagation case. The pseudo code for the 2D case given in Appendix A is developed for the 3D case and the phonon band structure is found by any numerical program. The phonon band structure of the sample model obtained with ABAQUS/MATLAB is shown in Figure 2.32. As seen in Figure 2.32, the phonon band structure of the sample model in Ref. [13] is similar to the phonon band structure obtained in ABAQUS/MATLAB. The band gap is between 6900 Hz and 9100

Hz in Ref. [13], whereas the band gap obtained by ABAQUS/MATLAB is between 6893 Hz and 9080 Hz. It is not possible to have the exact mesh structure of the sample model in Ref. [13], and there are deviations less than 1% at the upper and the lower limit of the band gap. These deviations are quite small and the developed MATLAB code is validated.

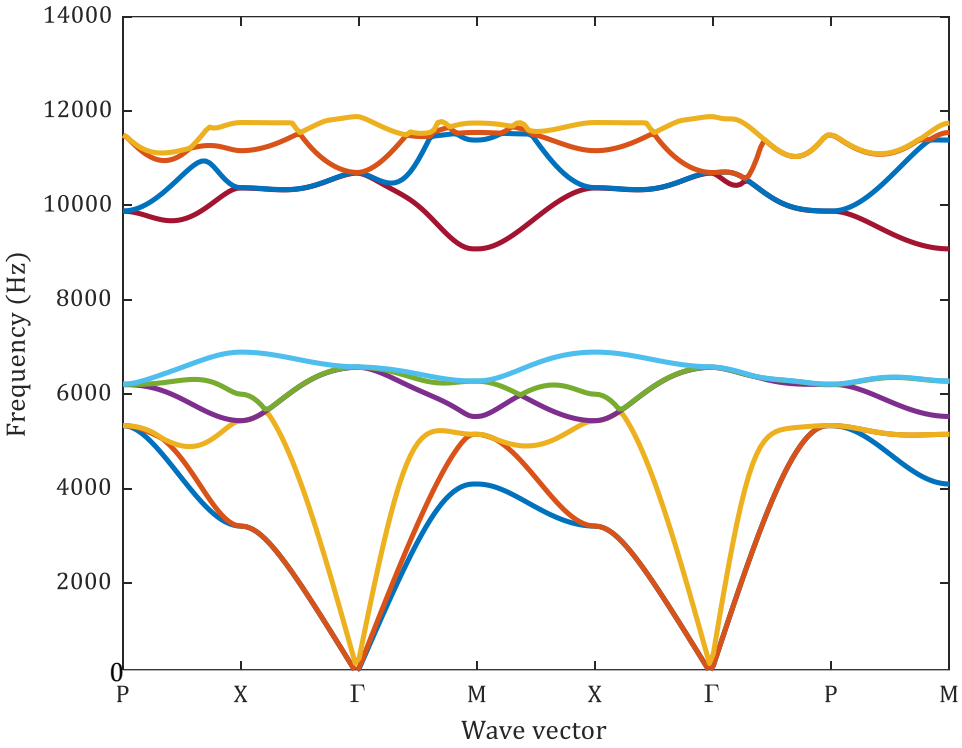


Figure 2.32. Phonon band structure showing the 3D wave propagation of the sample model investigated in Ref. [13], obtained by using ABAQUS/MATLAB.

As a second method, the same structure in Ref. [13] is designed and modeled using COMSOL Multiphysics. The phonon band structure of the sample model obtained using COMSOL Multiphysics is shown in Figure 2.33. The band gap is between 6900 Hz and 9100 Hz in Ref. [13], while the band gap obtained by COMSOL Multiphysics is between 6850 Hz and 9050 Hz. The deviations at the upper and lower limits of the band gap are less than 1%. These differences are negligible, and the COMSOL Multiphysics model is validated.

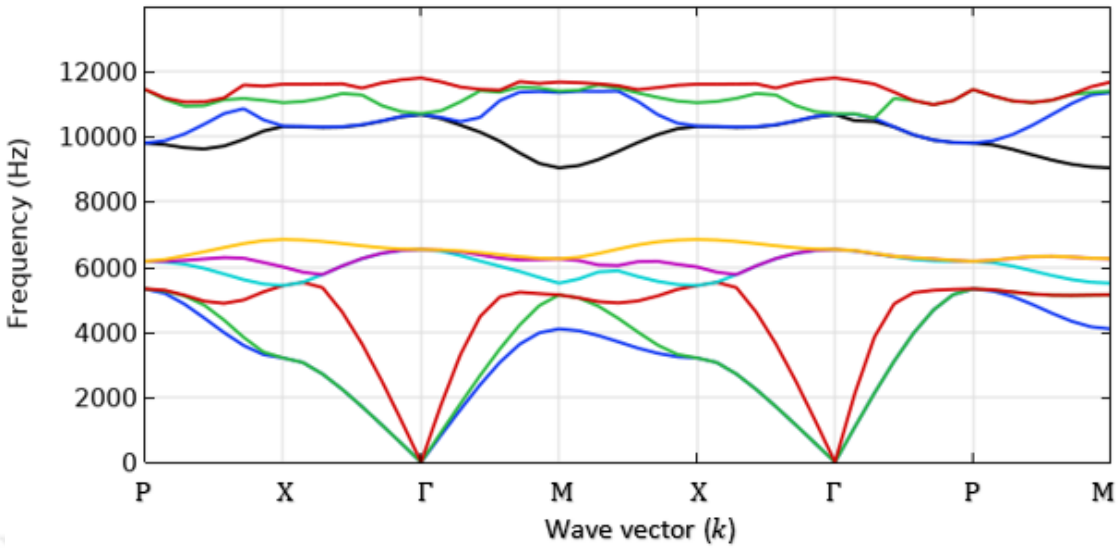


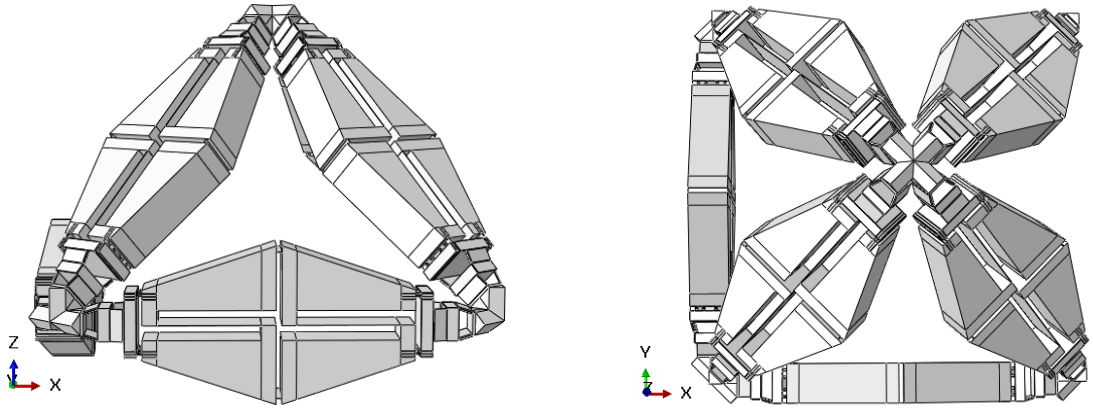
Figure 2.33. Phonon band structure showing the 3D wave propagation of the sample model investigated in Ref. [13], obtained by using COMSOL Multiphysics.

3. ANALYSIS OF THE 3D INERTIAL AMPLIFICATION MECHANISMS

In this chapter, 3D inertial amplification mechanisms with different sizes and geometries are analyzed and their band structures are obtained. In order to obtain the widest band gap in 3D, many iterations are performed with the help of COMSOL Multiphysics and ABAQUS/MATLAB programs. Four different cases are explained among many different iterations. Each of them has problems and these problems are solved with different techniques. The design and optimization of the mechanisms is beyond the scope of this thesis. Note that the inertial amplification mechanisms are designed and optimized by Sedef Nisan Otlu [86] and Berkay Acar [87], working on the same TUBITAK project (218M475).

3.1. FEM Model of the 3D Inertial Amplification Mechanism

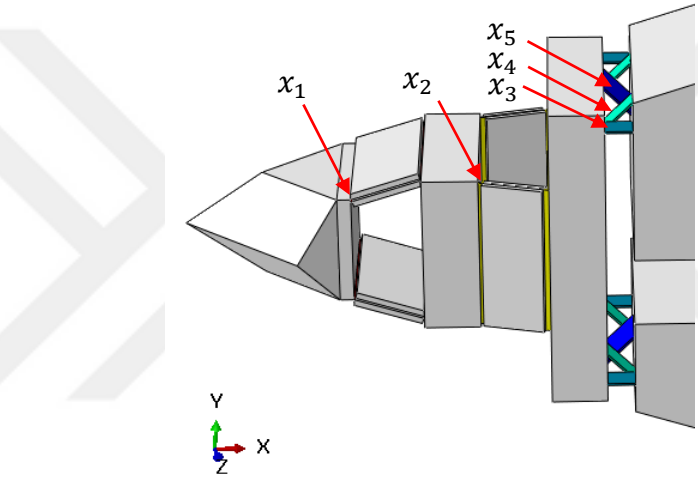
The unit cell model of the 3D inertial amplification mechanism is shown in Figure 3.1. As seen here, the unit cell model is obtained by combining six identical mechanisms shown in Figure 3.2.



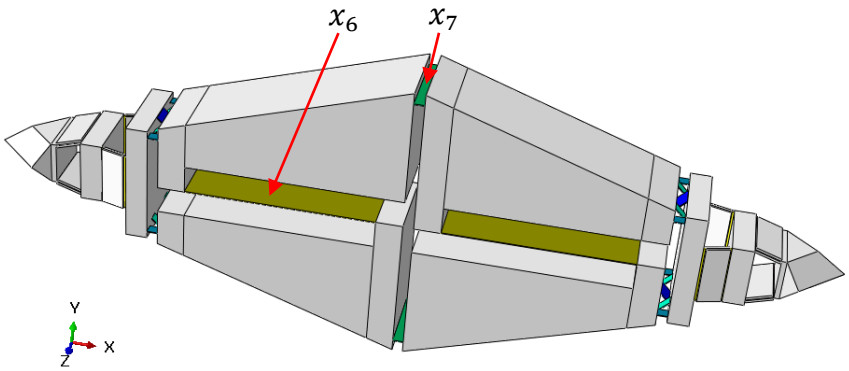
(a) (b)

Figure 3.1. (a) Front view and (b) top view of the designed inertial amplification mechanism unit cell model.

Each mechanism has seven thin flexures, all of which are the first (x_1) and second (x_2) remote center flexures, horizontal flexure (x_3), cross flexures (x_4, x_5) which make a 45 degree angle between horizontal axis, middle long (x_6) and short flexures (x_7). These flexures are quite important for the mechanism and their thicknesses are found by optimization to achieve the widest band gap in 3D. Detailed explanations of these flexures can be found in Ref [86]. The total length of the mechanism is 157 mm and the material of the mechanism is steel ($\rho = 7800$ kg/m^3, $E = 210$ GPa, $\upsilon = 0.3$). The thicknesses of all flexures shown in Figure 3.2 are initially determined as 0.15 mm [86].



(a)

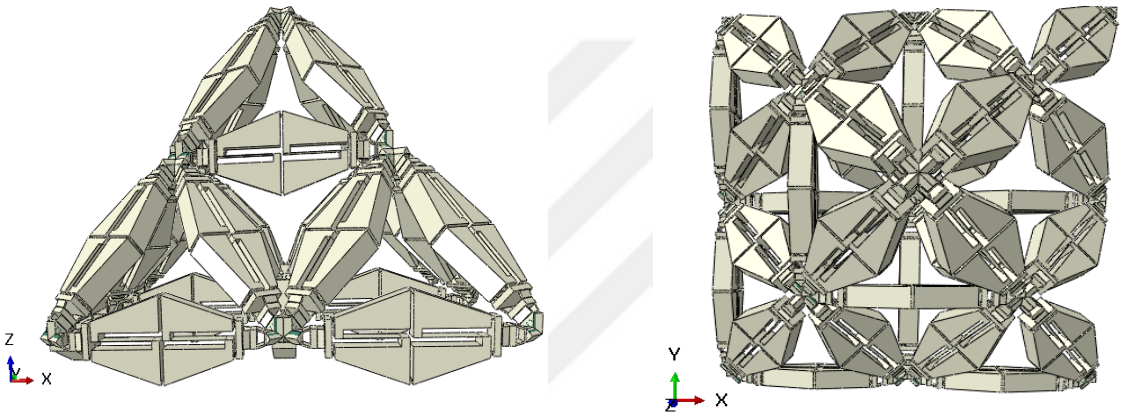


(b)

Figure 3.2. Seven thin flexures of the inertial amplification mechanisms. (a) First (x_1) and second (x_2) remote center flexures, horizontal flexure (x_3), and cross flexures (x_4, x_5). (b) Middle long (x_6) and short flexures (x_7) of the mechanism.

The periodic structure of the inertial amplification mechanism is shown in Figure 3.3a and b. As seen easily in Figure 3.3a and b, in order to obtain the periodic structure of

the mechanism, the mechanism is first translated in the *x-y* plane at the mechanism length and then offset by half the mechanism length in the *x* and *y* directions and by $\sqrt{2}/2$ of the mechanism length in the *z* direction. Assuming that an infinite periodic structure is obtained by continuing to repeat in these directions, the behavior of the infinite periodic structure can be analyzed by applying Bloch's theorem to the single unit cell. Bloch's theorem must be applied to the corresponding nodes of the unit cell model one by one to obtain Figure 3.3. In this way, the phonon band structure graph of the mechanism is obtained to understand the behavior of the infinite periodic case.



(a) (b)

Figure 3.3. (a) Front view and (b) top view of the periodic structure of the designed inertial amplification mechanism.

In order to obtain the band structure, another essential point is to obtain the IBZ geometry of the mechanism. The IBZ geometry used in the geometry investigated in Ref. [13] cannot be used, as the system does not have simple cube geometry. The IBZ geometry of the inertial amplification mechanism is in triclinic crystal structure and the IBZ geometry is as in Figure 3.4. While analyzing the system, waves with wave vectors tracing the path *B, Γ, F, Γ, G* are considered and the phonon band structure graph of the mechanism can be obtained.

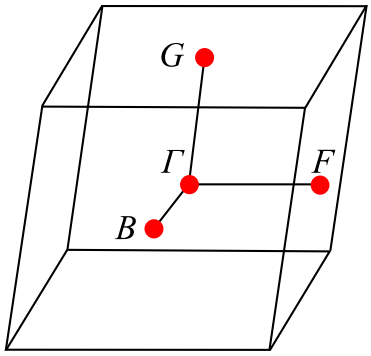


Figure 3.4. High symmetry points of the triclinic crystal structure and the IBZ of the inertial amplification mechanism.

The mesh used in the modal analysis of the inertial amplification mechanism is shown in Figure 3.5. In order to mesh the mechanism, the partition toolset in ABAQUS is used because it divides the geometries into simpler regions that ABAQUS can mesh by using different element types. It also provides more control over the meshing by improving the mesh quality. Hexahedral elements with the structured technique is used for the mechanism since the hexahedral elements have the highest accuracy of the solutions. The element type used is C3D8R, which is an eight-node linear brick with reduced integration.

The mechanism has very thin parts that can easily deform and relatively thick parts that almost do not deform. Hence, different size mesh is used in different regions considering the computational cost. Finer mesh is used for very thin deformable parts, and the coarser mesh is used for non-deformable parts. Unlike Euler Beam Theory, Timoshenko Beam Theory takes into account shear deformation and rotational bending effects. Thus, when meshing, the thin parts are also divided into several layers through the thickness to have high accuracy of the solution. Bloch's theorem is applied separately to the nodes on the yellow and red marked surfaces to obtain the infinite periodic structure of the mechanism. As can be seen in Figure 3.5, the regions marked with red and yellow must be symmetrical and the number of nodes must be equal in order to obtain the phonon band structure of the mechanism. Otherwise, Bloch's theorem cannot be applied and thus the band structure of the system whose node numbers do not match cannot be found. Therefore, matching of the node numbers and surfaces is the most important criterion when meshing the mechanism.

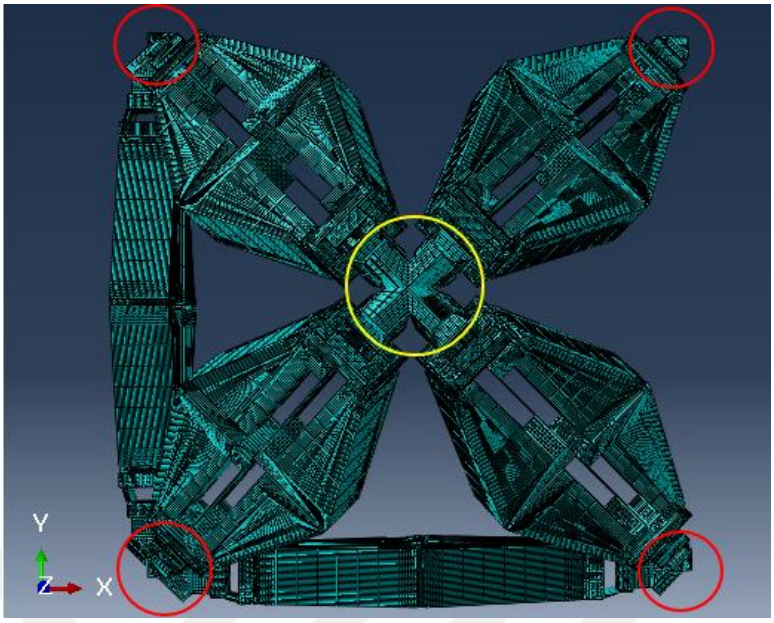
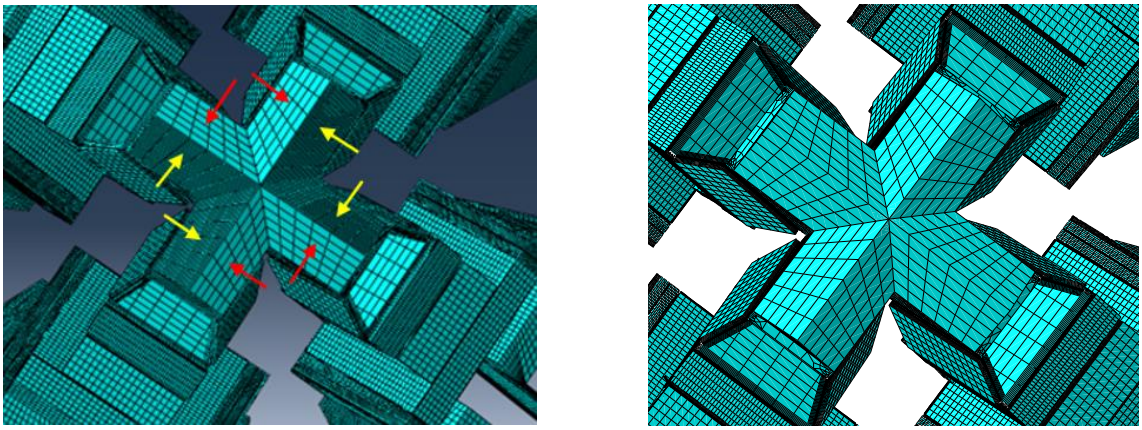


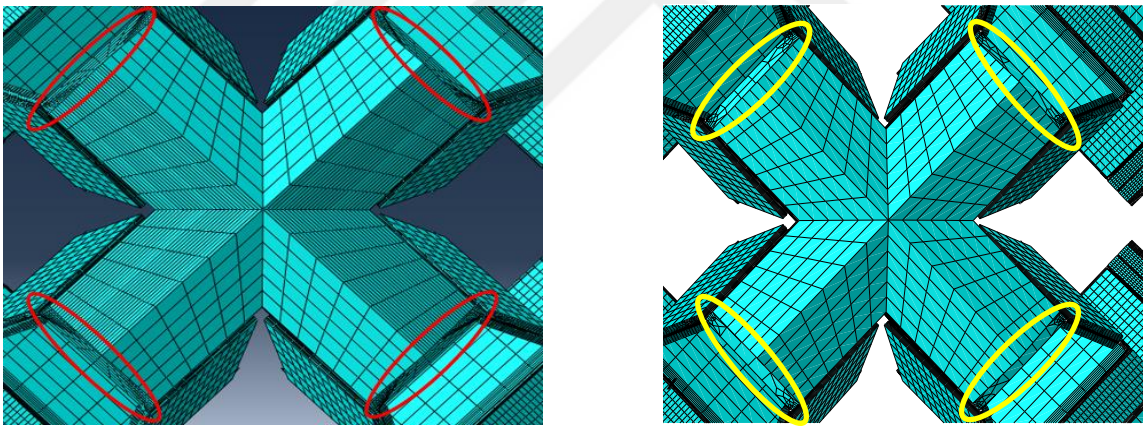
Figure 3.5. The mesh structure of the inertial amplification mechanism.

A detailed view of the surfaces marked in yellow in Figure 3.5 is shown in Figure 3.6a. As can be seen in Figure 3.6a, the number of nodes on the surfaces do not match, hence the band structure of the mechanism cannot be found. As six identical mechanisms are combined at a certain angle to create the inertial amplification mechanism, the corners of the mechanism marked in red and yellow in Figure 3.5 can only be meshed by partitioning the tetrahedron regions. Otherwise, it is not possible to partition the corners and mesh the mechanism. After using partitioning, different number of edges are automatically created at the corners of the mechanism, and symmetrical structures at the corners cannot be obtained by using hexahedral elements with the structured technique all over the geometry. Thus, the number of nodes on the surfaces do not match, and unsymmetrical surfaces are shown with red and yellow arrows in Figure 3.6a. As seen here, all surfaces indicated by the yellow and red arrows must be the same and the number of nodes on the surfaces must match as shown in Figure 3.6b.



(a) (b)

Figure 3.6. Detailed view of the surface marked with yellow circle in Figure 3.5. (a) Unsymmetrical matching surfaces of the 3D inertial amplification mechanism obtained using the structured mesh technique, and (b) symmetrical matching surfaces obtained using the sweep mesh technique.



(a) (b)

Figure 3.7. (a) Detailed view of the surface shown in Figure 3.6. (a) Red circles show hexahedral mesh structures obtained using the structured mesh technique, and (b) yellow circles show distorted mesh structures obtained using the sweep mesh technique.

In order to overcome the problem, either different mesh element types must be used for the mechanism or the number of edges at the corners must be made equal. Due to partitioning, too many edges are automatically created at the corners. Equalizing the number of each edge is a very complex task and takes a lot of time. Therefore, different mesh element types are used. More specifically, first hexahedral elements with the sweep mesh only on matching surfaces, and then hexahedral elements with the structured mesh for the rest of the

mechanism are used. Thanks to this approach, symmetrical mesh structures are first created on the matching surfaces regardless of the number of the edges at the corner. Thus, the distorted mesh structures marked with yellow circles in Figure 3.7b are created in the regions adjacent to the corners, which are the undeformed parts. The distorted mesh structures of these undeformed regions do not cause any difference in the analysis result. The proper hexahedral mesh structures marked with red circles obtained using the structured mesh technique and the distorted mesh structures marked with yellow circles adjacent to the corners obtained after using the sweep mesh technique are shown in Figure 3.7a and b, respectively. In the latter, each surface is the same and the node numbers of the surfaces match. As a result, matching problem is solved with this approach.

After solving the matching problem, the mechanism is analyzed in ABAQUS program. As a result of the modal analysis, **K** and **M** matrices are taken from ABAQUS and transferred to MATLAB. The size of the **K** and **M** matrices is very large, in particular, the size of the **K** matrix exceeds eight gigabytes (GB). The number of nodes in the mechanism is approximately 2 million 600 thousand.

The MATLAB code, previously validated for 3D wave propagation in Ref. [3], is run on a workstation with Intel Xeon Gold 5122 CPU @ 3.60 GHz (2 processors), 256 GB RAM and an out-of-memory warning is received. For this reason, the MATLAB code is optimized again. As a result of different iterations, results are obtained by using MATLAB in models with a maximum of 500 thousand nodes. At this stage, although the system includes detailed parts, the number of nodes is reduced to 500 thousand considering a certain margin of error in order to get results. In Table 3.1, the modal analysis results of the model with 2 million 600 thousand nodes and the model with 500 thousand nodes are compared, and the percentage deviations from the original model are given.

Before applying the periodic boundary condition (PBC), the unit cell is investigated under free-free BCs. In this case, the first six modes are values close to zero and are known as rigid body modes. When the unit cell is examined under free-free BCs, a large gap is generated between 15th mode and 16th mode. This frequency gap is similar to the band gap, and its exact limits can only be found when PBCs are applied. However, since the analysis takes too long when PBCs are applied, it is first investigated how the frequencies in the free-

free BCs of a single unit cell change according to the number of nodes in the model. As can be seen in Table 3.1, error rates are below 5% in the expected band gap. The ratio of the 16th mode to the 15th mode is 4.46 in the model with 2.600.000 nodes and 4.49 in the model with 500.000 nodes. The difference between the rates of the two models is less than 1% and is negligible.

Table 3.1. Natural frequencies of the model with the reduced number of nodes and the percentage deviations from the original model.

	Natural frequencies (Hz) of the original model (2.600.000 nodes)	Natural frequencies (Hz) of the model with the reduced number of nodes (500.000 nodes)	Frequency deviation rates (%) of the model with the reduced number of nodes (500.000 nodes)
7.mode	19.55	19.40	0.74
8.mode	20.44	20.30	0.64
9.mode	23.02	22.32	3.01
10.mode	23.43	22.73	2.95
11.mode	27.10	26.02	4.00
12.mode	29.94	28.65	4.30
13.mode	36.75	34.18	6.98
14.mode	39.09	37.38	4.35
15.mode	54.76	52.08	4.89
16.mode	244.48	234.06	4.26
17.mode	293.65	281.63	4.09
18.mode	310.6	297.19	4.31
19.mode	396.44	387.06	2.36
20.mode	402.35	388.85	3.35

As a result of the improvement in the number of nodes, the MATLAB code is run again and the analysis takes approximately 13 days. In order to reduce the run time, the MATLAB code is rewritten for parallel computing with MATLAB and the analysis time is reduced to 10 hours for the first six modes. The phonon band structure of the model obtained with ABAQUS/MATLAB is shown in Figure 3.8. The band gap is between 34 Hz and 341 Hz, and the ratio of the upper limit to the lower limit is 10.03. This ratio is much larger than the ratio of the 16th mode to the 15th mode (4.49) in the free-free boundary conditions.

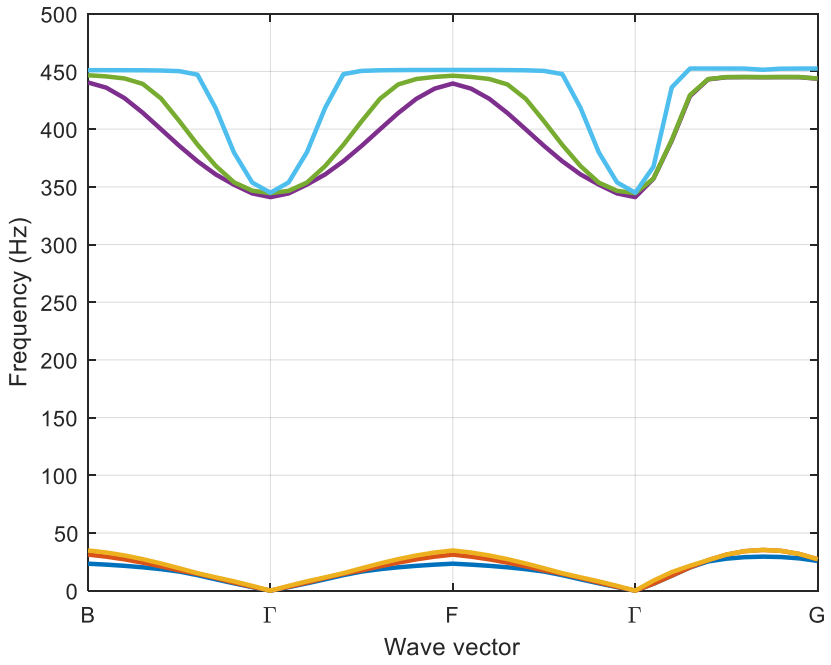


Figure 3.8. Phonon band structure showing the 3D wave propagation of the inertial amplification mechanism obtained using ABAQUS/MATLAB.

In addition, the same system is modeled in COMSOL Multiphysics and the modal analysis results are obtained. In COMSOL Multiphysics, phonon band structure is obtained directly in the program, without the need for an additional numerical program. While performing modal analysis, COMSOL Multiphysics also calculates the frequency values for each wave vector value with its parametric sweep feature. This, of course, causes the analysis to take longer and the program becomes unresponsive when the number of nodes is high. Therefore, as a result of the different iterations, models up to a maximum of 350 thousand nodes can be analyzed in COMSOL Multiphysics.

In Table 3.2, the modal analysis results of the COMSOL Multiphysics model with 350 thousand nodes and the modal analysis results of the ABAQUS model with 2 million 600 thousand nodes are compared, and the percentage deviations from the ABAQUS model (original model) are given.

Table 3.2. Natural frequencies of the models created using ABAQUS and COMSOL Multiphysics, and the percentage deviations from the ABAQUS (original) model.

	Natural frequencies (Hz) of the ABAQUS original model (2.600.000 nodes)	Natural frequencies (Hz) of the COMSOL Multiphysics model (350.000 nodes)	Frequency deviation rates (%) of the COMSOL Multiphysics model (350.000 nodes)
7.mode	19.55	19.11	2.26
8.mode	20.44	19.51	4.51
9.mode	23.02	23.34	1.38
10.mode	23.43	24.49	4.53
11.mode	27.10	28.66	5.76
12.mode	29.94	31.24	4.34
13.mode	36.75	39.85	8.44
14.mode	39.09	41.38	5.87
15.mode	54.76	58.48	6.79
16.mode	244.48	259.12	5.99
17.mode	293.65	310.92	5.88
18.mode	310.6	329.3	6.02
19.mode	396.44	406	2.41
20.mode	402.35	423.34	5.22

When the unit cell is examined under free-free BCs, a large gap is generated between 15th mode and 16th mode and the error rates for these modes are below 7%. The ratio of the 16th mode to the 15th mode is 4.46 in the ABAQUS model with 2.600.000 nodes and 4.43 in the COMSOL Multiphysics model with 350.000 nodes. The difference between the ratios obtained with these two models is less than 1% and is negligible. To sum up, three different modal analysis studies are performed in total. Two of them are carried out in ABAQUS with 2 million 600 thousand nodes and 500 thousand nodes and the other one is performed in COMSOL Multiphysics with 350 thousand nodes. As can be seen here, obtaining the phonon band structure is only possible with the ABAQUS/MATLAB model with 500 thousand nodes and the COMSOL Multiphysics model with 350 thousand nodes. Analysis of the COMSOL Multiphysics model takes 30 hours and phonon band structure of the model obtained with COMSOL Multiphysics is shown in Figure 3.9. The band gap of the model is between 40 Hz and 395 Hz, and the ratio of the upper limit to the lower limit is 9.88. This ratio is very close to the 10.03 ratio obtained with the ABAQUS/MATLAB model with 500 thousand nodes, and the difference between the ratios obtained with these two models is approximately 1.5%.

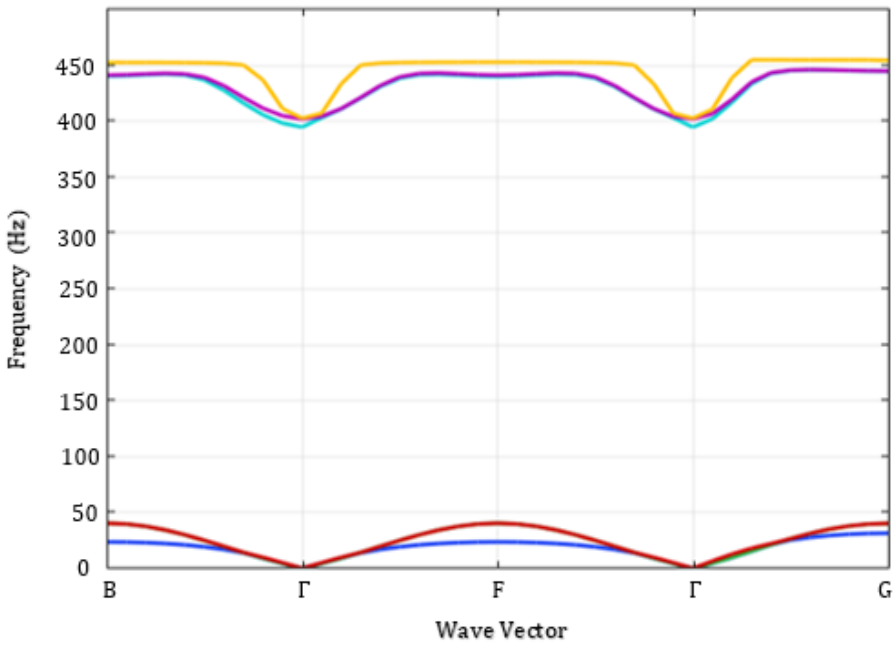


Figure 3.9. Phonon band structure showing the 3D wave propagation of the inertial amplification mechanism obtained using COMSOL Multiphysics.

In order to verify the models analyzed, the frequency responses of the inertial amplification mechanism, which is periodically arranged in the form of 3×2 is created using Hypermesh [87]. As seen in Figure 3.10, unit displacement is given from the left end point of the mechanism, the output is taken from the opposite point, and the result of frequency response function (FRF) analysis is given in Figure 3.11.

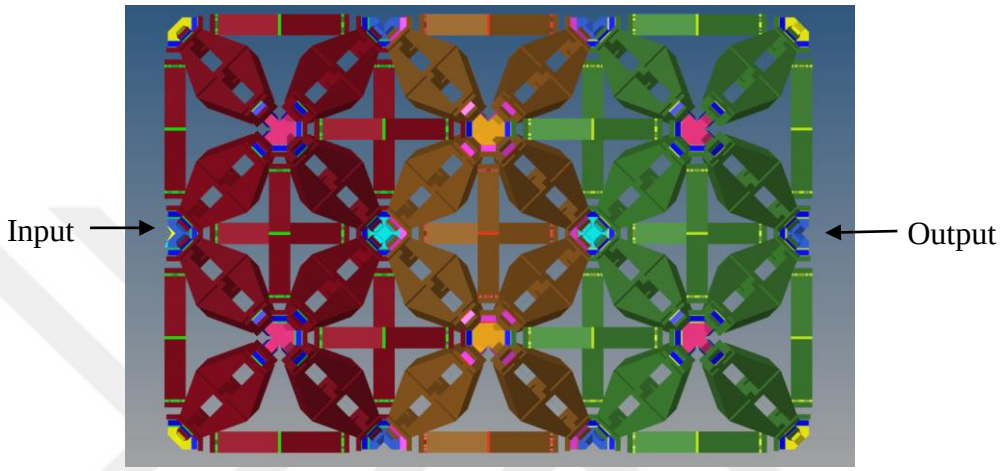


Figure 3.10. 3×2 octahedron array model of the inertial amplification mechanism [87].

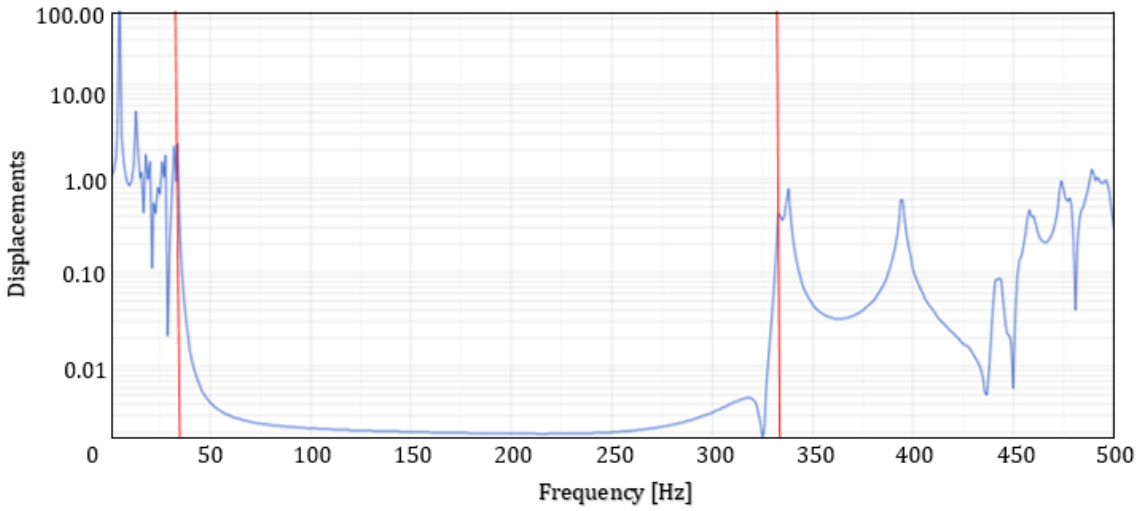


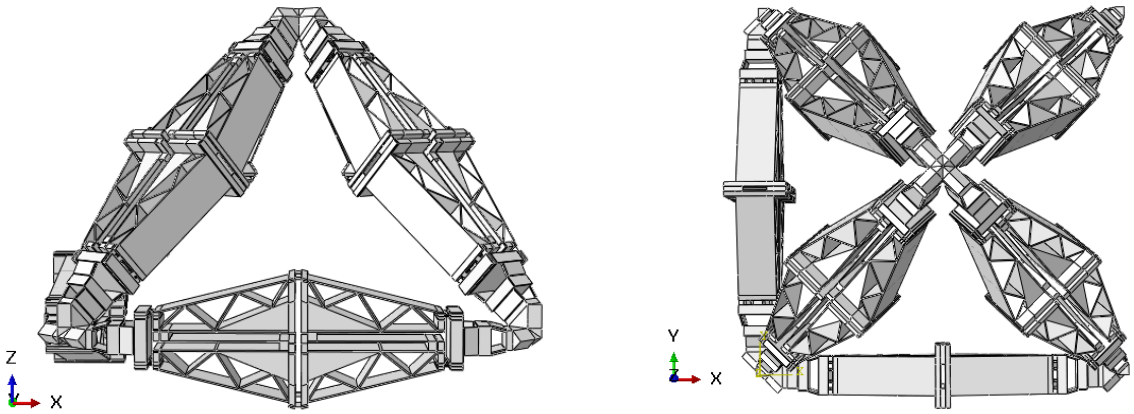
Figure 3.11. Frequency responses of the 3×2 octahedron array model of the inertial amplification mechanism [87].

The FRF analysis result of the 3×2 system shows that the band gap is between 33.63 Hz and 333.43 Hz and the ratio of the upper limit to the lower limit is 9.91 [87]. It is clear

that the ratio of the band gap limits of the model obtained using COMSOL Multiphysics, which is 395/40=9.88, and the ratio of the band gap limits of the 3×2 periodic system obtained in the FRF analysis, which is 333.43/33.63= 9.91, are close to each other. However, the upper and lower limits of the band gaps are quite different. The ratio of the band gap limits obtained with ABAQUS/MATLAB, which is 341/34= 10.03, and the ratio of the band gap limits of the 3×2 periodic system obtained in the FRF analysis, which is 333.43/33.63= 9.91, are similar. The difference between the ratios of the band gap limits of the two models is about 1.2%. The upper and lower limits of the band gaps are also similar. As a result of these comparisons, it is seen that the model obtained with ABAQUS/MATLAB gives more accurate results than the COMSOL Multiphysics model. One reason for the small differences in the phonon band gap obtained by using ABAQUS/MATLAB and the FRF analysis of the 3×2 periodic system is that the mesh types used for two models are different. The other important reason is that the phonon band gap found with Bloch's theorem in ABAQUS/MATLAB belongs to the infinite periodic structure, and the result of the FRF analysis is given only for the 3×2 periodic structure. If the number of unit cell is increased, the behavior of the finite periodic structure approaches the behavior of the infinite periodic system found with Bloch's theorem. In conclusion, the result is a high level of consistency and the differences are negligible.

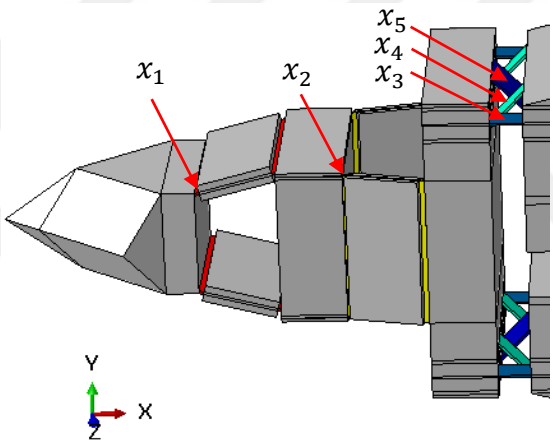
3.2. FEM Model of the First Optimized 3D Inertial Amplification Mechanism

The model of the first optimized 3D inertial amplification mechanism is shown in Figure 3.12. The unit cell model is obtained by combining six identical mechanisms shown in Figure 3.13. This mechanism is quite different than the mechanism shown in Figure 3.2. It has seven thin flexures ($x_1, x_2, x_3, x_4, x_5, x_6, x_7$), and three truss elements (x_8, x_9, x_{10}). Triangular blocks are supported with truss elements, rectangular blocks are added to the middle of the mechanism and the middle flexures are separated into two parts to widen the band gap of the mechanism. The total length of the mechanism is still 157 mm and the material of the mechanism is steel ($\rho = 7800$ kg/m^3, $E = 210$ GPa, $\upsilon = 0.3$). The thicknesses of flexures shown in Figure 3.13 are determined as $x_1 = x_2 = 0.16$ mm, $x_3 = 0.13$ mm, $x_4 = x_5 = 0.10$ mm, $x_6 = 0.15$ mm, $x_7 = 0.13$ mm, $x_8 = x_9 = x_{10} = 0.5$ mm [87].

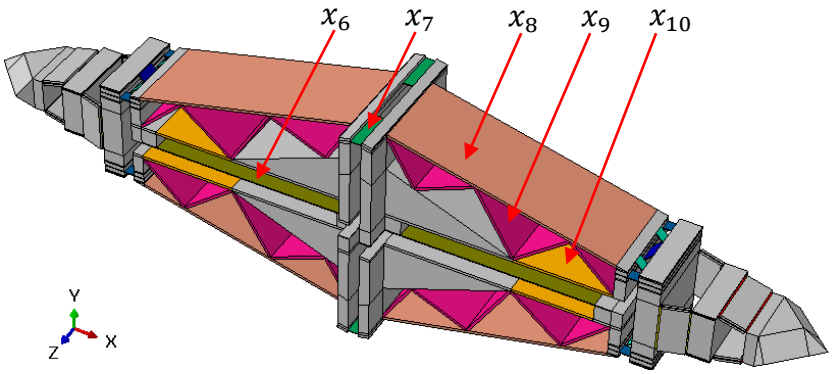


(a) (b)

Figure 3.12. (a) Front view and (b) top view of the first optimized unit cell model.



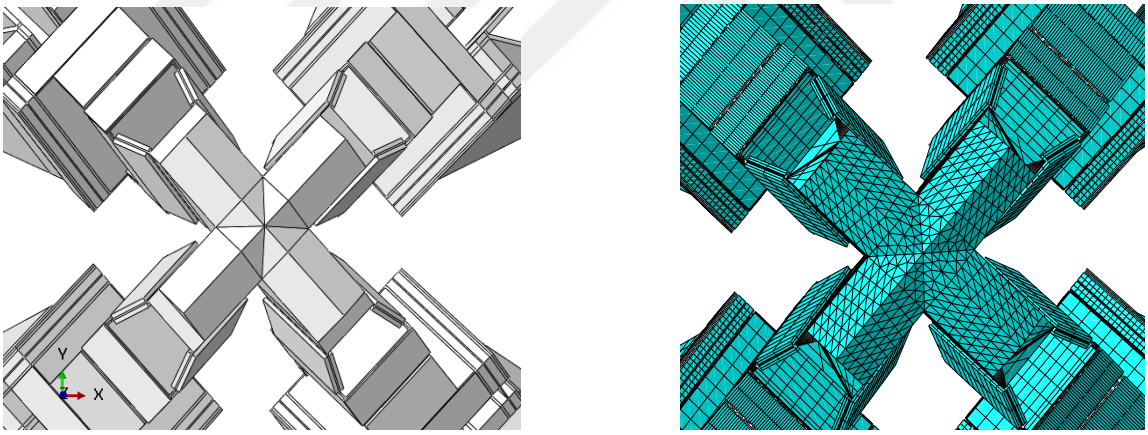
(a)



(b)

Figure 3.13. (a) First (x_1) and second (x_2) remote center flexures, horizontal (x_3), and cross flexures (x_4, x_5). (b) Middle long (x_6) and short flexures (x_7), and three truss elements (x_8, x_9, x_{10}) of the first optimized mechanism.

In order to obtain the phonon band structure of the first optimized mechanism, Bloch's theorem must be applied to the nodes on the yellow and red marked surfaces shown in Figure 3.5. As stated before, in order to apply Bloch's theorem, the number of nodes on the surfaces marked with red and yellow in Figure 3.5 must match. Since the first optimized geometry is different than the geometry shown in Figure 3.1, the corner geometries are partitioned in a different way. In this case, in order to match the corresponding surfaces and have the same number of nodes on the surfaces, first tetrahedral elements only on matching surfaces, and then hexahedral elements with the structured mesh for the rest of the mechanism are used. In the former case, the element type used is C3D4, which is a four-node linear tetrahedron, whereas the element type used in the latter case is C3D8R, which is an eight-node linear brick with reduced integration. In this way, the surfaces have the same number of nodes. The geometry of the top matching surfaces of the first optimized mechanism and the C3D4 type tetrahedral elements used are shown in Figure 3.14a and b, respectively.



(a) (b)

Figure 3.14. (a) The geometry of the top matching surfaces of the first optimized inertial amplification mechanism, and (b) its mesh structure obtained using the C3D4 tetrahedral element type.

After having the same number of nodes on the matching surfaces, Bloch's theorem can be applied in MATLAB. In order to obtain the phonon band structure using ABAQUS/MATLAB and not to receive an out-of-memory warning in MATLAB, the first optimized mechanism is modelled in ABAQUS with approximately 500 thousand nodes. If more nodes are used, the MATLAB program remains unresponsive and the phonon band

structure cannot be obtained. Therefore, the finer mesh is used for very critical parts that can deform, while the coarser mesh is used for non-deformable parts. The analysis time of the mechanism solved with the help of MATLAB parallel computation is 17 hours for the first 10 modes. The phonon band structure of the first optimized 3D inertial amplification mechanism is shown in Figure 3.15. As can be seen here, the phonon band gap of the first optimized mechanism is between 39.25 Hz and 512 Hz, and the ratio of the upper limit to the lower limit is 13.04.

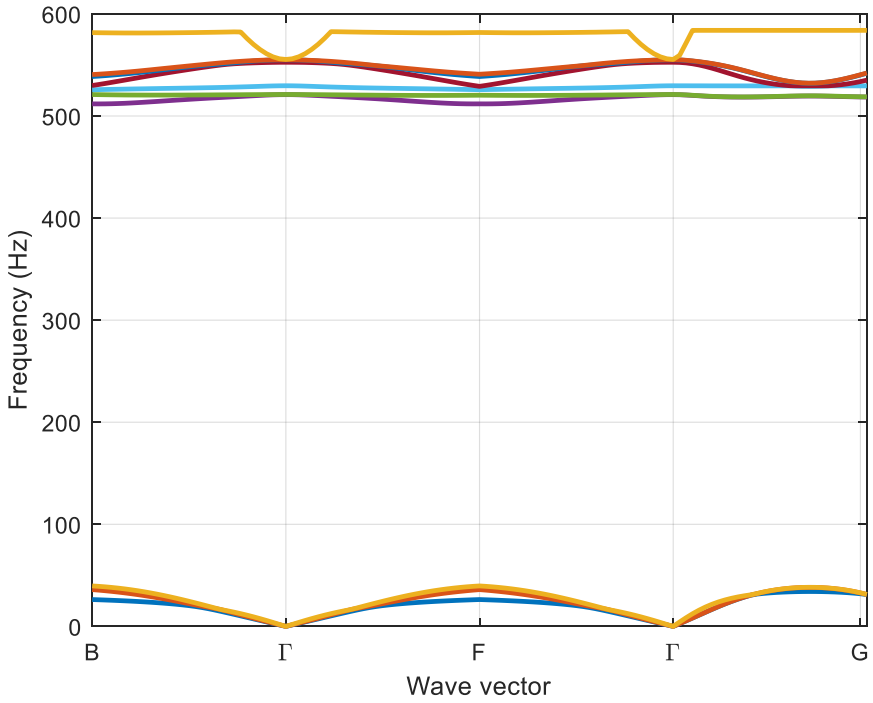
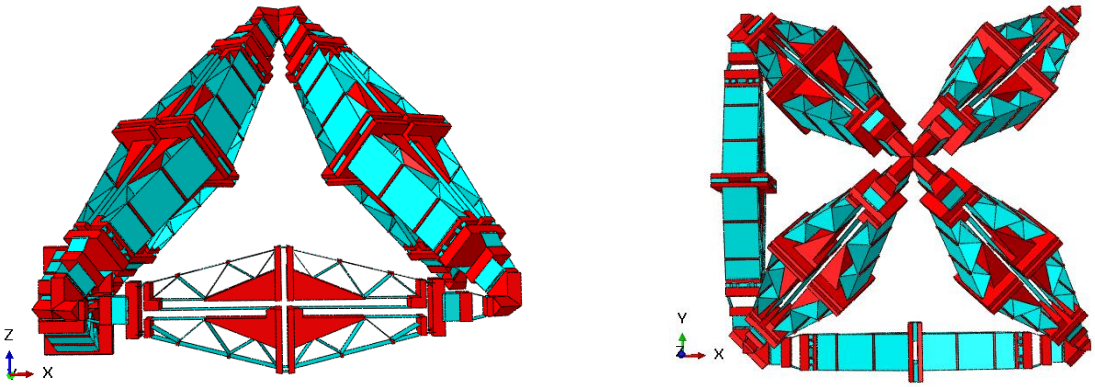


Figure 3.15. Phonon band structure showing the 3D wave propagation of the first optimized inertial amplification mechanism obtained using ABAQUS/MATLAB.

3.3. FEM Model of the Second Optimized 3D Inertial Amplification Mechanism

The model of the 3D inertial amplification mechanism obtained as a result of the second optimization is shown in Figure 3.16. The geometry is similar to the geometry shown in Figure 3.13, but the dimensions are different and shell elements in addition to solid elements are used in this geometry. The total length of the mechanism is still 157 mm and the material of the mechanism is steel.

The thicknesses of flexures are determined as $x_1 = x_2 = 0.148$ mm, $x_3 = 0.057$ mm, $x_4 = x_5 = 0.074$, $x_6 = 0.115$ mm, $x_7 = 0.079$ mm, $x_8 = x_9 = x_{10} = 0.516$ mm [87]. In Figure 3.16, the parts shown in cyan and red represent the shell and solid elements, respectively. In the second optimization, the dimensions of the mechanisms need to be changed many times until the optimum result is found, and therefore shell elements are used in addition to solid elements to model the inertial amplification mechanism. Otherwise, the mechanism must be modelled in each optimization study to find the optimum dimensions of the mechanism, resulting in a large amount of time wasted. Thus, the mechanism is modelled using solid and shell elements. Solid elements have three translational DOFs, whereas shell elements have three translational and three rotational DOFs at each node. The total number of DOFs of the model is much higher than the model using only solid elements. Because when only solid elements are used in any model, since each node has three DOFs, the total number of DOFs of the model is three times the number of nodes. Also, in the mechanism modeled in Hypermesh shown in Figure 3.16, shell elements enter a row into solid elements to prevent shell elements from rotating, and therefore some nodes are shared by both shell elements and solid elements.



(a) (b)

Figure 3.16. (a) Front view and (b) top view of the second optimized inertial amplification mechanism unit cell model.

Node numbers in ABAQUS or any other FEM program are generated automatically, and their numbering varies depending on the type of elements used. Conventional node ordering in FEM is shown in Figure 3.17. The node numbering is very confusing when considering the inertial amplification mechanism as it has solid, shell elements and shared

nodes. It is not known which nodes are solid, shell or shared and in what order they are in the **K** and **M** matrices obtained from ABAQUS. Therefore, **K** and **M** matrices obtained from ABAQUS are very complicated to read in MATLAB. Implementing Bloch's theorem by using **K** and **M** matrices in MATLAB also becomes very complicated and the MATLAB code previously written for the 3D case does not work in this case. In summary, two different problems need to be solved, reading **K** and **M** matrices by MATLAB and then implementing Bloch's theorem in MATLAB. In order to solve the problem of reading **K** and **M** matrices, two different methods can be used for the model that has solid, shell and shared elements.

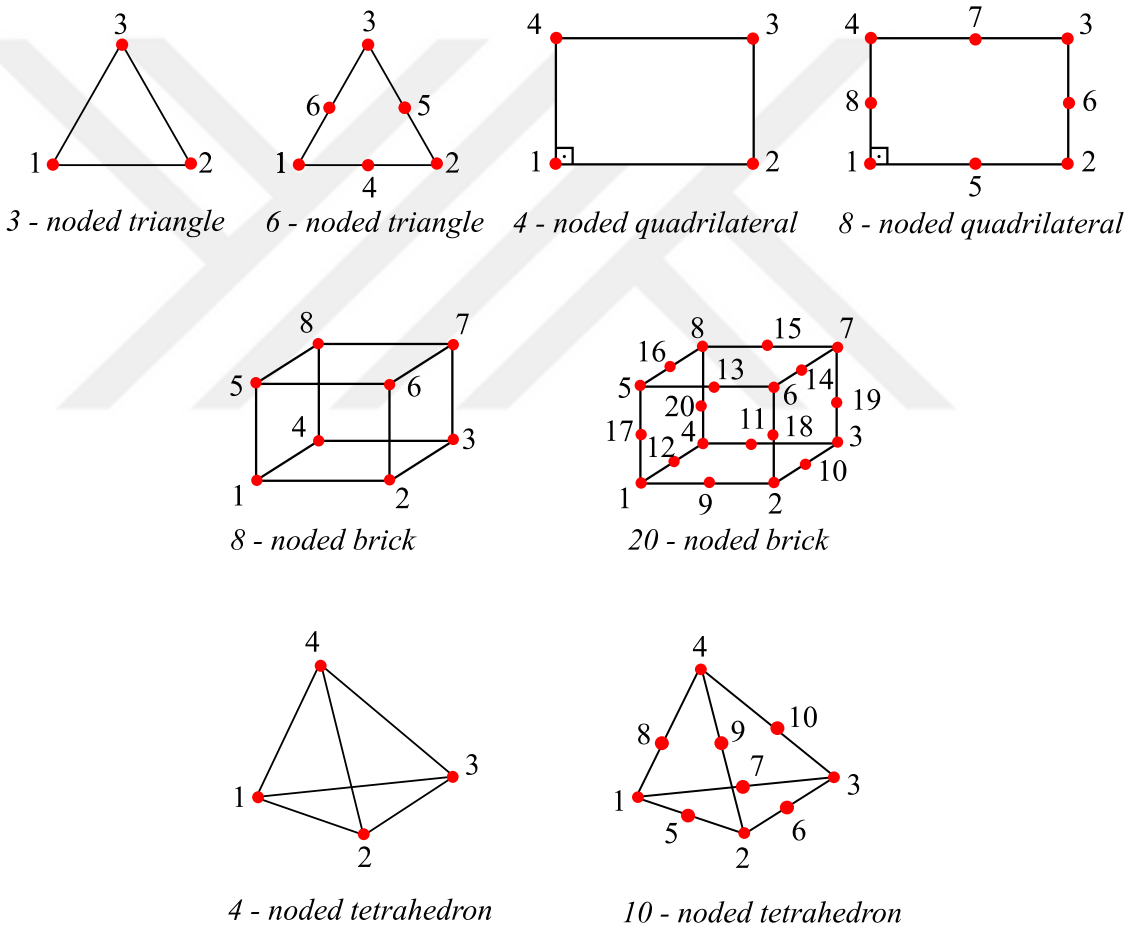


Figure 3.17. Node numbering of 2D and 3D elements in FEM.

The first method is to define the three different element sets, i.e., solid elements, shell elements and shared elements. **K** and **M** matrices for each element set are exported, then these matrices are merged to obtain the total matrix of the model. In order to do that, the code shown below should be written in the ABAQUS input file.

- *STEP, NAME=SOLID_ELEMENTS
- *MATRIX GENERATE, STIFFNESS, MASS, ELSET=<element set with only solid elements>
- *MATRIX OUTPUT, STIFFNESS, MASS, FORMAT=MATRIX INPUT
- *END STEP
- *STEP, NAME=SHELL_ELEMENTS
- *MATRIX GENERATE, STIFFNESS, MASS, ELSET=<element set with only shell elements>
- *MATRIX OUTPUT, STIFFNESS, MASS, FORMAT=MATRIX INPUT
- *END STEP
- *STEP, NAME=SHARED_ELEMENTS
- *MATRIX GENERATE, STIFFNESS, MASS, ELSET=<element set with both solid and shell elements>
- *MATRIX OUTPUT, STIFFNESS, MASS, FORMAT=MATRIX INPUT
- *END STEP

The alternative way is to generate **K** and **M** matrices by ABAQUS in the common mathematical coordinate format instead of the matrix input text format (default format). In order to get **K** and **M** matrices in the common mathematical coordinate format, the code shown below should be added in the ABAQUS input file.

- *STEP
- *MATRIX GENERATE, STIFFNESS, MASS
- *MATRIX OUTPUT, STIFFNESS, MASS, FORMAT=MATRIX COORDINATE
- *END STEP

Thanks to this, ABAQUS automatically generates the matrices that can be read by mathematics programs such as MATLAB. In this method, there is no need to define solid, shell and shared elements and merge them to get global matrices. This method is very useful and easier to implement. Both methods are validated and they both give the same result. For simplicity, the second method is used to overcome the problem of reading **K** and **M** matrices by MATLAB.

After solving the problem of reading the matrices with MATLAB, the problem of applying Bloch's theorem in MATLAB should be solved. In order to solve the problem, nodes are renumbered. First the nodes of the solid elements, then the shared nodes and finally the nodes of the shell elements are renumbered from one to the maximum number of nodes. The element with the least DOFs must be used first to ensure a certain order. This order is significant and only works when this starts with solid elements and ends with shell elements. The order is especially important on the matching surfaces where Bloch's theorem is applied. As seen in Figure 3.16, since only solid elements are used on the matching surfaces where Bloch's theorem is applied, the DOFs in these regions can be easily found for each node by multiplying three. After solving the problems, Bloch's theorem is applied in MATLAB.

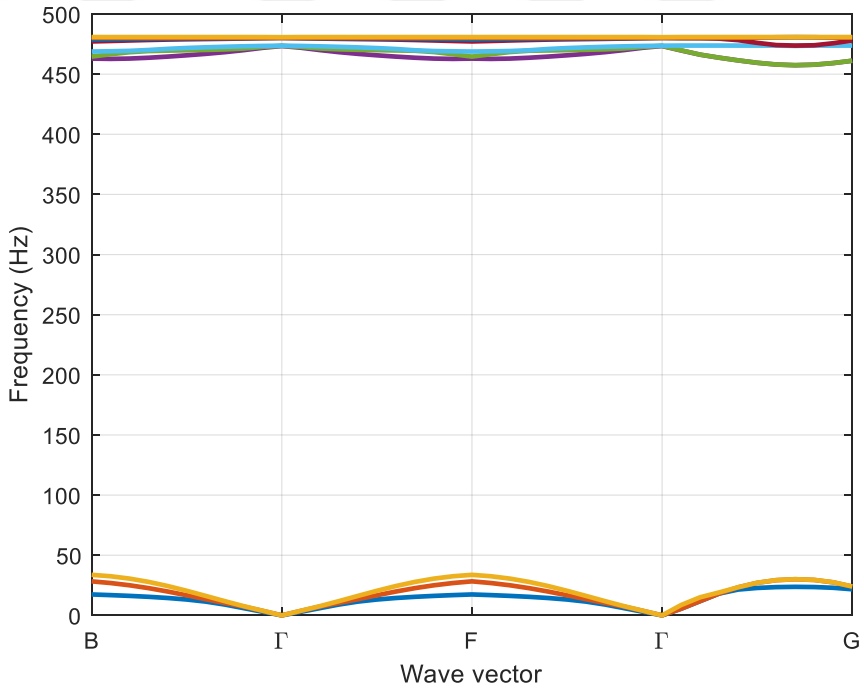


Figure 3.18. Phonon band structure showing the 3D wave propagation of the second optimized inertial amplification mechanism obtained using ABAQUS/MATLAB.

The phonon band structure of the second optimized 3D inertial amplification mechanism is shown in Figure 3.18. The analysis time of the mechanism solved with the help of MATLAB parallel computation is 15 hours for the first 10 modes. As can be seen in Figure 3.18, the phonon band gap of the second optimized inertial amplification mechanism is between 33.7 Hz and 457.5 Hz, and the ratio of the upper limit to the lower limit is 13.58.

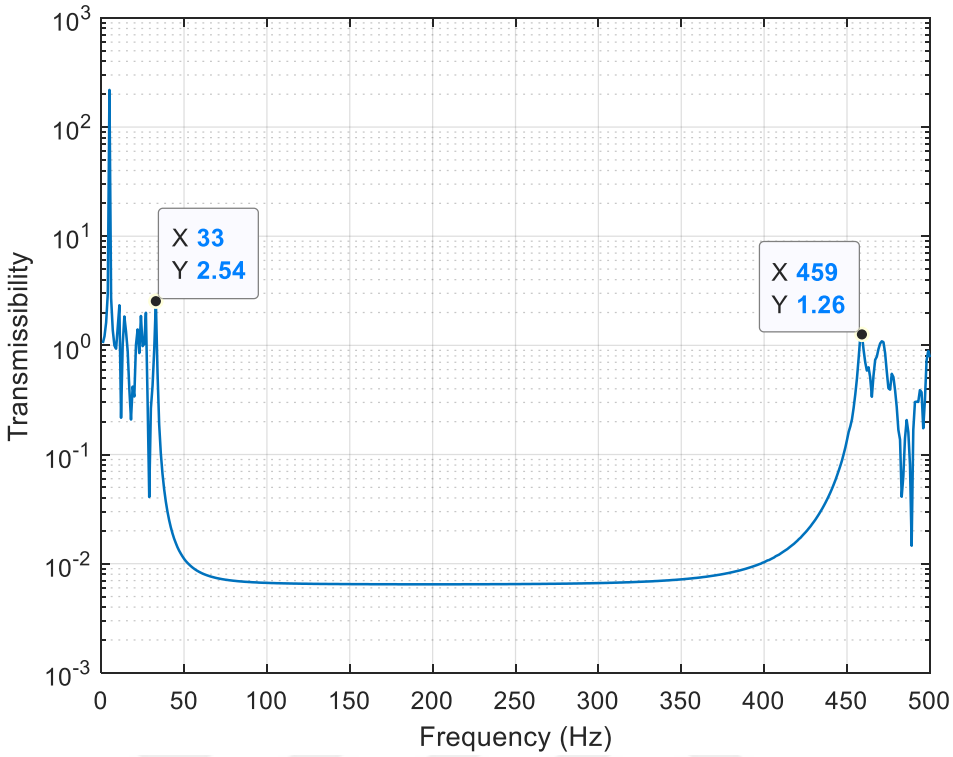


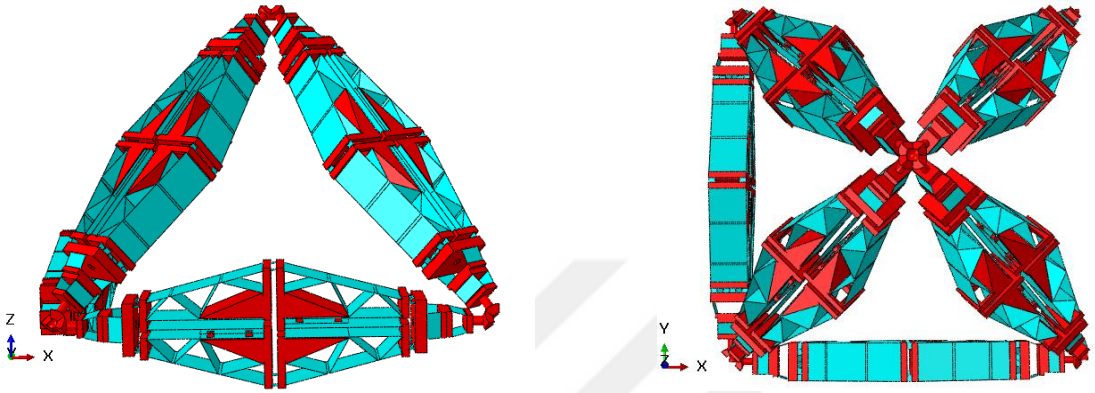
Figure 3.19. Frequency responses of the 3 × 2 octahedron array model of the second optimized inertial amplification mechanism.

The 3 × 2 octahedron array is arranged the same as the structure shown in Figure 3.10 for FRF analysis. Unit displacement is given from the left end point of the mechanism, the output is taken from the opposite point, and the FRF analysis result is given in Figure 3.19. As can be seen, the band gap is between 33 Hz and 459 Hz. The band gap limits of the 3 × 2 octahedron array and the infinitely periodic structure are thus demonstrated to be very similar.

3.4. FEM Model of the Optimized Large Scale 3D Inertial Amplification Mechanism

The band structure of the inertial amplification mechanism whose dimensions are scaled up after the first optimization study (see Section 3.2) is calculated. This mechanism is slightly different than the mechanism shown in Figures 3.12 and 3.13. It has also seven thin flexures ($x_1, x_2, x_3, x_4, x_5, x_6, x_7$), and three truss elements (x_8, x_9, x_{10}). The rectangular blocks next to the middle short flexures (x_7) are hollowed out, cross flexures (x_5) are

doubled, and M5 bolts are used at the end of the mechanism. In the first optimization study, the flexures are very thin and the minimum thickness is 0.1 mm. However, it is not likely to produce this mechanism with these thicknesses. Therefore, the length of the mechanism is increased by about 3.8 times to 600 mm in order to make the production feasible.

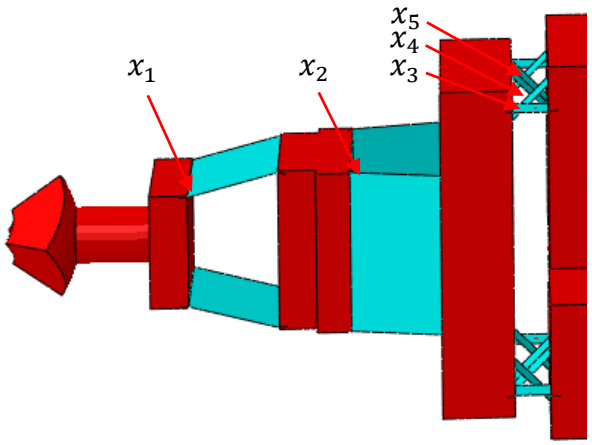


(a) (b)

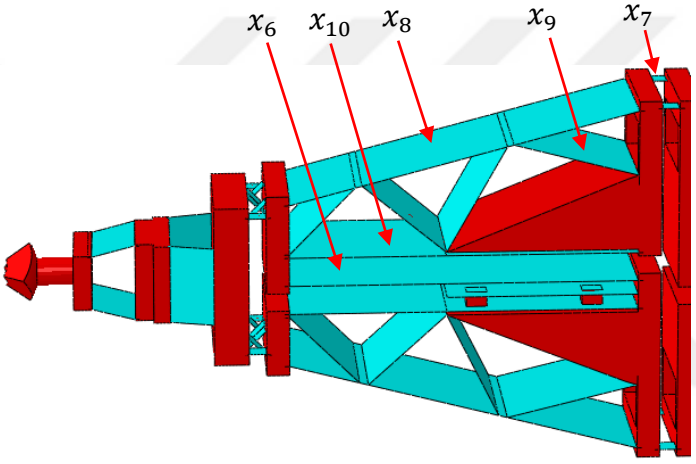
Figure 3.20. (a) Front view and (b) top view of the optimized large scale inertial amplification mechanism unit cell model.

The new thicknesses of flexures shown in Figure 3.21 are found as $x_1 = 0.44$ mm, $x_2 = 0.48$ mm, $x_3 = x_4 = x_5 = x_6 = x_7 = 0.4$ mm $x_8 = 2$ mm, $x_9 = 1$ mm, $x_{10} = 3$ mm [87]. As a result of scale up, it is aimed to decrease the natural frequencies of the system and to achieve isolation at low frequencies. It is aimed to provide vibration isolation in a wider frequency band by changing the limits of the first optimized parameters in the large scale mechanism.

The model of the 3D inertial amplification mechanism obtained as a result of the optimization is shown in Figure 3.20, and the parts shown in cyan and red represent the shell and solid elements, respectively. Notice that only half is shown in Figure 3.21b since the mechanism is symmetrical.



(a)

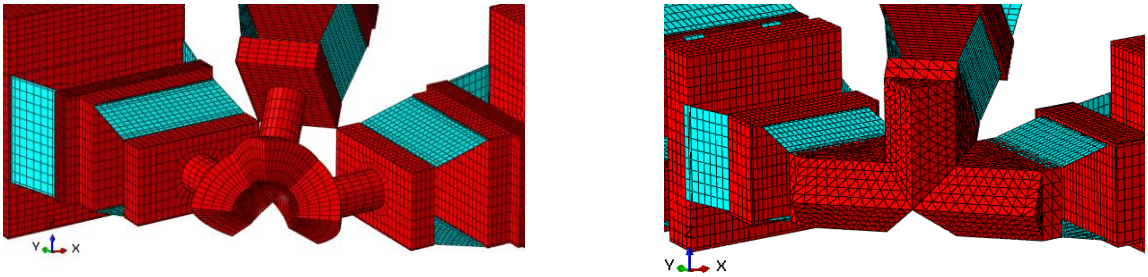


(b)

Figure 3.21. (a) First (x_1) and second (x_2) remote center flexures, horizontal flexure (x_3), and cross flexures (x_4, x_5). (b) Middle long (x_6) and short flexures (x_7), and three truss elements (x_8, x_9, x_{10}) of the large scale mechanism.

The corner geometries of the newly designed optimized large scale unit cell are different from the designed unit cell shown in Figure 3.12. Figure 3.22a shows the left corner geometry of the newly designed model, while Figure 3.22b shows the left corner geometry of the previously designed model shown in Figure 3.12.

In order to obtain the phonon band structure of the newly designed mechanism, Bloch's theorem must be applied to the corresponding nodes on the corner surfaces, which are the same as the locations shown in Figure 3.5.



(a) (b)

Figure 3.22. (a) Left corner geometry of the newly designed optimized large scale model, and (b) left corner geometry of the previously designed (see Figure 3.12) model of the inertial amplification mechanism.

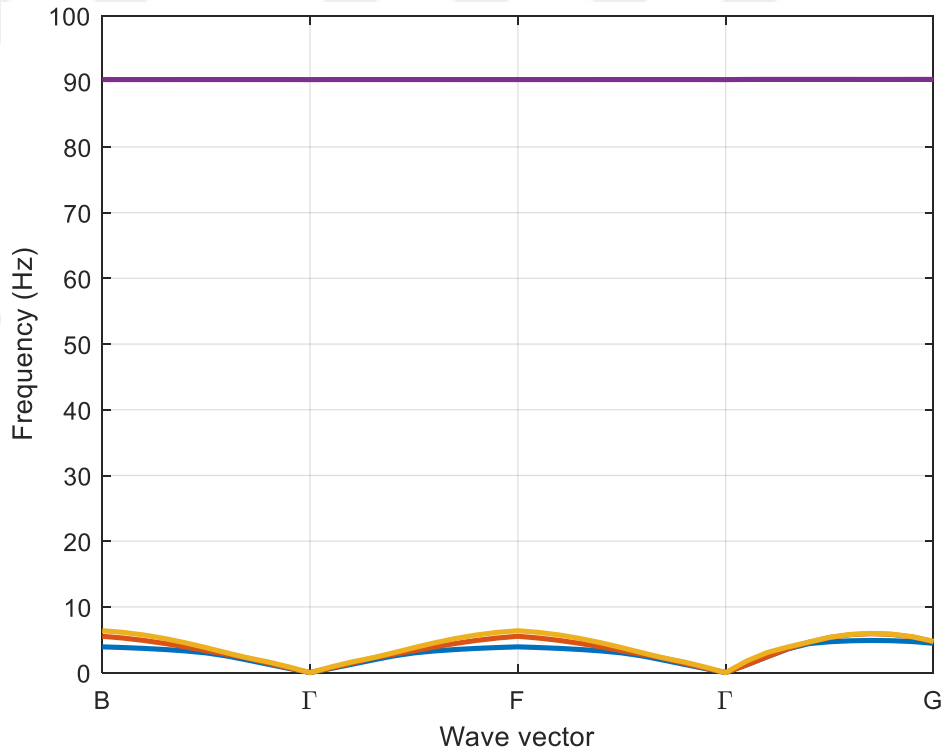


Figure 3.23. Phonon band structure showing the 3D wave propagation of the optimized large scale inertial amplification mechanism obtained using ABAQUS/MATLAB.

The phonon band structure of the optimized large scale 3D inertial amplification mechanism is shown in Figure 3.23. The analysis time of the mechanism solved with the help of MATLAB parallel computation is 10 hours for the first six modes.

As can be seen in Figure 3.23, the phonon band gap of the optimized large scale inertial amplification mechanism is between 6.37 Hz and 90.26 Hz, and the ratio of the upper limit to the lower limit is 14.17. This is the widest band gap obtained when all the 3D phononic crystals and elastic metamaterials in the literature are considered (see Table 1.1).

4. CONCLUSION

Three dimensional inertial amplification mechanisms with different sizes and geometries are analyzed to create the widest band gap in the literature. The band structures of the mechanisms are obtained by applying periodic boundary conditions, also called Bloch's boundary conditions, to the unit cells. In the literature, the widest band gap in 3D is achieved by this method, and the band gap is found to be in between 6.37 - 90.26 Hz, with a ratio of the upper limit to the lower limit of 14.17. Hence, vibration transmission is prevented in all directions within this frequency range.

First of all, typical wave problems in 1D, 2D, and 3D periodic structures studied in the literature are investigated and benchmark studies are performed with the help of COMSOL Multiphysics and ABAQUS/MATLAB programs. Thanks to the testing and validation of these models, the phonon band structure of the 3D elastic metamaterials with embedded inertial amplification mechanisms can then be precisely calculated. The inertial amplification mechanism developed in the TUBITAK project (218M475) has a complex geometry and analysis time can be very long. Therefore, phonon band structures are calculated by using both COMSOL Multiphysics and ABAQUS/MATLAB programs to obtain the most accurate model by comparing with the FRF results of the 3×2 octahedron array.

Many problems are encountered while applying Bloch's theorem to the inertial amplification mechanisms. First, matching problems occur on surfaces of different inertial amplification mechanisms where Bloch's theorem is applied. They are solved by using different mesh techniques in ABAQUS. Second, since inertial amplification mechanisms have very thin and thick parts, they can only be modelled with approximately 2 million 600 thousand nodes in ABAQUS. Thus, the size of the **K** and **M** matrices becomes very large, and only the **K** matrix exceeds eight gigabytes (GB). Even when using a workstation computer with a 16-core Intel Xeon Gold 5122 CPU 3.60 GHz and 256 GB RAM to calculate the phonon band structure, MATLAB gives an out of memory warning. To solve the problem, the MATLAB code is optimized and as a result of different iterations, results can only be obtained by using MATLAB in models with a maximum of 500 thousand nodes

modelled with ABAQUS. As a second method, COMSOL Multiphysics is used to calculate the band structure of the same geometries. Models up to a maximum of 350 thousand nodes can be analyzed in COMSOL Multiphysics. To sum up, only the ABAQUS models with 500 thousand nodes and the COMSOL Multiphysics models with 350 thousand nodes can be used to calculate the phonon band structures of the 3D elastic metamaterial with embedded inertial amplification mechanisms. A certain margin of error is, of course, taken into account to get results. Otherwise, it is not possible to get any results. The error rates between both models and the ABAQUS model with 2 million 600 thousand nodes (original model) are less than 1% and are negligible. When the results obtained with COMSOL Multiphysics and ABAQUS/MATLAB are compared with 3×2 FRF results, ABAQUS/MATLAB gives more accurate results than COMSOL Multiphysics model. Therefore, ABAQUS/MATLAB is used for subsequent calculations. Third, the computational costs of the models are very high. The analysis takes about 13 days for the ABAQUS model with 500 thousand nodes solved with the help of MATLAB. Therefore, MATLAB code is optimized, and parallel computation is used. Thus, the analysis time of the same system is reduced to 10 hours. Finally, when mechanisms are modeled using only solid elements, the number of nodes becomes too large and phonon band structures cannot be computed due to memory shortage or a certain margin of error is taken. Also, in optimization study, the dimensions of the mechanisms need to be changed many times until the optimum result is found. Thus, the models containing both solid and shell elements are used. The use of models containing solid and shell elements, however, brings about some problems because the elements have different degrees of freedom. The problems are reading the **K** and **M** matrices by MATLAB and then implementing Bloch's theorem in MATLAB. The easiest way to solve the former problem is to use the common mathematical coordinate format instead of the matrix input text format (default format) in ABAQUS. To solve the latter problem, on the other hand, nodes are renumbered. To conclude, the above mentioned problems are solved, and thus the widest band gap in 3D is calculated.

REFERENCES

1. Kushwaha, M. S., P. Halevi, L. Dobrzynski and B. Djafari-Rouhani, “Acoustic Band Structure of Periodic Elastic Composites”, *Physical Review Letters,* Vol. 71, No. 13, pp. 2022-2025, 1993.

2. Kushwaha, M. S., “Classical Band Structure of Periodic Elastic Composites”, *International Journal of Modern Physics B,* Vol. 10, No. 09, pp. 977-1094, 1996.

3. Yu, D., Y. Liu, G. Wang, H. Zhao and J. Qiu, “Flexural Vibration Band Gaps in Timoshenko Beams with Locally Resonant Structures”, *Journal of Applied Physics,* Vol. 100, No. 12, p. 124901, 2006.

4. Liu, X. N., G. K. Hu, C. T. Sun and G. L. Huang, “Wave Propagation Characterization and Design of Two-Dimensional Elastic Chiral Metacomposite”, *Journal of Sound and Vibration,* Vol. 330, No. 11, pp. 2536-2553, 2011.

5. Shen H., J. Wen, D. Yu and X. Wen, “The Vibrational Properties of a Periodic Composite Pipe in 3D Space," *Journal of Sound and Vibration,* Vol. 328, No. 1, pp. 57-70, 2009.

6. Kittel C., *Introduction to Solid State Physics*, Eighth Edition, John Wiley & Sons, New York, 2005.

7. Jiang, S., H. Hu and V. Laude, “Ultra-Wide Band Gap in Two-Dimensional Phononic Crystal with Combined Convex and Concave Holes”, *Physica Status Solidi (RRL)–Rapid Research Letters*, Vol. 12, No. 2, p. 1700317, 2017.

8. Gao, W., B. Yang, Y. Hong, K. Guo, P. Sun and J. Sun, “Investigation on Tunable Low-Frequency Property of Magnetic Field Induced Phononic Crystal with Archimedean Spiral-Beams”, *Mechanical Systems and Signal Processing*, Vol. 185, p. 109756, 2023.

9. Phani, A. S., J. Woodhouse and N. A. Fleck, “Wave Propagation in Two-Dimensional Periodic Lattices”, *The Journal of the Acoustical Society of America*, Vol. 119, No. 4, pp. 1995–2005, 2006.

10. Hussein, M. I., “Reduced Bloch Mode Expansion for Periodic Media Band Structure Calculations”, *Proceedings of the Royal Society A: Mathematical, Physical and Engineering Sciences*, Vol. 465, No. 2109, pp. 2825–2848, 2009.

11. Yin, C., Y. Xiao, D. Zhu, J. Wang and Q.-H. Qin, “Design of Low-Frequency 1D Phononic Crystals Harnessing Compression–Twist Coupling Effect with Large Deflection Angle”, *Thin-Walled Structures*, Vol. 179, p. 109600, 2022.

12. Axmann, W. and P. Kuchment, “An Efficient Finite Element Method for Computing Spectra of Photonic and Acoustic Band-Gap Materials: I. Scalar Case”, *Journal of Computational Physics*, Vol. 150, No. 2, pp. 468–481, 1999.

13. Yao, L., G. Jiang, F. Wu and J. Luo, “Band Structure Computation of Two-Dimensional and Three-Dimensional Phononic Crystals Using a Finite Element-Least Square Point Interpolation Method”, *Applied Mathematical Modelling*, Vol. 76, pp. 591–606, 2019.

14. Yang, H. Y. D., “Finite Difference Analysis of 2-D Photonic Crystals”, *IEEE Transactions on Microwave Theory and Techniques*, Vol. 44, No. 12, pp. 2688–2695, 1996.

15. Yang, W. H. and E. H. Lee, “Modal Analysis of Floquet Waves in Composite Materials”, *Journal of Applied Mechanics*, Vol. 41, No. 2, pp. 429–433, 1974.

16. Economou, E. N. and M. Sigalas, “Stop Bands for Elastic Waves in Periodic Composite Materials”, *The Journal of the Acoustical Society of America*, Vol. 95, No. 4, pp. 1734–1740, 1994.

17. Kushwaha, M. S., P. Halevi, G. Martinez, L. Dobrzynski and B. Djafari-Rouhani, “Theory of Acoustic Band Structure of Periodic Elastic Composites”, *Physical Review B* , Vol. 49, pp. 2313–2322, 1994.

18. Romero-Garcia, V., J. V. Sanchez-Perez and L. M. Garcia-Raffi, “Evanescent Modes in Sonic Crystals: Complex Dispersion Relation and Supercell Approximation”, *Journal of Applied Physics*, Vol. 108, No. 4, p. 044907, 2010.

19. Psarobas, I. E., N. Stefanou and A. Modinos, “Scattering of Elastic Waves by Periodic Arrays of Spherical Bodies”, *Physical Review B* , Vol. 62, pp. 278–291, 2000.

20. Leung, K. M. and Y. Qiu, “Multiple-Scattering Calculation of the Two-Dimensional Photonic Band Structure”, *Physical Review B,* Vol. 48, pp. 7767–7771, 1993.

21. Liu, Z., C. T. Chan, P. Sheng, A. L. Goertzen and J. H. Page, “Elastic Wave Scattering by Periodic Structures of Spherical Objects: Theory and Experiment”, *Physical Review B* , Vol. 62, pp. 2446–2457, 2000.

22. Cao, Y., Z. Hou and Y. Liu, “Finite Difference Time Domain Method for Band-structure Calculations of Two-Dimensional Phononic Crystals”, *Solid State Communications*, Vol. 132, No. 8, pp. 539–543, 2004.

23. Qiu, M. and S. He, “A Nonorthogonal Finite-Difference Time-Domain Method for Computing the Band Structure of a Two-Dimensional Photonic Crystal with Dielectric and Metallic Inclusions”, *Journal of Applied Physics,* Vol. 87, No. 12, pp. 8268–8275, 2000.

24. Hsieh, P.-F., T.-T. Wu and J.-H. Sun, “Three-Dimensional Phononic Band Gap Calculations Using the FDTD Method and a PC Cluster System”, *IEEE Transactions on Ultrasonics, Ferroelectrics, and Frequency Control* , Vol. 53, No. 1, pp. 148–158, 2006.

25. Tanaka, Y., Y. Tomoyasu and S.-I. Tamura, “Band Structure of Acoustic Waves in Phononic Lattices: Two-Dimensional Composites with Large Acoustic Mismatch”, *Physical Review B* , Vol. 62, pp. 7387–7392, 2000.

26. Singh, A. and P. K. Jain, “FDTD Analysis of the Dispersion Characteristics of the Metal PBG Structures”, *Progress In Electromagnetics Research B* , Vol. 39, pp. 71–88, 2012.

27. Sigalas, M. M. and N. Garcia, “Theoretical Study of Three Dimensional Elastic Band Gaps with the Finite-Difference Time-Domain Method”, *Journal of Applied Physics*, Vol. 87, No. 6, pp. 3122–3125, 2000.

28. Sigalas, M. M. and C. M. Soukoulis, “Elastic-Wave Propagation Through Disordered and/or Absorptive Layered Systems”, *Physical Review B*, Vol. 51, pp. 2780–2789, 1995.

29. Morini, L., Z.G. Tetik, G. Shmuel and M. Gei, “On the Universality of the Frequency Spectrum and Band-Gap Optimization of Quasicrystalline-Generated Structured Rods”, *Philosophical Transactions of the Royal Society A: Mathematical, Physical and Engineering Sciences*, Vol. 378, No. 2162, p. 20190240, 2020.

30. Yu, D., J. Wen, H. Zhao, Y. Liu and X. Wen, “Vibration Reduction by Using the Idea of Phononic Crystals in a Pipe-Conveying Fluid”, *Journal of Sound and Vibration*, Vol. 318, No. 1, pp. 193–205, 2008.

31. Yu, D., Y. Liu, G. Wang, L. Cai and J. Qiu, “Low Frequency Torsional Vibration Gaps in the Shaft with Locally Resonant Structures”, *Physics Letters A*, Vol. 348, No. 3, pp. 410–415, 2006.

32. Wang, G., J. Wen, Y. Liu and X. Wen, “Lumped-Mass Method for the Study of Band Structure in Two-Dimensional Phononic Crystals”, *Physical Review B*, Vol. 69, p. 184302, 2004.

33. Wang, G., X. Wen, J. Wen, L. Shao and Y. Liu, “Two-Dimensional Locally Resonant Phononic Crystals with Binary Structures”, *Physical Review Letters*, Vol. 93, p. 154302, 2004.

34. Zhang, Z., T. Li and Y. Tang, “Traveling Wave Analytical Solutions of Vibration Band Gaps of Composite Periodic Beams”, *Journal of Vibration and Control* , Vol. 25, No. 2, pp. 460–472, 2019.

35. Wang, Y.F., Y.Z. Wang, B. Wu, W. Chen and Y.S. Wang, “Tunable and Active Phononic Crystals and Metamaterials”, *Applied Mechanics Reviews*, Vol. 72, No. 4, p. 040801, 2020.

36. Hussein, M. I., M. J. Leamy and M. Ruzzene, “Dynamics of Phononic Materials and Structures: Historical Origins, Recent Progress, and Future Outlook”, *Applied Mechanics Reviews*, Vol. 66, No. 4, p. 040802, 2014.

37. Goffaux, C. and J. Sanchez-Dehesa, “Two-Dimensional Phononic Crystals Studied Using a Variational Method: Application to Lattices of Locally Resonant Materials”, *Physical Review B*, Vol. 67, p. 144301, 2003.

38. Liu, Z., C. T. Chan and P. Sheng, “Three-Component Elastic Wave Band-Gap Material”, *Physical Review B*, Vol. 65, p. 165116, 2002.

39. Jensen, J. S., “Phononic Band Gaps and Vibrations in One- and Two-Dimensional Mass–Spring Structures”, *Journal of Sound and Vibration*, Vol. 266, No. 5, pp. 1053–1078, 2003.

40. Claeys, C. C., K. Vergote, P. Sas and W. Desmet, “On the Potential of Tuned Resonators to Obtain Low-Frequency Vibrational Stop Bands in Periodic Panels”, *Journal of Sound and Vibration*, Vol. 332, No. 6, pp. 1418–1436, 2013.

41. Lu, Y. and A. Srivastava, “Level Repulsion and Band Sorting in Phononic Crystals”, *Journal of the Mechanics and Physics of Solids*, Vol. 111, pp. 100–112, 2018.

42. Yilmaz, C., G. M. Hulbert and N. Kikuchi, “Phononic Band Gaps Induced by Inertial Amplification in Periodic Media”, *Physical Review B*, Vol. 76, p. 054309, 2007.

43. Yilmaz, C. and G. M. Hulbert, “Theory of Phononic Gaps Induced by Inertial Amplification in Finite Structures”, *Physics Letters A*, Vol. 374, No. 34, pp. 3576–3584, 2010.

44. Xi, C., L. Dou, Y. Mi and H. Zheng, “Inertial Amplification Induced Band Gaps in Corrugated-Core Sandwich Panels”, *Composite Structures*, Vol. 267, p. 113918, 2021.

45. Acar, G. and C. Yilmaz, “Experimental and Numerical Evidence for the Existence of Wide and Deep Phononic Gaps Induced by Inertial Amplification in Two-Dimensional Solid Structures”, *Journal of Sound and Vibration*, Vol. 332, No. 24, pp. 6389–6404, 2013.

46. Ding, W., T. Chen, C. Chen, D. Chronopoulos and J. Zhu, “A Three-Dimensional Twisted Phononic Crystal with Omnidirectional Bandgap Based on Inertial Amplification by Utilizing Translation-Rotation Coupling”, *Journal of Sound and Vibration*, Vol. 541, p. 117307, 2022.

47. Taniker, S. and C. Yilmaz, “Design, Analysis and Experimental Investigation of Three-Dimensional Structures with Inertial Amplification Induced Vibration Stop Bands”, *International Journal of Solids and Structures*, Vol. 72, pp. 88–97, 2015.

48. Mizukami, K., K. Funaba and K. Ogi, “Design and Three-Dimensional Printing of Carbon-Fiber-Composite Elastic Metamaterials with Inertial Amplification Mechanisms”, *Journal of Sound and Vibration*, Vol. 513, p. 116412, 2021.

49. Yan, Y., A. Laskar, Z. Cheng, F. Menq, Y. Tang, Y. L. Mo and Z. Shi, “Seismic Isolation of Two Dimensional Periodic Foundations”, *Journal of Applied Physics*, Vol. 116, No. 4, p. 044908, 2014.

50. Li, J. and S. Li, “Generating Ultra Wide Low-Frequency Gap for Transverse Wave Isolation via Inertial Amplification Effects”, *Physics Letters A*, Vol. 382, No. 5, pp. 241–247, 2018.

51. Taniker, S. and C. Yilmaz, “Generating Ultra Wide Vibration Stop Bands by a Novel Inertial Amplification Mechanism Topology with Flexure Hinges”, *International Journal of Solids and Structures*, Vol. 106-107, pp. 129–138, 2017.

52. Hou, M., J. H. Wu, S. Cao, D. Guan and Y. Zhu, “Extremely Low Frequency Band Gaps of Beam-Like Inertial Amplification Metamaterials”, *Modern Physics Letters B*, Vol. 31, No. 27, p. 1750251, 2017.

53. Zeng, Y., L. Cao, S. Wan, T. Guo, Y.-F. Wang, Q.-J. Du, B. Assouar and Y.-S. Wang, “Seismic Metamaterials: Generating Low-Frequency Bandgaps Induced by Inertial Amplification”, *International Journal of Mechanical Sciences*, Vol. 221, p. 107224, 2022.

54. Yuksel, O. and C. Yilmaz, “Realization of an Ultrawide Stop Band in a 2-D Elastic Metamaterial with Topologically Optimized Inertial Amplification Mechanisms”, *International Journal of Solids and Structures*, Vol. 203, pp. 138–150, 2020.

55. Muhammad, S., S. Wang, F. Li and C. Zhang, “Bandgap Enhancement of Periodic Nonuniform Metamaterial Beams with Inertial Amplification Mechanisms”, *Journal of Vibration and Control*, Vol. 26, No. 15-16, pp. 1309–1318, 2020.

56. Adhikari, S. and A. Banerjee, “Enhanced Low-Frequency Vibration Energy Harvesting with Inertial Amplifiers”, *Journal of Intelligent Material Systems and Structures*, Vol. 33, No. 6, pp. 822–838, 2022.

57. Orta, A. H. and C. Yilmaz, “Inertial Amplification Induced Phononic Band Gaps Generated by a Compliant Axial to Rotary Motion Conversion Mechanism”, *Journal of Sound and Vibration*, Vol. 439, pp. 329–343, 2019.

58. Zeighami, F., A. Palermo and A. Marzani, “Inertial Amplified Resonators for Tunable Metasurfaces”, *Meccanica*, Vol. 54, No. 13, pp. 2053–2065, 2019.

59. Barys, M., J. S. Jensen and N. M. M. Frandsen, “Efficient Attenuation of Beam Vibrations by Inertial Amplification”, *European Journal of Mechanics - A/Solids*, Vol. 71, pp. 245–257, 2018.

60. Yuksel, O. and C. Yilmaz, “Size and Topology Optimization of Inertial Amplification Induced Phononic Band Gap Structures”, *Proceedings of the ASME 2017 International Mechanical Engineering Congress and Exposition*, Florida, USA, 2017.

61. Zhou, J., L. Dou, K. Wang, D. Xu and H. Ouyang, “A Nonlinear Resonator with Inertial Amplification for Very Low-Frequency Flexural Wave Attenuations in Beams”, *Nonlinear Dynamics*, Vol. 96, pp. 647–665, 2019.

62. Yuksel, O. and C. Yilmaz, “Shape Optimization of Phononic Band Gap Structures Incorporating Inertial Amplification Mechanisms”, *Journal of Sound and Vibration*, Vol. 355, pp. 232–245, 2015.

63. Miniaci, M., M. Mazzotti, A. Amendola and F. Fraternali, “Effect of Prestress on Phononic Band Gaps Induced by Inertial Amplification”, *International Journal of Solids and Structures*, Vol. 216, pp. 156–166, 2021.

64. Banerjee, A., S. Adhikari and M. I. Hussein, “Inertial Amplification Band-Gap Generation by Coupling a Levered Mass with a Locally Resonant Mass”, *International Journal of Mechanical Sciences*, Vol. 207, p. 106630, 2021.

65. Dong, Z. and P. Sheng, “Inertial-Amplified Mechanical Resonators for the Mitigation of Ultralow-Frequency Vibrations”, *Physical Review Applied* , Vol. 18, p. 014027, 2022.

66. Zeng, Y., L. Cao, S. Wan, T. Guo, S. An, Y.-F. Wang, Q.-J. Du, B. Vincent, Y.-S. Wang and B. Assouar, “Inertially Amplified Seismic Metamaterial with an

Ultra-Low-Frequency Bandgap", *Applied Physics Letters*, Vol. 121, No. 8, p. 081701, 2022.

67. Cheng, Z., A. Palermo, Z. Shi and A. Marzani, "Enhanced Tuned Mass Damper Using an Inertial Amplification Mechanism", *Journal of Sound and Vibration*, Vol. 475, p. 115267, 2020.

68. Muhammad and C. W. Lim, "Ultrawide Bandgap by 3D Monolithic Mechanical Metastructure for Vibration and Noise Control", *Archives of Civil and Mechanical Engineering*, Vol. 21, No. 2, p. 52, 2021.

69. Martinez, J. A. I, J. Moughames, G. Ulliac, M. Kadic and V. Laude, "Three-Dimensional Phononic Crystal with Ultra-Wide Band Gap at Megahertz Frequencies", *Applied Physics Letters*, Vol. 118, No. 6, p. 063507, 2021.

70. Muhammad and C. W. Lim, "Phononic Metastructures with Ultrawide Low Frequency Three-Dimensional Band Gaps as Broadband Low Frequency Filter", *Scientific Reports*, Vol. 11, No. 1, p. 7137, 2021.

71. Muhammad, "Design and Manufacturing of Monolithic Mechanical Metastructures Governing Ultrawide Low Frequency Three-Dimensional Band Gaps", *Additive Manufacturing*, Vol. 47, p. 102231, 2021.

72. D'Alessandro, L., R. Ardito, F. Braghin and A. Corigliano, "Low Frequency 3D Ultra-Wide Vibration Attenuation via Elastic Metamaterial", *Scientific Reports*, Vol. 9, No. 1, p. 8039, 2019.

73. D'Alessandro, L., E. Belloni, R. Ardito, A. Corigliano and F. Braghin, "Modeling and Experimental Verification of an Ultra-Wide Bandgap in 3D Phononic Crystal", *Applied Physics Letters*, Vol. 109, No. 22, p. 221907, 2016.

74. Lu, Y., Y. Yang, J. K. Guest and A. Srivastava, "3-D Phononic Crystals with Ultra-Wide Band Gaps", *Scientific Reports*, Vol. 7, No. 1, p. 43407, 2017.

75. Bloch, F., “Uber die Quantenmechanik der Elektronen in Kristallgittern”, *Zeitschrift für Physik*, Vol. 52, No. 7, pp. 555–600, 1929.

76. Brillouin, L., *Wave Propagation in Periodic Structures*, McGraw-Hill, New York, 1946.

77. Myers, H.P., *Introductory Solid State Physics*, CRC Press, London, 1997.

78. Phani, A. S. and M. I. Hussein, *Dynamics of Lattice Materials*, John Wiley & Sons, New York, 2017.

79. Krattiger, D., *Fast Band-Structure Computation for Phononic and Electronic Waves in Crystals*, Ph.D. Thesis, University of Colorado, 2017.

80. Bertoldi, K. and M. C. Boyce, “Wave Propagation and Instabilities in Monolithic and Periodically Structured Elastomeric Materials Undergoing Large Deformations”, *Physical Review B*, Vol. 78, p. 184107, 2008.

81. Bertoldi, K., M. C. Boyce, S. Deschanel, S. M. Prange and T. Mullin, “Mechanics of Deformation-Triggered Pattern Transformations and Superelastic Behavior in Periodic Elastomeric Structures”, *Journal of the Mechanics and Physics of Solids*, Vol. 56, No. 8, pp. 2642–2668, 2008.

82. Gomez, S. E. R., *Wave Propagation in a Phase Transforming Cellular Material*, M.S. Thesis, Universidad Escuela de Administracion, Finanzas e Instituto Tecnologico, 2016.

83. Lim, Q. J., P. Wang, S. J. A. Koh, E. H. Khoo and K. Bertoldi, “Wave Propagation in Fractal-Inspired Self-Similar Beam Lattices”, *Applied Physics Letters*, Vol. 107, No. 22, p. 221911, 2015.

84. Liu, J. and K. Bertoldi, “Bloch Wave Approach for the Analysis of Sequential Bifurcations in Bilayer Structures”, *Proceedings of the Royal Society A: Mathematical, Physical and Engineering Sciences*, Vol. 471, No. 2182, p. 20150493, 2015.

85. Aberg, M. and P. Gudmundson, “The Usage of Standard Finite Element Codes for Computation of Dispersion Relations in Materials with Periodic Microstructure”, *The Journal of the Acoustical Society of America*, Vol. 102, No. 4, pp. 2007–2013, 1997.

86. Otlu, S. N., *Ultrawide Stop Band in a 3D Elastic Metamaterial with Inertial Amplification Mechanisms Having Cross Flexure Hinges*, M.S. Thesis, Boğaziçi University, 2022.

87. Acar, B., *Design and Analysis of Ultrawide Elastic Metamaterial for Three Dimensional Vibration Isolation*, M.S. Thesis, Boğaziçi University, 2022.

APPENDIX A: PSEUDO CODE THAT COMPUTES THE BAND STRUCTURE OF THE 2D STRUCTURES

Input: K and **M** matrices, node numbers, # Increments

Output: Eigenvalues and eigenvectors

Determine node numbers: nL, nR, nB, nT, nBL, nBR, nTL, nTR, nI ← left, right, bottom, top, corner, internal nodes

Determine each DOF: $qL \leftarrow [2nL - 1 \;\; 2nL]$ // Same procedure for each DOF

Import: K and **M** matrices from ABAQUS with all free boundary conditions, **K**, **M** matrices should be $2n \times 2n$ square matrices where n is the total number of nodes

for i=1 to #Increments **do** // Determine each edge of the IBZ of the unit cell

    $k(i) \leftarrow [k1(i) \;\; k2(i)]$ // Wave vector

end

$qn \leftarrow length(qI) + length(qL) + length(qB) + length(qBL)$ // Reduced number of DOFs

$P \leftarrow zeros(2n, qn)$, $P0 \leftarrow zeros(2n, qn)$, $Px \leftarrow zeros(2n, qn)$, $Py \leftarrow zeros(2n, qn)$, $Pxy \leftarrow zeros(2n, qn)$ // Form Bloch periodicity submatrices

for i=1 to 2n **do** // Find the locations of each DOF in the Bloch-periodicity matrix

    $[row, column] \leftarrow find(qL == i)$

    $P0(i, column) \leftarrow 1$ // Same procedure for each DOF

end

for i=1 to #Increments **do** // Calculate the eigenvectors and eigenvalues

    $lambda1 \leftarrow exp(1i * k1(i) * r1)$ // Multiplier of right and left

    $lambda2 \leftarrow exp(1i * k2(i) * r2)$ // Multiplier of top and bottom

    $P \leftarrow P0 + lambda1 * Px + lambda2 * Py + lambda1 * lambda2 * Pxy$

    $KR \leftarrow P' * K * P$ // Reduced stiffness matrix

    $MR \leftarrow P' * M * P$ // Reduced mass matrix

    $[V, D] \leftarrow eigs(KR, MR)$

end

APPENDIX B: ELSEVIER LICENSE NUMBER 5458851205096

ELSEVIER LICENSE
TERMS AND CONDITIONS

Jan 04, 2023

This Agreement between BoGAZICI UNIVERSITY -- Zafer Gökay Tetik ("You") and Elsevier ("Elsevier") consists of your license details and the terms and conditions provided by Elsevier and Copyright Clearance Center.

License Number	5458851205096
License date	Dec 30, 2022
Licensed Content Publisher	Elsevier
Licensed Content Publication	Physics Letters A
Licensed Content Title	Low frequency torsional vibration gaps in the shaft with locally resonant structures
Licensed Content Author	Dianlong Yu,Yaozong Liu,Gang Wang,Li Cai,Jing Qiu
Licensed Content Date	Jan 2, 2006
Licensed Content Volume	348
Licensed Content Issue	3-6
Licensed Content Pages	6
Start Page	410
End Page	415
Type of Use	reuse in a thesis/dissertation
Portion	figures/tables/illustrations
Number of figures/tables/illustrations	2
Format	both print and electronic
Are you the author of this Elsevier article?	No
Will you be translating?	No
Title	BAND STRUCTURE CALCULATION OF 3D ULTRAWIDE ELASTIC METAMATERIALS WITH EMBEDDED INERTIAL AMPLIFICATION MECHANISMS
Institution name	BOGAZICI UNIVERSITY
Expected presentation date	Dec 2022

Figure B.1. Elsevier license of [31] for Figures 2.20 and 2.21.

APPENDIX C: JOHN WILEY AND SONS LICENSE NUMBER 5458850506031

JOHN WILEY AND SONS LICENSE TERMS AND CONDITIONS

Jan 04, 2023

This Agreement between BoGAZICI UNIVERSITY -- Zafer Gökay Tetik ("You") and John Wiley and Sons ("John Wiley and Sons") consists of your license details and the terms and conditions provided by John Wiley and Sons and Copyright Clearance Center.

License Number	5458850506031
License date	Dec 30, 2022
Licensed Content Publisher	John Wiley and Sons
Licensed Content Publication	PHYSICA STATUS SOLIDI (RRL) RAPID RESEARCH LETTERS
Licensed Content Title	Ultra-Wide Band Gap in Two-Dimensional Phononic Crystal with Combined Convex and Concave Holes
Licensed Content Author	Vincent Laude, Hongping Hu, Shan Jiang
Licensed Content Date	Dec 13, 2017
Licensed Content Volume	12
Licensed Content Issue	2
Licensed Content Pages	5
Type of Use	Dissertation/Thesis
Requestor type	University/Academic
Format	Print and electronic
Portion	Figure/table
Number of figures/tables	3
Will you be translating?	No
Title	BAND STRUCTURE CALCULATION OF 3D ULTRAWIDE ELASTIC METAMATERIALS WITH EMBEDDED INERTIAL AMPLIFICATION MECHANISMS
Institution name	BOGAZICI UNIVERSITY
Expected presentation date	Dec 2022

Figure C.1. John Wiley and Sons license of [7] for Figures 2.24, 2.25 and 2.26.

APPENDIX D: ELSEVIER LICENSE NUMBER 5458850899369

ELSEVIER LICENSE
TERMS AND CONDITIONS

Jan 04, 2023

This Agreement between BoGAZICI UNIVERSITY -- Zafer Gökay Tetik ("You") and Elsevier ("Elsevier") consists of your license details and the terms and conditions provided by Elsevier and Copyright Clearance Center.

License Number	5458850899369
License date	Dec 30, 2022
Licensed Content Publisher	Elsevier
Licensed Content Publication	Applied Mathematical Modelling
Licensed Content Title	Band structure computation of two-dimensional and three-dimensional phononic crystals using a finite element-least square point interpolation method
Licensed Content Author	Lingyun Yao,Guoqi Jiang,Fei Wu,Jinyu Luo
Licensed Content Date	Dec 1, 2019
Licensed Content Volume	76
Licensed Content Issue	n/a
Licensed Content Pages	16
Start Page	591
End Page	606
Type of Use	reuse in a thesis/dissertation
Portion	figures/tables/illustrations
Number of figures/tables/illustrations	3
Format	both print and electronic
Are you the author of this Elsevier article?	No
Will you be translating?	No
Title	BAND STRUCTURE CALCULATION OF 3D ULTRAWIDE ELASTIC METAMATERIALS WITH EMBEDDED INERTIAL AMPLIFICATION MECHANISMS
Institution name	BOGAZICI UNIVERSITY
Expected presentation date	Dec 2022

Figure D.1. Elsevier license of [13] for Figures 2.29, 2.30 and 2.31.